Ollscoil na hÉireann, Corcaigh

National University of Ireland, Cork

Scalable Solid State Synthesis of Core-Shell Pt@Cu_2O Nanocubes with Controlled Size and Shape

Thesis presented by

Hazel Neill B.Sc.

for the degree of

Master of Science

University College Cork

School of Chemistry

Head of School: Dr. Humphrey Moynihan

Supervisor(s): Dr. Gillian Collins and Dr. Brenda Long

September 2021

Declaration of Authorship:

This is to certify that the work that I am submitting is my own and has not been submitted for any other degree, either at University College Cork or elsewhere. All external sources and references have been clearly acknowledged and identified within the contents of this thesis. I have read and understood the University College Cork's regulations concerning plagiarism.

Hazel Neill B.Sc.

Acknowledgments:

I would like to thank both my supervisors, Gillian and Brenda for their continuous support and help throughout the past two years in helping me grow as a researcher and complete this project to the best of my abilities. I would also like to thank the other members of MCAG who were always there to provide me with help and advice when I needed it and helped to make my experience an enjoyable one. I would especially like to thank Louise, whose initial work discovered these cubic structures and helped me get started. I would like to thank Kathleen for all the work she has done throughout her FYP and Vuslat for her help with testing the nanostructures for an application. I would also like to thank Luke for his work with the Au nanoparticles. Lastly, a special thanks to John for being constant a pillar of support throughout my research.

Abstract:

This works reports a novel solid state synthesis approach for the formation of shape controlled Pt@Cu_2O nanoparticles immobilized onto Cu substrates. High nanoparticle loading was achieved by the use of a self-assembled monolayer consisting of a long chain diamine. The SAM enabled immobilization of citrate stabilized Pt nanoparticles onto the Cu substrate. Annealing under a reducing atmosphere led to the formation of core-shell nanostructures with a cubic morphology. Characterisation showed the nanocubes to consist of a Pt core and crystalline oxide shell. A key question that is addressed in this work was determining the composition of the shell material. A combination of detailed materials characterisation including XPS, XRD and high resolution TEM analysis confirmed the composition to be Cu_2O. Preliminary measurements have demonstrated the use of the substrates in glucose sensing applications.

List of Abbreviations:

Abbreviation	***Interpretation***
AFM	Atomic Force Microscopy
A. Nigres	*Aspergillus nigres*
BE	Binding Energy
B. subtilis	*Bacillus subtilis*
C. albicans	*Candida albicans*
CCAD/Cu3	Electrodeposited Wafer
CMP/Cu1	Chemical Mechanical Polish
CTAB	Cetyltrimethylammonium bromide
CVD	Chemical Vapour Deposition
DAD	Diaminodecane
DI	Deionised Water
DMF	Dimethylformamide
DMSO	Dimethyl Sulfoxide
E. coli	*Escherichia coli*
EDX	Energy Dispersive X-ray
FG	Forming Gas
FWHM	Full Width Half Maxima
GO	Graphene Oxide

IPA	Isopropyl Alcohol
KE	Kinetic Energy
LPE	Liquid Phase Exfoliation
MOR	Methanol Oxidation Reaction
MRSA	*Meticillin-resistant S. aureus*
NMP	*N*-methyl-pyrrolidone
NP	Nanoparticles
P. aeruginosa	*Pseudomonas aeruginosa*
PEG	Polyethylene Glycol
PtNP	Platinum Nanoparticles
PVA	Polyvinyl Alcohol
PVD/Cu2	Physical Vapour Deposition
PVP	Polyvinylpyrrolidone
RT	Room Temperature
SAM	Self-Assembled Monolayer
S. aureus	*Staphylococcus aureus*
S. cerevisiae	*Saccharomyces cerevisiae*
SCH	Sodium Cholate Hydrate
SEM	Scanning Electron Microscopy
TEM	Transmission Electron Microscopy

TMD	Transition Metal Dichalcogenide
XPS	X-ray Photoelectron Spectroscopy
XRD	X-ray Diffraction
XTEM	Cross-Section Transmission Electron Microscopy

Table of Contents

List of Tables and Figures

Tables:

<u>Chapter One</u>

Chapter Three

Appendix Chapter:

Figures:

Chapter One

Chapter Two

Chapter Three:

Figure 3.15: Cyclic voltammetry studies of functionalized and blank wafers in **a)** NaOH solution in the **b)** presence and absence of glucose and **c)** comparison of blank and functionalized wafers in presence of glucose.

Figure 3.16: a) Cyclic voltammetry response towards increased conc. of glucose, **b)** calibration study with chronoamperometry **c)** corresponding calibration curve and **d)** reproducibility of substrates.

Figure 3.17: SEM images of Au nanoparticles supported on Cu substrates **a)** unannealed and **b)** annealed.

Figure 3.18: SEM of **a)** as-received Cu1 **b)** Cu1 with no SAM but with PtNPs and **c)** Cu1 with SAM + PtNPs.

Figure 3.19: SEM image of Cu wafer after annealing **a)** with DAD SAM **b)** with no DAD SAM.

Figure 3.20: a) Cu1 **b)** Cu2 and **c)** Cu3 wafer after being annealed under conditions 1. **d)** Cu1, **e)** Cu2 and **f)** Cu3 wafer after being annealed under conditions 2. **g)** Cu1, **h)** Cu2 and **i)** Cu3 condition after being annealed under conditions 3.

Figure 3.21: Cu2 wafer after annealing at **a)** 450°C, **b)** 550°C and **c)** 650°C. Cu1 wafer after annealing at **d)** 450°C, **e)** 550°C and **f)** 650°C. Cu3 wafer after annealing at **g)** 450°C, **h)** 550°C and **i)** 650°C.

Figure 3.22: XRD analysis of as received and treated Cu1 wafers.

Figure 3.23: Scanning electron microscopy image of **a)** Cu1, **b)** Cu2 and **c)** Cu3 as-received (inset is the atomic force microscopy image of each substrate).

Figure 3.24: Time Deposition study on **a)** Cu1 wafer, **b)** Cu3 wafer and **c)** Cu3 wafer reaction after 35 min.

Figure 3.25: Cu3 wafer with PtNP deposition time of **a)** 128 min and **b)** 256 min.

Appendix Chapter:

Figure A.1: a) Dark navy MoS_2 solution before sonication, **b)** deep green MoS_2 solution after sonication

Figure A.2: SEM images of **a)** the exfoliated MoS_2 powder and **b)** more detailed exfoliated MoS_2 powder.

Chapter One:

Introduction

Copper Oxides Nanoparticles Review

1.1 Introduction:

Transition metal oxide nanostructures have attracted substantial research interest, mainly due of their unique characteristics at nanoscale dimensions compared to those of bulk their counterparts. They encompass a very large class of compounds such as manganese oxides (MnO_x), zinc oxide (ZnO), titanium dioxide (TiO_2), tin oxides (SnO_x), iron oxides (FeO_x) amongst others. Nanostructured transition metal oxides are utilised in a vast range of applications including sensors,[1] bactericidal agents,[2] energy storage,[3] photocatalysts,[2] batteries,[4] solar cells[1] and catalysis.[5] Copper oxides (CuO and Cu_2O) have been established as technologically important materials due to their unique advantages of low cost, high chemical stability and remarkable electrochemical performance, particularly, in the fields of catalysis, photovoltaics, sensors and energy storage applications.

The most common crystal phases of Cu_xO are copper(II) oxide or cupric oxide (CuO), and copper(I) oxide or cuprous oxide (Cu_2O). CuO is black solid and crystallizes in the monoclinic crystal system while Cu_2O has a red-brown colour and crystallizes in a cubic structure. A third stable phase of copper-oxide is also known, Cu_4O_3, with the mineral name of paramelaconite. Cu_4O_3 is a mixture of Cu(I) and Cu(II) oxide and has been much less explored relative to CuO and Cu_2O. Both CuO and Cu_2O are p-type semiconductors and their reported band gaps are 1.3 eV - 2.1 eV for CuO and 2.1 eV – 2.6 eV for Cu_2O.[6] The p-type conductivity in these oxides arises from the existence of negatively charged Cu vacancies and CuO and Cu_2O thin films are widely used in several device applications such as thin film transistors, photovoltaics, smart windows and IR detectors.

Nanostructured Cu_xO can be grown using different synthesis techniques, including solid or vapour and liquid phase solution processes, in which a variety of morphologies can be obtained. Commonly used solution synthesis methods include seed mediated growth,[7] sol-gel

method,[8] hydrothermal route,[9] sonochemical techniques[5] and microwave irradiated method[10] as well as many others. Vapour phase synthesis methods are broadly divided into physical vapour deposition (PVD) and chemical vapor deposition (CVD) techniques. The synthesis methodology of CuO/Cu_2O nanostructures can determine their morphology, size and whether or not the nanoparticles are mobilised onto a support material. In general, nanoparticles are commonly made using one of two methods, either top down or bottom up approach. The top down approach involves a bulk material that is either cut or sliced in size until the nanometre scale is reached. The bottom up approach refers to the build-up of material from precursor so that the nanoparticles are effectively built atom by atom or molecule by molecule. A schematic of both methods of nanoparticle synthesis can be seen in **Figure 1.1**.

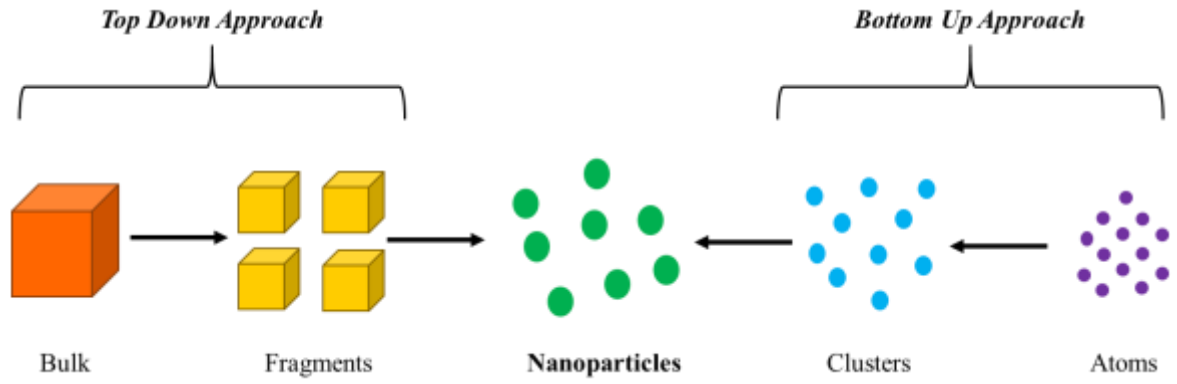

Figure 1.1: Reaction scheme for top down and bottom up approach to nanoparticle synthesis, *adapted from Reference 11.*

Bottom up synthesis is the most widely used methodology for synthesising CuO and Cu_2O nanostructures and can be broadly divided into solution based synthesis and solid state synthesis, which are discussed in the detail in the next section.

1.2 Solution synthesis

1.2.1 Seed Mediated Growth:

Seed mediated growth as the name suggests involves synthesising the nanostructures from prepared seeds. Seed-mediated synthesis typical requires the use of a capping agent and a reducing agent, such as sodium borohydride ($NaBH_4$) , L-ascorbic acid or sodium ascorbate.[12] Seed-mediate growth is particularly advantageous for controlling the final size and morphology of the Cu_xO nanostructures. Capping agents operate by preventing growth of the nanoparticle in a particular direction through selective adsorption along a specific lattice plane, thereby preventing crystal growth along this direction, resulting in control over the final morphology of the nanoparticle. Two of the most commonly used capping agents for CuO nanoparticle synthesis are polyvinylpyrrolidone (PVP)[13] and oleylamine[5] while the most common for Cu_2O nanoparticle synthesis are polyethylene glycol (PEG)[14,15] and sodium dodecyl sulphate (SDS).[16,17]

Seed nanoparticles used in seed-mediated growth are typically in the range of 3-13 nm in size.[7,18–20] The larger the seed size is, the larger the subsequent nanoparticles will be, if other reaction parameters remain the same. The seeds synthesised are commonly spherical in shape[18,20] however, this is not always the case as seeds can also have a nanoflake[21] morphology as well as cubic.[19] A variety of different nanoparticle morphologies have been synthesised using seed-mediated growth including cubic,[12] nanoflowers,[22] nanorods,[18] and nanowires[23]. Seed mediated growth can be conducted as a one-step synthesis where the seeds are prepared in-situ or as a two-step synthesis technique, where the seeds are isolated prior to the overgrowth step, which is demonstrated in **Figure 1.2.**

Figure 1.2: Reaction scheme for seed mediated approach to nanoparticle synthesis, *adapted from Reference 20.*

1.2.2 Sol-Gel Method:

The sol-gel method is an abbreviation of solution-gel method.[24] The sol-gel methodology involves preparation of a solution that subsequently evolves into a gel and finally after a period of drying and calcination produces CuO nanoparticles. A typical sol-gel procedure requires a copper precursor such as a copper salt. A stabilising or chelating agent such as surfactants prevent the agglomeration of the nanoparticles while they are in solution. Once the homogeneous solution has been synthesised it is commonly blue/green in colour due to the present of Cu ions[2,25,26] and a precipitate usually forms at this point. This precipitate is dried and this can be done through evaporation of excess solvents[26] or the use of an oven or furnace.[2,27,28] After the drying process a black powder is present, which is heated to high temperatures typically in the range of 400-600 °C for several hours. Annealing under an air or an oxygen atmosphere results in oxidation of the Cu precursor to give Cu_2O or CuO depending on the temperature.[8] Annealing under a reducing atmosphere *e.g.* H_2 results in reduction of the Cu precursor and can produce lower Cu oxidation states such as CuO and non-stoichiometric oxides.[28] A key advantage of the sol-gel method is the ability to the readily control the size of the nanoparticles[29,30] The most common metal precursors and their resultant morphologies can be seen in **Table 1.1**.

Table 1.1: Common reagents and morphologies produced from sol-gel synthesis

Cu Precursor	***Stabilising Agent***	***Morphology***	***Ref***
$Cu(NO_3)_2$	-	Spherical	2
$Cu(CH_3COO)_2$	Monoethanolamine	Core-Shell	25
$CuCl_2$	Acetic Acid	Spherical	8
$Cu(CH_3COO)_2$	-	Spherical	31
$Cu(CH_3COO)_2$	PEG	Spherical	27
$Cu(NO_3)_2$	Citric Acid	Spherical	26
$Cu(NO_3)_2$	-	Needle/Platelet	28
$Cu(acac)_2$	-	Nanotubes	32

1.2.3 Hydrothermal and Solvothermal Routes

The hydrothermal synthetic route is where reactions are carried out under aqueous conditions in a sealed, Teflon lined, pressurized container and with the reaction temperature often over the critical temperature of the solution.[33] These reactions are often carried out under alkaline conditions using NaOH, which acts as an accelerant by instantly precipitating out $Cu(OH)_2$. The most commonly used precursors and reagents for hydrothermal synthesis of CuO and Cu_2O nanostructures as well as the morphologies that these reactions produce can be seen **Table 1.2**.

Table 1.2: Common reagents and morphologies produced from the hydrothermal and solvothermal routes.

Cu Precursor	***Stabilising Agent***	***Accelerant***	***Teflon Autoclave***	***Morphology***	***Ref***
$Cu(NO_3)_2.3H_2O$	PEG	NaOH	Yes	Needle	9
$Cu(C_2H_3O_2).2H_2O$	PVP	NaOH	No	Nanocubes	13
$Cu(NO_3)_2.3H_2O$	-	NaOH	Yes	Flakes	33
$CuSO_4.5H_2O$	PEG	NaOH	Yes	Nanosheets/flakes	34
$CuSO_4.5H_2O$	$Na_3C_6H_5O_7$	NaOH	Yes	Spherical	35
$CuSO_4.5H_2O$	-	-	No	Spherical	36
$CuCl_2.H_2O$	-	NaOH	Yes	Nanobelt/Leaf	37
$Cu(NO_3)_2$	-	NaOH	Yes	Needle, Plate	38
$Cu(NO_3)_2.3H_2O$	NH_3H_2O	NaOH	Yes	Spherical, Hexapod	39
$Cu(CO_2CH_3)2H_2O$	Ethylene Glycol	-	Yes	Nanocomposite	40
$CuSO_4.5H_2O$	PVP	NaOH	Yes	Octahedral	41

In a typical hydrothermal synthesis, the aqueous Cu salt solution is mixed with a mineral base (usually NaOH) and sometimes a capping agent. The solution is heated under gentle stirring to form a homogenous solution of $[Cu(OH)_2]$ nanoparticles.[13,34] This solution is then transferred to a reaction vessel, mainly a Teflon lined autoclave or a hot air oven[13,36] and heated at elevated temperatures typically 100°C - 160°C[13,35] for a range of 15 min – 12 h.[34,42] Hydrothermal synthesis gives rise to high yield of CuO products, Lui et al report a 95% yield of CuO nanostructures.[42] A high yield of Cu_2O nanostructures were also produced using hydrothermal and solvothermal techniques.[41,43]

Other advantages of the hydrothermal route are that numerous inorganic salts can be dissolved in water enable a wide variety of precursors to be used. Water is a low cost, non-toxic and environmentally friendly solvent and the strong polarity of water may be favourable to the oriented growth of nanocrystals.[33] Hydrothermal synthesis also allows a range of different morphologies for CuO nanoparticles such as nanoflakes, nanoflowers, nanorods, and nanotubes, particularly with the use of capping ligands.[33] A schematic for the hydrothermal synthesis of cubic CuO nanoparticles using PVP as a capping agent is shown is **Figure 1.3**.

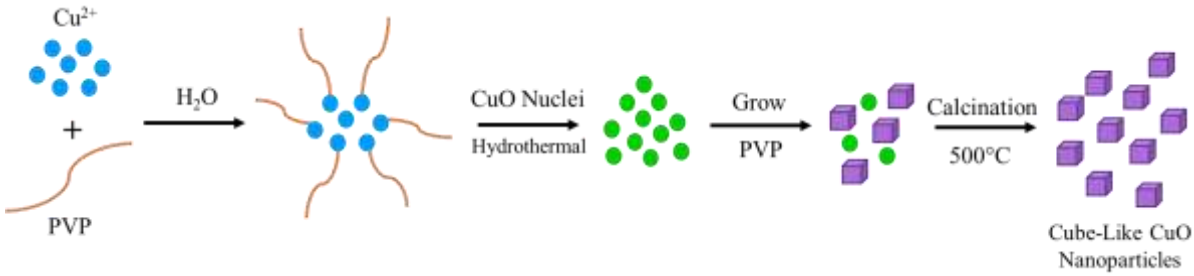

Figure 1.3: Proposed reaction for hydrothermal synthesis of PVP capped CuO nanoparticles, *adapted from Reference 13.*

1.2.4 Sonochemical Technique

The use of high intensity ultrasound for the preparation of many nanomaterials has been successful applied to the synthesis of CuO and Cu_2O nanostructures. The sonochemical technique to synthesising CuO and Cu_2O nanoparticles is similar to other solution methods previously described, with the addition of a sonication step. The most regularly used reagents and morphologies produced can be seen in **Table 1.3.** A solution containing the Cu salt, base and often but not always a capping ligand is first prepared and then subjected to sonication for a time period that ranged from 15 min - 3 h.[44–49] Sonication aids in the formation of a homogenous mixture of $Cu(OH)_2$, which is then calcined at 400°C -700°C[44,45,47,50] or in some

cases 100°C - 180°C[46,51] for a period of 2 h in either a furnace[45,47,51] or a hot air oven[46] analogous to that of the hydrothermal process. It is during the calcination process that the blue/green solution becomes a black or brick red suspension indicating the formation of CuO or Cu_2O nanoparticles. [46,52]

One of the key benefits of sonochemical synthesis methods is that the technique does not require high temperature or elevated pressures. Siva *et al.* used a sonochemical technique to obtain different morphologies of CuO nanostructures by tuning the concentration of cetyltrimethylammonium bromide (CTAB). [53] In his case CTAB acted as a miceller template and so the morphology of the micelles could be altered when the CTAB concentration was above the critical micelle concentration, resulting in different morphologies of CuO nanoparticles. A combination of CTAB and sodium salicylate (NaSal) stabilise the micelle system formed, inducing the formation of a wormlike micelle, allowing for synthesis of CuO nanorods using low a concentration of surfactant.[54]

Table 1.3: Common reagents and morphologies produced from the sonochemical technique.

Cu Precursor	***Stabilising Agent***	***Accelerant***	***Sonication***	***Morphology***	***Ref***
$Cu(NO_3)_2.3H_2O$	PVA	NaOH	Probe	Spherical	50
$Cu(NO_3)_2$	-	NaOH	Probe	Spherical	44
$Cu(NO_3)_2.3H_2O$	PEG	$(NH_4)_2CO_3$	Bath	Spherical	45
$Cu(NO_3)_2$	CTAB	NaOH	-	Nanoleaves	51
$Cu(CH_3COO)_2$	PVP	NaOH	Horn	Spherical	46
$Cu(CH_3COO)_2.H_2O$	-	NH_4OH	Horn	Spherical	47
$Cu(CH_3COO)_2.H_2O$	CTAB	NH_4Cl	Probe	Nanorods	48
$Cu(CH_3COO)_2.H_2O$	Glycerol	-	Horn	Spherical	52
$CuSO_4.5H_2O$	PVP	NaOH	Horn	Nanocubes	55
$Cu(CH_3COO)_2.H_2O$	*B*-cyclodextrin	-	Probe	Spherical	56

1.2.5 Microwave Irradiated Method

Microwave based techniques have advantages of faster rate of reaction, higher reproducibility, higher yields, and scalability compared to conventional heating processes. The most frequently used reagents and the resultant morphologies for this synthesis method can be seen in **Table 1.4**.

Table 1.4: Common reagents and morphologies produced from the microwave irradiated method.

Cu Precursor	*Capping Agent*	*Reducing Agent*	*Morphology*	*Ref*
$Cu(CH_3COO)_2$	PEG	-	Spherical	10
$Cu(CH_3COO)_2,2H_2O$	-	DMF	Spherical	57
$Cu(CH_3COO)_2$	PEG	-	Nanopowder	58
$Cu(NO_3)_2$	-	Urea	Nanorods	59
$Cu(NO_3)_2.6H_2O$	-	Urea	Spherical	60
$Cu(NO_3)_2.6H_2O$	-	Urea	Spherical	61
$CuSO_4.5H_2O$	L-glutamic Acid	-	Nanoleaves	62
$CuCl_2.2H_2O$	-	-	Nanoplates	63
$Cu(CH_3COO)_2$	-	Glucose	Spherical	64
$CuSO_4 \cdot 5H_2O$	$C_4H_4O_6KNa \cdot 4H_2O$	Glucose	Stellar, Cubic	65
$CuCl_2 \cdot 2H_2O$	PEG	Glucose	Octahedron	66

Microwave irradiated synthesis of CuO and Cu_2O nanoparticles begins with making an either aqueous or organic solution containing the Cu precursor along with capping ligands or reducing agents.[10,57–63] The mixture is then placed in a microwave oven or a microwave reflux system usually under air for a time period up to 30 min. Microwave synthesis parameters can be tuned to yield a range morphologies, as outlined in in Table 1.4. [10,58,59,61–63] The microwave irradiation of the solution can be continuous or involve on and off cycles of microwave irradiation over the reaction period. Once the solution is allowed to cool to room temperature and the black precipitate is collected by centrifugation and washed with one or all of the following solvents, deionised water, absolute ethanol and acetone.[10,60–63] The precipitate is

allowed to dry under air or in an oven at a range of temperatures including room temperature, 60°C or 100°C from a period 3 h to overnight.[58–60,62,63]

Some of the advantages associated with the microwave irradiation method for synthesising nanoparticles are short reaction time, narrow particle size distribution, small particle size and high purity of the nanoparticles. The increase reaction rate and lower energy consumption make microwave assisted heating a more economically favourable approach that conventional heating methodologies. [61]

1.2.6 Additional Synthetic Methods

Seed-mediated growth, sol-gel method, hydrothermal route, sonochemical technique and the microwave irradiation method are the most popular synthesis techniques for the preparation of CuO and Cu_2O nanoparticles each with their own advantages and disadvantages, as previously described. There are other less commonly used synthetic routes available for the synthesis of CuO and Cu_2O nanoparticles. These include synthesising nanoparticles using 3D printing[67] which were then used in the fabrication of glucose sensors. Other methods include metal organic gel synthesis[68] as well as green synthesis of nanoparticles, where natural derived reagents are used such the dried gum of Middle Eastern legumes.[69–71] Another additional synthetic route is solution combustion as it is a fast and facile method of synthesising highly crystalline nanoparticles of metals and metal oxides. The method involves heating the Cu precursor solution until evaporation of the solvent (typically water).[72] During the combustion process, the redox reaction between the metal precursors *e.g.* Cu salt, and the reducing agents such glycine, hydrazine, glucose, urea, provide the energy to sustain the combustion.[73] Solution combustion has also been integrated with microwave synthesis, where the solution was allowed

to boil, dehydrate and decomposition of gases occurred which lead to combustion of the solution.[61]

1.3 Vapour Phase and Solid State Synthesis:

While solution synthesis is more widely used for the synthesis of nanoparticles, vapour phase and solid state synthesis are also effective at producing nanoparticles and have been successfully applied to transition metals and metal oxides.[74–77] Vapour phase synthesis is divided into two different categories, physical vapour deposition (PVD) and chemical vapour deposition (CVD). These categories allow for a thin film of a chosen metal such as Cu to be deposited onto a substrate using a variety of techniques.[78] Vapour phase synthesis creates conditions where the vapour phase mixture is thermodynamically unstable in relation to the formation of the solid material that is to be prepared in nanoparticle form.[76] It produces nanoparticles from a supersaturated vapour which along with suitable condensation kinetics allows particles to nucleate homogeneously. The remaining supersaturation is relieved through the condensation of vapour phase molecules on the resulting particles which allows for particle growth.[76] Vapour phase deposition has been proven to be effective in the synthesis of CuO nanoparticles[79] as well as Cu_2O films[80] . Chemical vapour deposition can also produce CuO nanoparticles with a cubic morphology.[81]

Thermal oxidation techniques offer a simple, convenient and fast method to synthesize nanostructured Cu_xO with various morphologies including nanowires, nanoribbons and nanorods. Thermal oxidation is a technique that involves the process of growing a thin layer of oxide on the surface of a wafer,[82] by simply heating a substrate to a high temperature usually between 200 - 800°C in an oxygen rich environment. The morphology and stoichiometry of

the Cu_xO nanostructures can be controlled to some degree by tuning the reaction parameters such as annealing temperature.[78]

Solid state synthesis can also be utilised for CuO and Cu_2O nanoparticles as well as other copper species including Cu-ZnO and Cu-CdO.[83–86] There are other less common methods of solid state synthesis which include mortar grinding, vibration milling, mechanochemical processing. While theses methods are simple and offer advantages of scalability, they generally suffer from limited control over nanoparticle size and morphology. **Table 1.5** demonstrates the morphologies produced as a result of the different synthetic methods used.

Table 1.5: Synthesis methods and morphologies produced from solid state synthesis.

Synthesis Method	***Surfactant/Reducing Agent***	***Morphology***	***Ref***
Mortar Grinding	Leaf Extracts	Nanorods	85
Vibration Milling	Poly(vinylpyrrolidone)	Spherical	75
Mechanochemical Processing	Polyethylene Glycol 400	Nanoparticles	83
Green Synthesis	-	Nanoparticles	74
Chemical Synthesis	Polyethylene Glycol	Nanocubes	77

Some of the benefits linked to solid-state synthesis include, high-yield,[83] low cost,[74,75,77,83] green,[74] surfactant free,[75] room temperature synthesis,[74,75] size controllable nanoparticles,[74,75,77] as well as the benefit of scalibility.[74,75] The benefits associated with this type of synthesis makes it very appealing as it provides a simple method for synthesising nanoparticles with a variety of morphologies.

1.4 Shape controlled CuO and Cu_2O Nanostructures

Controlling the morphology of nanoparticles is crucial in determining their catalytic abilities, stability and surface area. When different crystallographic facets are exposed on CuO and Cu_2O nanoparticles it can result in facet-dependent chemical and physical properties, which have been shown to influence the catalytic, photocatalytic, electrochemical and optical properties of CuO and Cu_2O nanoparticles.[87] Therefore of devising methodologies that can control the resulting morphologies of the nanoparticles is important. Several reaction parameters are used to control the shape of the nanoparticles and these include precursor concentration, capping agents and reaction temperature as well as a combination of these.

Shui *et al.* used a sonochemical, surfactant free synthesis of CuO and Cu_2O nanostructures where the morphology of the nanostructures could be tuned by altering the molar ratio of NaOH to $CuSO_4$.[88] The morphologies obtained on varying the ratio of base to Cu precursor are summarised in **Table 1.6.** Radi *et al.* demonstrated an electrochemical method to prepare shape controlled nanostructures by varying the concentration of the electrolyte, in this case $CuSO_4.5H_2O$ along with the electrodeposition times.[87] The nanoparticles produced in this experiment were Cu-Cu_2O core shell with a CuO outer layer. The overall shape of the core shell nanoparticles are dependent on the initial shape of the Cu core.[87] The limiting planes for Cu with slower growth rates were (100) and (111) and the difference in the growth rates between the limiting planes causes specific facets to be exposed producing the shape of the nanoparticles. At 10 mM of the copper precursor, cubic nanoparticles are formed, at 100 mM cuboctaherdral nanoparticles are formed and at 200 mM octahedral nanoparticles are formed. Between 10 – 50 mM truncated nanocubes were formed.[87] These various morphologies of core shell nanoparticles are formed from the conversion of Cu nanoparticles to Cu_2O nanoparticles in the presence of aqueous electrolyte during electrodeposition.

Table 1.6: Morphologies of CuO and Cu_2O nanoparticles by changing the reactant molar ratios.[67]

Molar Ratio	***CuO***	***Cu_2O***
2	Spindle	-
2.5	-	Truncated Cube
3	Nanorods	Cuboctahedron
4	Nanoribbons	Octahedron
5	Agglomerates	-

Capping agents/surfactants can enable the selective growth of facets and are used extensively for shape controlled synthesis of nanoparticles. The morphology of Cu_2O nanoparticles can be altered when D-(+)-glucose is used as a capping agent.[89] When the solution was stirred for 15 min rhombicuboctaherdron and octahedron shaped nanoparticles were formed. When the solution when stirred for a longer reaction time of 60 min nanocubes were produced.[89]

Bai *et al.* conducted a detailed study on the shape controlled synthesis of Cu_2O nanoparticles evaluating the influence of capping ligands and reaction temperature.[90] L-Ascorbic acid was used as the reducing agent and PVP as the capping ligand.[90] In the absence of the surfactant, nanoparticles with irregular morphologies were produced. CuO nanocubes were formed when the PVP surfactant was present in concentrations of 0 – 0.018 mmol, due to capping of the (100) surface facets. They further showed that the concentration of ascorbic acid impacted on nanoparticle morphology. In the absence of ascorbic acid nanoparticle formation does not occur as no reduction of the precursor takes place. L-ascorbic acid in the presence of PVP give rise to nanocubes, however at high concentrations, ascorbic acid erodes the corners of the nanocubes giving rise to truncated nanocubes initially, which evolve to cuboctahedra

and finally octahedra. Interestingly, they showed that the solution stirring rate can influence the morphology of Cu_2O nanoparticles due to mechanical wear that can erode the corners of the nanocubes gradually altering the nanoparticle shape.[90] At 4 rotations per second (r/s) nanocubes are formed, a 5 r/s truncated cubes are formed and at 6 r/s Cu_2O nanospheres. At a higher rate than 6 r/s no nanoparticles form. The temperature of the reaction could also be altered to change the nanoparticle morphology as at a temperature between 30-50°C the morphology changed from truncated cube to uniform cubic.[90]

Reaction temperature can also be used to alter the morphology of CuO nanoparticles using a precipitation method. The Cu precursor solution is stirred at room temperature for various times and then heated to the higher reaction temperature.[91] **Table 1.7** shows the reaction conditions and the resultant morphologies of the CuO nanostructures as a result of tuning reaction temperature.

Table 1.7: Morphologies produced by the change in the reaction temperature.[91]

Reaction Time (h)	***Reaction Temp***	***Morphology***
24	60°C	Nanoparticles
15	80°C	Cube-like
10	110°C	Rectangular
8	160°C	Nanobar
5	180°C	Nanorod

1.5 Supported CuO and Cu_2O Nanoparticles:

For many applications it is necessary to immobilise nanoparticles onto a solid support material. Support materials are essential for many catalytic applications of nanoparticles and are typically characterised by high surface area, good chemical and physical stability and enable nanoparticles to be immobilised with high dispersion. Supported nanoparticles can be prepared in situ or in a two-step process whereby colloidal nanoparticles are first synthesised and then deposited onto the support.[92,93]

There are a range of different supports available to CuO and Cu_2O nanoparticles which include both oxide supports and non-oxide supports. There are many oxides used as supports for Cu_xO nanoparticles which include cerium oxide (CeO_2), iron oxide (Fe_3O_4), ɣ-aluminium oxide (ɣ-Al_2O_3) and aluminium silicate ($3Al_2O_3.2SiO_2$), silicon dioxide (SiO_2) and graphene oxide (GO). **Table 1.8** shows the different methods in which the nanoparticles are attached to the supports as well as their main application once immobilised.

Table 1.8: Oxide supports; their nanoparticle tethering methods and their applications.

Oxide Support	***Tethering Method***	***Application***	***Ref***
CeO_2	Impregnation	Interfacial Redox Process	94,95
Fe_3O_4	Impregnation	Magnetically Recyclable Catalysts	96
ɣ-Al_2O_3	Grinding Method	Catalytic elimination	94
$3Al_2O_3.2SiO_2$	NO reduction by CO	Catalytic elimination	97
Mesoporous Silica	Impregnation	-	98
3D Macroporous	Incipient Impregnation	Soot Combustion	99,100
Silica Thin Film	Immersion, Heat Treated	Photocatalyst	99
GO	Intercalation, Adsorption	Nanoelectronic devices	99,101,102

Silica Gel	Immersion, Heat Treated	CO Oxidation	103
Cu	Photoassisted Deposition	Photocatalysis of Atrazine	104
Mesoporous Silica	Impregnation, Heated	Hydrogen Generation	105

Some of the benefits to using oxide supports is that they can be low cost, have a high surface area which increases the amount of nanoparticles that can be immobilised on the surface.[96,100] The reaction scheme for the CuO nanoparticles supported on Fe_3O_4 can be seen **Figure 1.4.**

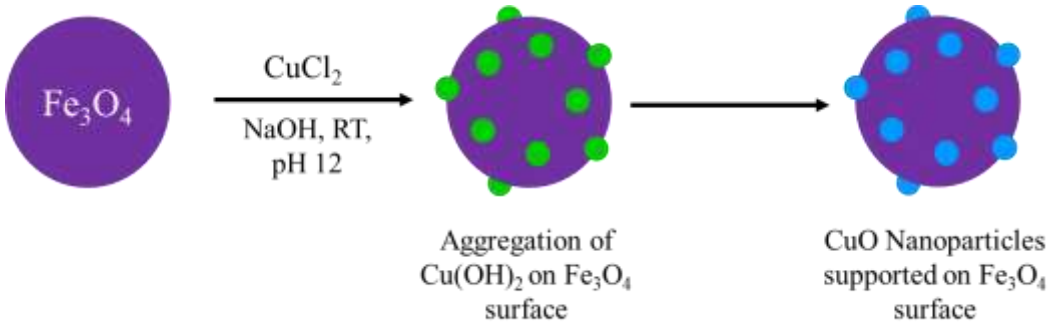

Figure 1.4: Reaction scheme for Fe_3O_4 supported CuO nanoparticles, *adapted from Reference 96.*

In addition to oxide supported nanoparticles, other supports available for the Cu_xO nanoparticles include cellulose, silicon, graphite and activated carbon. **Table 1.9** demonstrates the method of tethering the nanoparticles to the support as well as their application once immobilised onto the surface.

Table 1.9: Non-oxide supports; their nanoparticle tethering methods and their applications.

Non-oxide Support	***Tethering Method***	***Application***	***Ref***
Cellulose	Electrostatic Interactions	4-Nitrophenol Reduction	106,107
Silicon	Electroless Deposition	Nonenzymatic H_2O_2 Detection	108
Graphite	Wet Ball Milled	Nonenzymatic H_2O_2 Sensor	109–111
Activated Carbon	Impregnation	Water Pollutant Removal	112,113
Mesoporous TiP	Ion Dispersed	Environmental	114
CoAl-HT	Deposition Precipitation	Epoxidation of Styrene	115

Some of the benefits involved in using non-oxide supports are that they too have a high surface area, come in large quantities[106,108] and can also be considered as low cost as well as non-pollutants.[112] The reaction scheme for the CuO nanoparticle supported on cellulose can be seen in **Figure 1.5**.

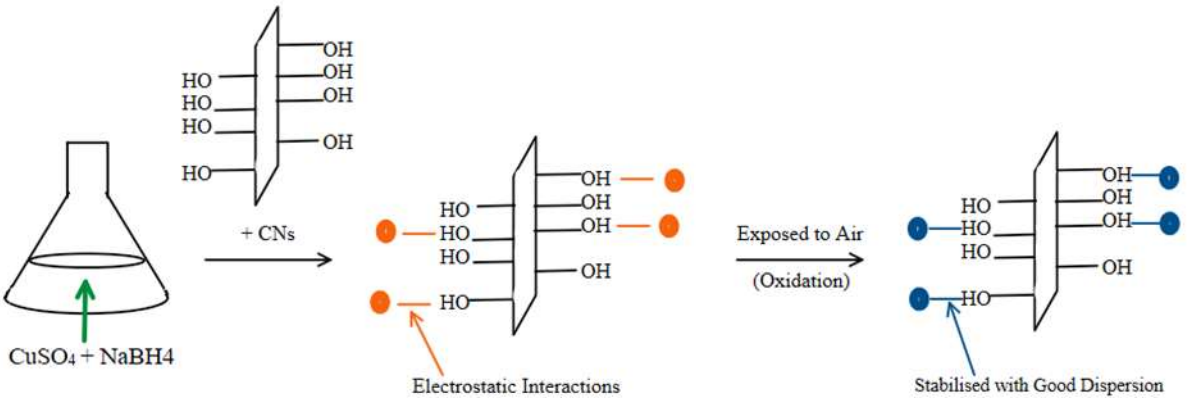

Figure 1.5: Mechanism two for cellulose supported CuO nanoparticles. The orange and blue circles represent the Cu and CuO nanoparticles respectively, *adapted from Reference 106.*

1.6 Applications of Cu_xO Nanoparticles

CuO and Cu_2O nanoparticles are very versatile materials. Their low cost and low toxicity are advantageous for many commercial uses and their major applications are in the areas of catalysis, biomedicine, sensors as well as batteries and energy storage. The most important of the applications for Cu_xO nanoparticles in this project is their use as sensors.

Catalysis, photocatalysis and electrocatalysts are also key applications of CuO and Cu_2O nanoparticles. Both CuO and Cu_2O are efficient photocatalysts for photodegradation of organic dyes and pollutants.[116,117] They are also high performing electrocatalysis particularly when their morphology is optimised as the electrocatalytic properties of Cu_2O nanocrystals have been shown to depend on the nanocrystal size and shape.[118] **Table 1.10** shows some of the main catalytic applications of the CuO and Cu_2O nanoparticles.

Table 1.10: Catalytic abilities of CuO and Cu_2O nanoparticles and their uses.

Catalytic Application	***Effective On***			***Ref***
Organic Reactions	*p*-nitrophenol	Boronation of Alkynes		62,119,120
Photocatalyst	*Escherichia coli*	Degradation of Pollutant Dyes	CO_2	5,47,99,121–123
Antibiotics	Production of Actinorhodin			124
Hydrogen Storage	Methanolysis of ammonia–borane			125
H_2 Production	Water or Biofuels			5
Electrooxidation	Organic Compounds			5
Photocatalyst	Degradation of Pollutant Dyes			47
Sensor	Glucose			17

Another application of CuO and Cu_2O nanoparticles lies in the biomedical field particularly in the application of their antimicrobial properties. CuO and Cu_2O nanoparticles have antibacterial properties similar to that of silver (Ag)[126] in that they are both utilised for antimicrobial formulations and wound dressings.[127] However one advantage Cu has over Ag is the lower cost as Cu. CuO nanoparticles demonstrated good antibacterial abilities against well-known bacteria including *Escherichia coli (E. coli)* which is Gram-negative, *Staphylococcus aureus (S. aureus)* which is Gram-positive as well as *meticillin-resistant S. aureus (MRSA)* which is also Gram-positive.[128] Cu_2O nanoparticles were found to display superior antibacterial properties to CuO, very similar to that of pure Cu.[129] Cu_2O nanoparticle incorporated into nano-cellulose fibres which displayed excellent antibacterial performance.[130]

CuO and Cu nanoparticles also have potential antiviral therapy to treat herpes simplex type 1[131] along with hepatitis C virus.[132] The importance of CuO nanoparticles role in combatting these microbes is vital when 67% (~5.2 billion) of the world's population is infected with herpes simplex type 1[131] and ~130-180 million people are effected by hepatitis C worldwide.[133]

CuO and Cu_2O nanoparticles also display antifungal properties and have been shown to inhibit the fungi *Aspergillus nigres (A. nigres)* and *Candida albicans (C. albicans)* as well as *Saccharomyces cerevisiae (S. cerevisiae).* These microbes can cause a variety of diseases such as urinary tract infections, hepatitis C as well as black mould and pneumonia and as a result are very dangerous. **Table 1.11** demonstrates the antimicrobial activities of CuO and Cu_2O nanoparticles.

Table 1.11: Antimicrobial activities of CuO and Cu_2O nanoparticles and their uses.

Antimicrobial Application	***Effective On***					***Ref***
Antibacterial	*E. coli*	*S. aureus*	*B. subtilis*	Biofouling	*P. aeruginosa*	25,134,135
Antiviral	Hepatitis C	Herpes Simplex Virus		MS2 Bacteriophages		131,132,136
Antifungal	*A. nigres*	*C. albicans*		*S. cerevisiae*		122,137

1.6.1 Sensor Applications of Cu_xO Nanoparticles

CuO, Cu_2O and hybrid CuO-Cu_2O nanoparticles can be utilized for various sensors which range from biosensors, environmental sensors, toxic compound sensors amongst others. The use of copper oxides is one of the most efficient ways to develop high-performance gas sensors and there have been many reports on the gas sensing properties of CuO and to a lesser extent Cu_2O.[1,138,139] The other important use for CuO and Cu_2O nanoparticles in sensors, lies in their ability to detect glucose.[21,67,72,140,141] This wide range of potential applications makes CuO and Cu_2O nanoparticles extremely versatile and gives them the potential to be suitable across many industries and processes and these applications are highlighted in **Table 1.12**.

Table 1.12: Copper oxide nanoparticles and their application as sensors.

Sensor Type	***Detection of***	***Ref***
Gas Sensor	H_2S, CH_2O, CH_3CHO and NO_2	1,142–144
Inorganic Compound	Hydrazine	22
Nanochemistry	Nanoenzymes	68
Environmental Factor	Humidity	44
Cholesterol	Hydrogen Peroxide	21,108,109

The ability to detect the oxidation of glucose and glucose oxidase is extremely important given that the chronic disease, diabetes directly involves the deficiency of insulin which regulates high blood glucose levels.[141] The original glucose sensors were based on enzymes and although these sensors were extremely sensitive towards glucose and glucose oxidase they suffered from disadvantages. These disadvantages included pH, as a change of pH could denature the enzyme as would a change of temperature outside of the optimum range of the enzyme. As a result of the enzymes instability to the changes in its environment, non-enzymatic glucose and glucose oxidase sensors became more prevalent. Non-enzymatic sensors were made possible through the use of transition metal oxides.

Transition metal oxides have proven to be very useful as catalysts in sensing applications. CuO is attractive material for sensing applications due to the easy, cost-effective and efficient methods available for the synthesis of CuO and Cu_2O nanoparticles with a high surface area.[68] Cu_2O nanoparticles, in particular those with a cubic morphology have been proven effective as non-enzymatic glucose sensors with a sensitivity of 3213 $\mu A\ mM^{-1}\ cm^{-2}$.[17]

It has been shown in the literature that Cu oxide based glucose sensors can have linear range of 1 – 15 mM to 22.55 mM[140] as well as sensitivity ranges of 1098.37 - 10,630 $\mu A\ mM^{-1}\ cm^{-2}$.[68,140] CuO nanoparticles in combination with other transition metals such as Pt have also demonstrated potential in the area of non-enzymatic glucose sensors. Pt cubes and CuO nanoflowers deposited on a graphene oxide surface produced a linear range of 12 mM and a sensitivity range of 3577 $\mu A\ mM^{-1}\ cm^{-2}$ towards glucose.[141] There is evidence that CuO nanoparticles both alone and in combination with other transition metals have an excellent ability to detect glucose and glucose oxidase and further research needs to be done to further enhance these abilities. A schematic of a Cu-foam based glucose sensor can be seen in **Figure 1.6.**

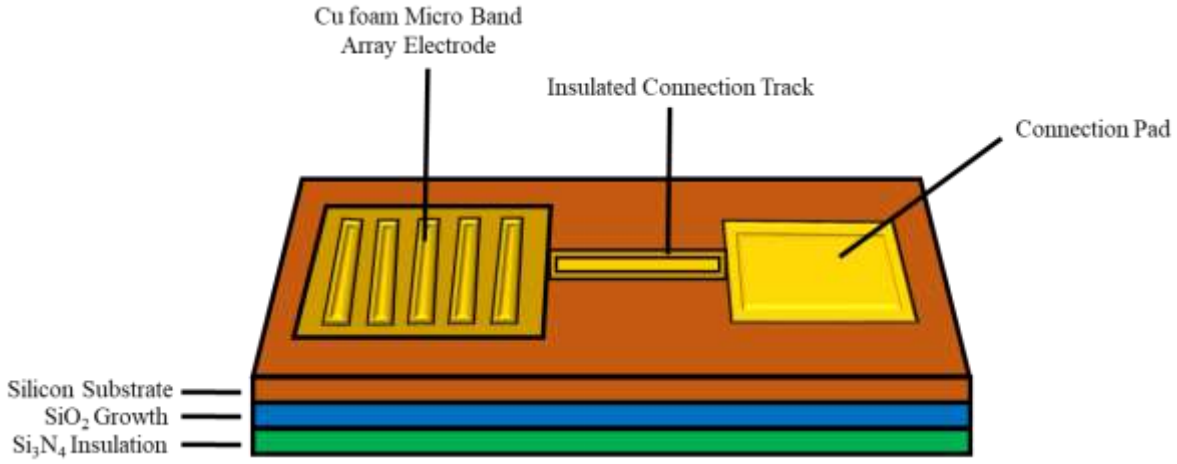

Figure 1.6: Schematic of a Cu-foam glucose sensor. *Adapted from Reference 140.*

1.7 Conclusion

CuO and Cu_2O nanoparticles are inexpensive, have high surface area and are extremely versatile for a range of applications. A variety of synthesis methods enables the preparation of CuO and Cu_2O nanoparticles with different morphologies including nanorods, nanospheres, nanocubes, nanoleaves etc. CuO and Cu_2O nanoparticles can also be immobilised onto a variety of support materials each adding their own properties to the nanoparticles and their capabilities. CuO and Cu_2O nanoparticles have a wide range of applications which are not exclusive to antimicrobial activity, gas sensors, glucose sensors, catalysts, photocatalysts and electrocatalysts. These applications, as well as the ability to control both the size and shape of the nanoparticles make CuO and Cu_2O nanoparticles desirable for many areas both in research and industry.

1.8 References

(1) Mikami, K.; Kido, Y.; Akaishi, Y.; Quitan, A.; Kida, T. Synthesis of Cu2O/CuO Nanocrystals and Their Application to H2S Sensing. *Sensors* **2019**, *19* (211).

(2) Akhavan, O.; Ghaderi, E. Cu and CuO Nanoparticles Immobilised by Silica Thin Films as Antibacterial Materials and Photocatalysts. *Surf. Coat. Technol.* **2010**, *205* (2010), 219–223.

(3) Song, M.; Zhao, J.; Li, H.; Yu, X.; Yang, X.; Zhang, L.; Yin, Z.; Wang, X. Preparation of Cu2O/Cu Porous Granular Films by in Situ Oxidation for Electrochemical Energy Storage. *J. Electroanal. Chem.* **2020**, *857*, 113755.

(4) Zhou, J.; Ma, L.; Song, H.; Wu, B.; Chen, X. Durable High-Rate Performance of CuO Hollow Nanoparticles/Graphene-Nanosheet Composite Anode Material for Lithium-Ion Batteries. *Electrochem. Commun.* **2011**, *13* (12), 1357–1360.

(5) Gawande, M. B.; Goswami, A.; Felpin, F.-X.; Asefa, T.; Huang, X.; Silva, R.; Zou, X.; Zboril, R.; Varma, R. S. Cu and Cu-Based Nanoparticles: Synthesis and Applications in Catalysis. *Chem. Rev.* **2016**, *116* (6), 3722–3811.

(6) Murali, D. S.; Kumar, S.; Choudhary, R. J.; Wadikar, A. D.; Jain, M. K.; Subrahmanyam, A. Synthesis of Cu2O from CuO Thin Films: Optical and Electrical Properties. *AIP Adv.* **2015**, *5* (4), 047143.

(7) Bigall, N. C.; Härtling, T.; Klose, M.; Simon, P.; Eng, L. M.; Eychmüller, A. Monodisperse Platinum Nanospheres with Adjustable Diameters from 10 to 100 Nm: Synthesis and Distinct Optical Properties. *Nano Lett.* **2008**, *8* (12), 4588–4592.

(8) Aparna, Y.; Enkateswara Rao, K. V.; Srinivasa Subbarao, P. Synthesis and Characterization of CuO Nano Particles by Novel Sol-Gel Method. *Int. Proc. Chem. Biol. Environ. Eng.* **2012**, *48* (30), 156–160.

(9) Ananth, A.; Dharaneedharan, S.; Heo, M.-S.; Mok, Y. S. Copper Oxide Nanomaterials: Synthesis, Characterization and Structure-Specific Antibacterial Performance. *Chem. Eng. J.* **2015**, *262*, 179–188.

(10) Wang, H.; Xu, J.-Z.; Zhu, J.-J.; Chen, H.-Y. Preparation of CuO Nanoparticles by Microwave Irradiation. *J. Cryst. Growth* **2002**, *244* (1), 88–94.

(11) Rawat, R. S. Dense Plasma Focus - From Alternative Fusion Source to Versatile High Energy Density Plasma Source for Plasma Nanotechnology. *J. Phys. Conf. Ser.* **2015**, *591*, 012021.

(12) R. Jana, N.; L. Wang, Z.; K. Sau, T.; Pal, T. Seed-Mediated Growth Method to Prepare Cubic Copper Nanoparticles. *Currnet Sci.* **2000**, *79* (9).

(13) Siddiqui, H.; Qureshi, M. S.; Haque, F. Z. Structural and Optical Properties of CuO Nanocubes Prepared Through Simple Hydrothermal Route. *Int. J. Sci. Eng. Res.* **2014**, *5* (3).

(14) Wang, D.; Yu, D.; Mo, M.; Liu, X.; Qian, Y. Seed-Mediated Growth Approach to Shape-Controlled Synthesis of Cu2O Particles. *J. Colloid Interface Sci.* **2003**, *261* (2), 565–568.

(15) Zhang, X.; Wang, G.; Gu, A.; Wu, H.; Fang, B. Preparation of Porous Cu2O Octahedron and Its Application as L-Tyrosine Sensors. *Solid State Commun.* **2008**, *148* (11–12), 525–528.

(16) Kuo, C.-H.; Chen, C.-H.; Huang, M. H. Seed-Mediated Synthesis of Monodispersed Cu2O Nanocubes with Five Different Size Ranges from 40 to 420 Nm. *Adv. Funct. Mater.* **2007**, *17* (18), 3773–3780.

(17) Liu, W.; Chai, G.; Zhang, J.; Wang, M.; Dai, Y.; Yang, Q. Preparation of Cu_2O Nanocubes with Different Sizes and Rough Surfaces by a Seed-Mediated Self-Assembly Process and Their Application as a Non-Enzymatic Glucose Sensor. *New J. Chem.* **2020**, *44* (36), 15662–15670.

(18) Liu, C. M.; Guo, L.; Xu, H. B.; Wu, Z. Y.; Weber, J. Seed-Mediated Growth and Properties of Copper Nanoparticles, Nanoparticle 1D Arrays and Nanorods. *Microelectron. Eng.* **2003**, *66* (1–4), 107–114.

(19) Krishnan, S. K.; Prokhorov, E.; Bahena, D.; Esparza, R.; Meyyappan, M. Chitosan-Covered Pd@Pt Core–Shell Nanocubes for Direct Electron Transfer in Electrochemical Enzymatic Glucose Biosensor. *ACS Omega* **2017**, *2* (5), 1896–1904.

(20) Agunloye, E.; Panariello, L.; Gavriilidis, A.; Mazzei, L. A Model for the Formation of Gold Nanoparticles in the Citrate Synthesis Method. *Chem. Eng. Sci.* **2018**, *191*, 318–331.

(21) Zhang, X.; Wang, G.; Zhang, W.; Hu, N.; Wu, H.; Fang, B. Seed-Mediated Growth Method for Epitaxial Array of CuO Nanowires on Surface of Cu Nanostructures and Its Application as a Glucose Sensor. *J. Phys. Chem. C* **2008**, *112* (24), 8856–8862.

(22) Zhang, X.; Gu, A.; Wang, G.; Wang, W.; Wu, H.; Fang, B. Seed-Mediated Preparation of CuO Nanoflowers and Their Application as Hydrazine Sensor. *Chem. Lett.* **2009**, *38* (5), 466–467.

(23) Umar, A. A.; Oyama, M. A Seed-Mediated Growth Method for Vertical Array of Single-Crystalline CuO Nanowires on Surfaces. *Cryst. Growth Des.* **2007**, *7* (12), 2404–2409.

(24) Kshirsagar, J.; Shrivastava, R.; Adwani, P. Preparation and Characterization of Copper Oxide Nanoparticles and Determination of Enhancement in Critical Heat Flux. *Therm. Sci.* **2017**, *21* (1 Part A), 233–242.

(25) Dadi, R.; Azouani, R.; Traore, M.; Mielcarek, C.; Kanaev, A. Antibacterial Activity of ZnO and CuO Nanoparticles against Gram Positive and Gram Negative Strains. *Mater. Sci. Eng. C* **2019**, *104*, 109968.

(26) Etefagh, R.; Azhir, E.; Shahtahmasebi, N. Synthesis of CuO Nanoparticles and Fabrication of Nanostructural Layer Biosensors for Detecting Aspergillus Niger Fungi. *Sci. Iran.* **2013**, *20* (3), 1055–1058.

(27) Karthik, K.; Victor Jaya, N.; Kanagaraj, M.; Arumugam, S. Temperature-Dependent Magnetic Anomalies of CuO Nanoparticles. *Solid State Commun.* **2011**, *151* (7), 564–568.

(28) Dörner, L.; Cancellieri, C.; Rheingans, B.; Walter, M.; Kägi, R.; Schmutz, P.; Kovalenko, M. V.; Jeurgens, L. P. H. Cost-Effective Sol-Gel Synthesis of Porous CuO Nanoparticle Aggregates with Tunable Specific Surface Area. *Sci. Rep.* **2019**, *9* (1), 11758.

(29) Grigore, M.; Biscu, E.; Holban, A.; Gestal, M.; Grumezescu, A. Methods of Synthesis, Properties and Biomedical Applications of CuO Nanoparticles. *Pharmaceuticals* **2016**, *9* (4), 75.

(30) Suleiman, M.; Mousa, M.; Hussein, A.; Hammouti, B.; Hadda, T. B.; Warad, I. Copper(II)-Oxide Nanostructures: Synthesis, Characterizations and Their Applications–Review. *J. Mater. Environ. Sci.* **2013**, *4* (5), 792–797.

(31) Jayaprakash, J.; Srinivasan, N.; Chandrasekaran, P. Surface Modifications of CuO Nanoparticles Using Ethylene Diamine Tetra Acetic Acid as a Capping Agent by Sol–Gel Routine. *Spectrochim. Acta. A. Mol. Biomol. Spectrosc.* **2014**, *123*, 363–368.

(32) Shen, X.-P.; Liu, H.-J.; Pan, L.; Chen, K.-M.; Hong, J.-M.; Xu, Z. An Efficient Template Pathway to Synthesis of Ordered Metal Oxide Nanotube Arrays Using Metal Acetylacetonates as Single-Source Molecular Precursors. *Chem. Lett.* **2004**, *33* (9), 1128–1129.

(33) Zhang, Q.; Zhang, K.; Xu, D.; Yang, G.; Huang, H.; Nie, F.; Liu, C.; Yang, S. CuO Nanostructures: Synthesis, Characterization, Growth Mechanisms, Fundamental Properties, and Applications. *Prog. Mater. Sci.* **2014**, *60*, 208–337.

(34) Yang, C.; Su, X.; Wang, J.; Cao, X.; Wang, S.; Zhang, L. Facile Microwave-Assisted Hydrothermal Synthesis of Varied-Shaped CuO Nanoparticles and Their Gas Sensing Properties. *Sens. Actuators B Chem.* **2013**, *185*, 159–165.

(35) Xiao, H.-M.; Fu, S.-Y.; Zhu, L.-P.; Li, Y.-Q.; Yang, G. Controlled Synthesis and Characterization of CuO Nanostructures through a Facile Hydrothermal Route in the Presence of Sodium Citrate. *Eur. J. Inorg. Chem.* **2007**, *2007* (14), 1966–1971.

(36) Kannaki, K.; Ramesh, P. S.; Geetha, D. Hydrothermal Synthesis of CuO Nanostructure and Their Characterizations. *Int. J. Sci. Eng. Res.* **2012**, *3* (9).

(37) Chen, D.; Shen, G.; Tang, K.; Qian, Y. Large-Scale Synthesis of CuO Shuttle-like Crystals via a Convenient Hydrothermal Decomposition Route. *J. Cryst. Growth* **2003**, *254* (1–2), 225–228.

(38) Outokesh, M.; Hosseinpour, M.; Ahmadi, S. J.; Mousavand, T.; Sadjadi, S.; Soltanian, W. Hydrothermal Synthesis of CuO Nanoparticles: Study on Effects of Operational Conditions on Yield, Purity, and Size of the Nanoparticles. *Ind. Eng. Chem. Res.* **2011**, *50* (6), 3540–3554.

(39) Lan, X.; Zhang, J.; Gao, H.; Wang, T. Morphology-Controlled Hydrothermal Synthesis and Growth Mechanism of Microcrystal Cu2O. *CrystEngComm* **2011**, *13* (2), 633–636.

(40) Zhang, F.; Li, Y.; Gu, Y.; Wang, Z.; Wang, C. One-Pot Solvothermal Synthesis of a Cu2O/Graphene Nanocomposite and Its Application in an Electrochemical Sensor for Dopamine. *Microchim. Acta* **2011**, *173* (1–2), 103–109.

(41) Khan, M. A.; Ullah, M.; Iqbal, T.; Mahmood, H.; Khan, A. A.; Shafique, M.; Majid, A.; Ahmed, A.; Khan, N. A. Surfactant Assisted Synthesis of Cuprous Oxide (Cu2O) Nanoparticles via Solvothermal Process. *Nanosci. Nanotechnol. Res.* **2015**, *3* (1), 16–22.

(42) Liu, Q.; Liu, H.; Liang, Y.; Xu, Z.; Yin, G. Large-Scale Synthesis of Single-Crystalline CuO Nanoplatelets by a Hydrothermal Process. *Mater. Res. Bull.* **2006**, *41* (4), 697–702.

(43) Tang, X.; Ren, L.; Sun, L.; Tian, W.; Cao, M.; Hu, C. A Solvothermal Route to Cu2O Nanocubes and Cu Nanoparticles1. *Chem. Res. Chin. Univ.* **2006**, *22* (5), 547–551.

(44) Nabiyouni, G.; Ghanbari, D.; Abbasian, H. Sonochemical-Assisted Synthesis of Copper Oxide Nanoparticles and Its Application as Humidity Sensor. *J. Nanostructures* **2014**, *3*, 429–434.

(45) Saravanan, S.; Sivasankar, T. Effect of Ultrasound Power and Calcination Temperature on the Sonochemical Synthesis of Copper Oxide Nanoparticles for Textile Dyes Treatment. *Environ. Prog. Sustain. Energy* **2016**, *35* (3), 669–679.

(46) Anandan, S.; Lee, G.-J.; Wu, J. J. Sonochemical Synthesis of CuO Nanostructures with Different Morphology. *Ultrason. Sonochem.* **2012**, *19* (3), 682–686.

(47) Mosleh, S.; Rahimi, M. R.; Ghaedi, M.; Dashtian, K.; Hajati, S. Sonochemical-Assisted Synthesis of CuO/Cu2O/Cu Nanoparticles as Efficient Photocatalyst for Simultaneous Degradation of Pollutant Dyes in Rotating Packed Bed Reactor: LED Illumination and Central Composite Design Optimization. *Ultrason. Sonochem.* **2018**, *40*, 601–610.

(48) Kim, D.-S.; Kim, J.-C.; Kim, B.-K.; Kim, D.-W. One-Pot Low-Temperature Sonochemical Synthesis of CuO Nanostructures and Their Electrochemical Properties. *Ceram. Int.* **2016**, *42* (16), 19454–19460.

(49) Eddy Jai Poinern, G. Rapid Sonochemical Synthesis and Characterisation of Copper Oxide Nanoparticles from Schweizer's Reagent. *Int. J. Sci.* **2015**, *1* (11), 23–29.

(50) Wongpisutpaisan, N.; Charoonsuk, P.; Vittayakorn, N.; Pecharapa, W. Sonochemical Synthesis and Characterization of Copper Oxide Nanoparticles. *Energy Procedia* **2011**, *9*, 404–409.

(51) Karunakaran, C.; Manikandan, G.; Gomathisankar, P. Microwave, Sonochemical and Combustion Synthesized CuO Nanostructures and Their Electrical and Bactericidal Properties. *J. Alloys Compd.* **2013**, *580*, 570–577.

(52) Bhosale, M. A.; Bhanage, B. M. A Simple Approach for Sonochemical Synthesis of Cu 2 O Nanoparticles with High Catalytic Properties. *Adv. Powder Technol.* **2016**, *27* (1), 238–244.

(53) Silva, N.; Ramírez, S.; Díaz, I.; Garcia, A.; Hassan, N. Easy, Quick, and Reproducible Sonochemical Synthesis of CuO Nanoparticles. *Materials* **2019**, *12* (5), 804.

(54) Mohd Yusof, N. S.; Ashokkumar, M. Ultrasonic Modification of Micelle Nanostructures. In *Handbook of Ultrasonics and Sonochemistry*; Springer Singapore: Singapore, 2016; pp 491–524.

(55) Kaviyarasan, K.; Anandan, S.; Mangalaraja, R. V.; Sivasankar, T.; Ashokkumar, M. Sonochemical Synthesis of Cu2O Nanocubes for Enhanced Chemiluminescence Applications. *Ultrason. Sonochem.* **2016**, *29*, 388–393.

(56) Xu, L.; Jiang, L.-P.; Zhu, J.-J. Sonochemical Synthesis and Photocatalysis of Porous Cu $_2$ O Nanospheres with Controllable Structures. *Nanotechnology* **2009**, *20* (4), 045605.

(57) Dagher, S.; Haik, Y.; Ayesh, A. I.; Tit, N. Synthesis and Optical Properties of Colloidal CuO Nanoparticles. *J. Lumin.* **2014**, *151*, 149–154.

(58) Felix, S.; Chakkravarthy, R. B. P.; Grace, A. N. Microwave Assisted Synthesis of Copper Oxide and Its Application in Electrochemical Sensing. *IOP Conf. Ser. Mater. Sci. Eng.* **2015**, *73*, 012115.

(59) Qiu, G.; Dharmarathna, S.; Zhang, Y.; Opembe, N.; Huang, H.; Suib, S. L. Facile Microwave-Assisted Hydrothermal Synthesis of CuO Nanomaterials and Their Catalytic and Electrochemical Properties. *J. Phys. Chem. C* **2012**, *116* (1), 468–477.

(60) Shaalan, N. M.; Rashad, M.; Abdel-Rahim, M. A. CuO Nanoparticles Synthesized by Microwave-Assisted Method for Methane Sensing. *Opt. Quantum Electron.* **2016**, *48* (12), 531.

(61) Rashad, M.; Rüsing, M.; Berth, G.; Lischka, K.; Pawlis, A. CuO and Co3O4 Nanoparticles: Synthesis, Characterizations, and Raman Spectroscopy. *J. Nanomater.* **2013**, *2013*, 1–6.

(62) Bhattacharjee, A.; Ahmaruzzaman, M. Microwave Assisted Facile and Green Route for Synthesis of CuO Nanoleaves and Their Efficacy as a Catalyst for Reduction and Degradation of Hazardous Organic Compounds. *J. Photochem. Photobiol. Chem.* **2018**, *353*, 215–228.

(63) Moura, A. P.; Cavalcante, L. S.; Sczancoski, J. C.; Stroppa, D. G.; Paris, E. C.; Ramirez, A. J.; Varela, J. A.; Longo, E. Structure and Growth Mechanism of CuO Plates Obtained by Microwave-Hydrothermal without Surfactants. *Adv. Powder Technol.* **2010**, *21* (2), 197–202.

(64) Kuo, C. Y.; Wu, C. H.; Wu, J. T.; Chen, Y. C. Preparation of Immobilized Cu2O Using Microwave Irradiation and Its Catalytic Activity for Bisphenol A: Comparisons of Cu2O/H2O2 and Visible-Light/Cu2O/H2O2 Systems. *Water Sci. Technol.* **2014**, *70* (8), 1428–1433.

(65) Wu, Z.; Shao, M.; Zhang, W.; Ni, Y. Large-Scale Synthesis of Uniform Cu2O Stellar Crystals via Microwave-Assisted Route. *J. Cryst. Growth* **2004**, *260* (3–4), 490–493.

(66) 조영식; 허영덕. Microwave Assisted Synthesis of Cu_2O Crystals with Morphological Evolution from Octapod to Octahedron. *Bull. Korean Chem. Soc.* **2014**, *35* (1), 309–312.

(67) Su, C.-K.; Tseng, H.-H. 3D-Printed CuO Nanoparticle–Functionalized Flow Reactor Enables Online Fluorometric Monitoring of Glucose. *Microchim. Acta* **2019**, *186* (7).

(68) Wu, Q.; He, L.; Jiang, Z. W.; Li, Y.; Cao, Z. M.; Huang, C. Z.; Li, Y. F. CuO Nanoparticles Derived from Metal-Organic Gel with Excellent Electrocatalytic and Peroxidase-Mimicking Activities for Glucose and Cholesterol Detection. *Biosens. Bioelectron.* **2019**, *145*, 111704.

(69) Sarkar, J.; Chakraborty, N.; Chatterjee, A.; Bhattacharjee, A.; Dasgupta, D.; Acharya, K. Green Synthesized Copper Oxide Nanoparticles Ameliorate Defence and Antioxidant Enzymes in Lens Culinaris. *Nanomaterials* **2020**, *10* (2), 312.

(70) Ananda Murthy, H. C.; Abebe, B.; C H, P.; Shantaveerayya, K. A Review on Green Synthesis and Applications of Cu and CuO Nanoparticles. *Mater. Sci. Res. India* **2018**, *15* (3), 279–295.

(71) Taghavi Fardood, S.; Ramazani, A.; Joo, S. W. Green Chemistry Approach for the Synthesis of Copper Oxide Nanoparticles Using Tragacanth Gel and Their Structural Characterization. *J. Struct. Chem.* **2018**, *59* (2), 482–486.

(72) Ashok, A.; Kumar, A.; Tarlochan, F. Highly Efficient Nonenzymatic Glucose Sensors Based on CuO Nanoparticles. *Appl. Surf. Sci.* **2019**, *481*, 712–722.

(73) Varma, A.; Mukasyan, A. S.; Rogachev, A. S.; Manukyan, K. V. Solution Combustion Synthesis of Nanoscale Materials. *Chem. Rev.* **2016**, *116* (23), 14493–14586.

(74) Wang, Q.; Ming, M.; Niu, S.; Zhang, Y.; Fan, G.; Hu, J.-S. Scalable Solid-State Synthesis of Highly Dispersed Uncapped Metal (Rh, Ru, Ir) Nanoparticles for Efficient Hydrogen Evolution. *Adv. Energy Mater.* **2018**, *8* (31), 1801698.

(75) Debnath, D.; Kim, C.; Kim, S. H.; Geckeler, K. E. Solid-State Synthesis of Silver Nanoparticles at Room Temperature: Poly(Vinylpyrrolidone) as a Tool: Solid-State Synthesis of Silver Nanoparticles at Room Temperature: Poly(Vinylpyrrolidone) as a Tool. *Macromol. Rapid Commun.* **2010**, *31* (6), 549–553.

(76) Swihart, M. T. Vapor-Phase Synthesis of Nanoparticles. *Curr. Opin. Colloid Interface Sci.* **2003**, *8* (1), 127–133.

(77) Cao, Y.; Jia, D.; Zhou, J.; Sun, Y. Simple Solid-State Chemical Synthesis of $ZnSnO_3$ Nanocubes and Their Application as Gas Sensors. *Eur. J. Inorg. Chem.* **2009**, *2009* (27), 4105–4109.

(78) Zoolfakar, A. S.; Rani, R. A.; Morfa, A. J.; O'Mullane, A. P.; Kalantar-zadeh, K. Nanostructured Copper Oxide Semiconductors: A Perspective on Materials, Synthesis Methods and Applications. *J Mater Chem C* **2014**, *2* (27), 5247–5270.

(79) Chiang, C.-Y.; Aroh, K.; Ehrman, S. H. Copper Oxide Nanoparticle Made by Flame Spray Pyrolysis for Photoelectrochemical Water Splitting – Part I. CuO Nanoparticle Preparation. *Int. J. Hydrog. Energy* **2012**, *37* (6), 4871–4879.

(80) Anu, A.; Abdul Khadar, M. Grain Size Tuning of Nanostructured Cu $_2$ O Films through Vapour Phase Supersaturation Control and Their Characterization for Practical Applications. *AIP Adv.* **2015**, *5* (9), 097176.

(81) Shi, G.; Liu, J.; Chen, B.; Bao, Y.; Xu, J. Phase-Controlled Growth of Cubic Phase CuO Nanoparticles by Chemical Vapor Deposition: Phase-Controlled Growth of Cubic Phase CuO Nanoparticles. *Phys. Status Solidi A* **2017**, *214* (10), 1700041.

(82) Zhang, J. X. J.; Hoshino, K. Fundamentals of Nano/Microfabrication and Scale Effect. In *Molecular Sensors and Nanodevices*; Elsevier, 2019; pp 43–111.

(83) Vidyasagar, C. C.; Naik, Y. A.; Venkatesh, T. G.; Viswanatha, R. Solid-State Synthesis and Effect of Temperature on Optical Properties of Cu–ZnO, Cu–CdO and CuO Nanoparticles. *Powder Technol.* **2011**, *214* (3), 337–343.

(84) Vidyasagar, C. C.; Arthoba Naik, Y.; Venkatesha, T. G.; Viswanatha, R. Solid-State Synthesis and Effect of Temperature on Optical Properties of CuO Nanoparticles. *Nano-Micro Lett.* **2012**, *4* (2), 73–77.

(85) Patel, V. K.; Bhattacharya, S. Solid State Green Synthesis and Catalytic Activity of CuO Nanorods in Thermal Decomposition of Potassium Periodate. *Mater. Res. Express* **2017**, *4* (9), 095012.

(86) Li, P.; Lv, W.; Ai, S. Green and Gentle Synthesis of Cu $_2$ O Nanoparticles Using Lignin as Reducing and Capping Reagent with Antibacterial Properties. *J. Exp. Nanosci.* **2016**, *11* (1), 18–27.

(87) Radi, A.; Pradhan, D.; Sohn, Y.; Leung, K. T. Nanoscale Shape and Size Control of Cubic, Cuboctahedral, and Octahedral Cu−Cu $_2$ O Core−Shell Nanoparticles on Si(100) by One-Step, Templateless, Capping-Agent-Free Electrodeposition. *ACS Nano* **2010**, *4* (3), 1553–1560.

(88) Shui, A.; Zhu, W.; Xu, L.; Qin, D.; Wang, Y. Green Sonochemical Synthesis of Cupric and Cuprous Oxides Nanoparticles and Their Optical Properties. *Ceram. Int.* **2013**, *39* (8), 8715–8722.

(89) Yamada, Y.; Yano, K.; Fukuzumi, S. Catalytic Application of Shape-Controlled Cu $_2$ O Particles Protected by Co $_3$ O $_4$ Nanoparticles for Hydrogen Evolution from Ammonia Borane. *Energy Env. Sci* **2012**, *5* (1), 5356–5363.

(90) Bai, Y.; Yang, T.; Gu, Q.; Cheng, G.; Zheng, R. Shape Control Mechanism of Cuprous Oxide Nanoparticles in Aqueous Colloidal Solutions. *Powder Technol.* **2012**, *227*, 35–42.

(91) Shah, J.; Ranjan, M.; Gupta, S. K.; Satyaprasad, A.; Chaki, S.; Sonvane, Y. Reaction Temperature Dependent Shape-Controlled Studies of Copper-Oxide Nanocrystals. *Mater. Res. Express* **2018**, *5* (6), 065037.

(92) Zhu, Q.-L.; Xu, Q. Immobilization of Ultrafine Metal Nanoparticles to High-Surface-Area Materials and Their Catalytic Applications. *Chem* **2016**, *1* (2), 220–245.

(93) Ndolomingo, M. J.; Bingwa, N.; Meijboom, R. Review of Supported Metal Nanoparticles: Synthesis Methodologies, Advantages and Application as Catalysts. *J. Mater. Sci.* **2020**, *55* (15), 6195–6241.

(94) Yao, X.; Tang, C.; Gao, F.; Dong, L. Research Progress on the Catalytic Elimination of Atmospheric Molecular Contaminants over Supported Metal-Oxide Catalysts. *Catal. Sci. Technol.* **2014**, *4* (9), 2814.

(95) Martínez-Arias, A.; Hungría, A. B.; Fernández-García, M.; Conesa, J. C.; Munuera, G. Interfacial Redox Processes under CO/O2 in a Nanoceria-Supported Copper Oxide Catalyst. *J. Phys. Chem. B* **2004**, *108* (46), 17983–17991.

(96) Shelke, S. N.; Bankar, S. R.; Mhaske, G. R.; Kadam, S. S.; Murade, D. K.; Bhorkade, S. B.; Rathi, A. K.; Bundaleski, N.; Teodoro, O. M. N. D.; Zboril, R.; Varma, R. S.; Gawande, M. B. Iron Oxide-Supported Copper Oxide Nanoparticles (Nanocat-Fe-CuO): Magnetically Recyclable Catalysts for the Synthesis of Pyrazole Derivatives, 4-Methoxyaniline, and Ullmann-Type Condensation Reactions. *ACS Sustain. Chem. Eng.* **2014**, *2* (7), 1699–1706.

(97) Kiritoshi, S.; Iwasa, T.; Araki, K.; Kawabata, Y.; Taketsugu, T.; Hinokuma, S.; Machida, M. Supported Binary CuOx–Pt Catalysts with High Activity and Thermal Stability for the Combustion of NH3as a Carbon-Free Energy Source. *RSC Adv.* **2018**, *8* (72), 41491–41498.

(98) El-Nahhal, I. M.; Salem, J. K.; Selmane, M.; Kodeh, F. S.; Ebtihan, H. A. Synthesis and Structural Characterization of ZnO and CuO Nanoparticles Supported Mesoporous Silica SBA-15. *Chem. Phys. Lett.* **2017**, *667*, 165–171.

(99) Akhavan, O.; Ghaderi, E. Cu and CuO Nanoparticles Immobilized by Silica Thin Films as Antibacterial Materials and Photocatalysts. *Surf. Coat. Technol.* **2010**, *205* (1), 219–223.

(100) Yu, X.; Zhao, Z.; Wei, Y.; Liu, J.; Li, J.; Duan, A.; Jiang, G. Three-Dimensionally Ordered Macroporous SiO2 -Supported Transition Metal Oxide Catalysts: Facile

Synthesis and High Catalytic Activity for Diesel Soot Combustion. *RSC Adv.* **2015**, *5* (61), 49780–49790.

(101) Zhu, J.; Zeng, G.; Nie, F.; Xu, X.; Chen, S.; Han, Q.; Wang, X. Decorating Graphene Oxide with CuO Nanoparticles in a Water–Isopropanol System. *Nanoscale* **2010**, *2* (6), 988.

(102) Hummers, W. S.; Offeman, R. E. Preparation of Graphitic Oxide. *J. Am. Chem. Soc.* **1958**, *80* (6), 1339–1339.

(103) White, B.; Yin, M.; Hall, A.; Le, D.; Stolbov, S.; Rahman, T.; Turro, N.; O'Brien, S. Complete CO Oxidation over Cu $_2$ O Nanoparticles Supported on Silica Gel. *Nano Lett.* **2006**, *6* (9), 2095–2098.

(104) Mkhalid, I. A.; Shawky, A. Cu-Supported Cu2O Nanoparticles: Optimized Photodeposition Enhances the Visible Light Photodestruction of Atrazine. *J. Alloys Compd.* **2021**, *853*, 157040.

(105) Wang, G.; van den Berg, R.; de Mello Donega, C.; de Jong, K. P.; de Jongh, P. E. Silica-Supported Cu2O Nanoparticles with Tunable Size for Sustainable Hydrogen Generation. *Appl. Catal. B Environ.* **2016**, *192*, 199–207.

(106) Zhou, Z.; Lu, C.; Wu, X.; Zhang, X. Cellulose Nanocrystals as a Novel Support for CuO Nanoparticles Catalysts: Facile Synthesis and Their Application to 4-Nitrophenol Reduction. *RSC Adv.* **2013**, *3* (48), 26066.

(107) Vainio, U.; Pirkkalainen, K.; Kisko, K.; Goerigk, G.; Kotelnikova, N. E.; Serimaa, R. Copper and Copper Oxide Nanoparticles in a Cellulose Support Studied Using Anomalous Small-Angle X-Ray Scattering. *Eur. Phys. J. D* **2007**, *42* (1), 93–101.

(108) Huang, J.; Zhu, Y.; Zhong, H.; Yang, X.; Li, C. Dispersed CuO Nanoparticles on a Silicon Nanowire for Improved Performance of Nonenzymatic H2O2 Detection. *ACS Appl. Mater. Interfaces* **2014**, *6* (10), 7055–7062.

(109) Kamyabi, M.; Hajari, N. Low Potential and Non-Enzymatic Hydrogen Peroxide Sensor Based on Copper Oxide Nanoparticle on Activated Pencil Graphite Electrode. *J. Braz. Chem. Soc.* **2016**.

(110) Honraedt, A.; Le Callonnec, F.; Le Grognec, E.; Fernandez, V.; Felpin, F.-X. C–H Arylation of Benzoquinone in Water through Aniline Activation: Synergistic Effect of Graphite-Supported Copper Oxide Nanoparticles. *J. Org. Chem.* **2013**, *78* (9), 4604–4609.

(111) Jung, D.-W.; Jeong, J.-H.; Kong, B.-S.; Lee, J. K.; Oh, E.-S. Preparation of Nano-Sized Graphite-Supported CuO and Cu-Sn as Active Materials in Lithium Ion Batteries. *J. Nanosci. Nanotechnol.* **2012**, *12* (4), 3317–3321.

(112) Peternela, J.; Silva, M. F.; Vieira, M. F.; Bergamasco, R.; Vieira, A. M. S. Synthesis and Impregnation of Copper Oxide Nanoparticles on Activated Carbon through Green Synthesis for Water Pollutant Removal. *Mater. Res.* **2017**, *21* (1).

(113) Boruban, C.; Esenturk, E. N. Activated Carbon-Supported CuO Nanoparticles: A Hybrid Material for Carbon Dioxide Adsorption. *J. Nanoparticle Res.* **2018**, *20* (3), 59.

(114) Ma, T.-Y.; Yuan, Z.-Y. Periodic Mesoporous Titanium Phosphonate Spheres for High Dispersion of CuO Nanoparticles. *Dalton Trans.* **2010**, *39* (40), 9570.

(115) Hu, R.; Yang, P.; Pan, Y.; Li, Y.; He, Y.; Feng, J.; Li, D. Synthesis of a Highly Dispersed CuO Catalyst on CoAl-HT for the Epoxidation of Styrene. *Dalton Trans* **2017**, *46* (39), 13463–13471.

(116) Scuderi, V.; Amiard, G.; Boninelli, S.; Scalese, S.; Miritello, M.; Sberna, P. M.; Impellizzeri, G.; Privitera, V. Photocatalytic Activity of CuO and Cu2O Nanowires. *Mater. Sci. Semicond. Process.* **2016**, *42*, 89–93.

(117) Baghriche, O.; Rtimi, S.; Pulgarin, C.; Kiwi, J. Polystyrene CuO/Cu 2 O Uniform Films Inducing MB-Degradation under Sunlight. *Catal. Today* **2017**, *284*, 77–83.

(118) Li, Q.; Xu, P.; Zhang, B.; Tsai, H.; Zheng, S.; Wu, G.; Wang, H.-L. Structure-Dependent Electrocatalytic Properties of Cu $_2$ O Nanocrystals for Oxygen Reduction Reaction. *J. Phys. Chem. C* **2013**, *117* (27), 13872–13878.

(119) Grirrane, A.; Corma, A.; Garcia, H. Stereoselective Single (Copper) or Double (Platinum) Boronation of Alkynes Catalyzed by Magnesia-Supported Copper Oxide or Platinum Nanoparticles. *Chem. - Eur. J.* **2011**, *17* (8), 2467–2478.

(120) Patil, S.; Mane, A.; Dhongade-Desai, S. CuO Nanoparticles as a Reusable Catalyst for the Synthesis of 1H-Pyrazolo[1,2-b]Phthalazine-5,10-Dione Derivatives under Solvent-Free Conditions. *J. Iran. Chem. Soc.* **2019**, *16* (8), 1665–1675.

(121) Akhavan, O.; Azimirad, R.; Safa, S.; Hasani, E. CuO/Cu(OH)2 Hierarchical Nanostructures as Bactericidal Photocatalysts. *J. Mater. Chem.* **2011**, *21* (26), 9634.

(122) Katwal, R.; Kaur, H.; Sharma, G.; Naushad, Mu.; Pathania, D. Electrochemical Synthesized Copper Oxide Nanoparticles for Enhanced Photocatalytic and Antimicrobial Activity. *J. Ind. Eng. Chem.* **2015**, *31*, 173–184.

(123) Pandiyarajan, T.; Saravanan, R.; Karthikeyan, B.; Gracia, F.; Mansilla, H. D.; Gracia-Pinilla, M. A.; Mangalaraja, R. V. Sonochemical Synthesis of CuO Nanostructures and Their Morphology Dependent Optical and Visible Light Driven Photocatalytic Properties. *J. Mater. Sci. Mater. Electron.* **2017**, *28* (3), 2448–2457.

(124) Liu, X.; Tang, J.; Wang, L.; Liu, R. Mechanism of CuO Nano-Particles on Stimulating Production of Actinorhodin in Streptomyces Coelicolor by Transcriptional Analysis. *Sci. Rep.* **2019**, *9* (1).

(125) Yurderi, M.; Bulut, A.; Ertas, İ. E.; Zahmakiran, M.; Kaya, M. Supported Copper–Copper Oxide Nanoparticles as Active, Stable and Low-Cost Catalyst in the Methanolysis of Ammonia–Borane for Chemical Hydrogen Storage. *Appl. Catal. B Environ.* **2015**, *165*, 169–175.

(126) Morones, J. R.; Elechiguerra, J. L.; Camacho, A.; Holt, K.; Kouri, J. B.; Ramírez, J. T.; Yacaman, M. J. The Bactericidal Effect of Silver Nanoparticles. *Nanotechnology* **2005**, *16* (10), 2346–2353.

(127) Loomba, L.; Scarabelli, T. Metallic Nanoparticles and Their Medicinal Potential. Part I: Gold and Silver Colloids. *Ther. Deliv.* **2013**, *4* (7), 859–873.

(128) Ren, G.; Hu, D.; Cheng, E. W. C.; Vargas-Reus, M. A.; Reip, P.; Allaker, R. P. Characterisation of Copper Oxide Nanoparticles for Antimicrobial Applications. *Int. J. Antimicrob. Agents* **2009**, *33* (6), 587–590.

(129) Hans, M.; Erbe, A.; Mathews, S.; Chen, Y.; Solioz, M.; Mücklich, F. Role of Copper Oxides in Contact Killing of Bacteria. *Langmuir* **2013**, *29* (52), 16160–16166.

(130) Su, X.; Chen, W.; Han, Y.; Wang, D.; Yao, J. In-Situ Synthesis of Cu2O on Cotton Fibers with Antibacterial Properties and Reusable Photocatalytic Degradation of Dyes. *Appl. Surf. Sci.* **2021**, *536*, 147945.

(131) Tavakoli, A.; Hashemzadeh, M. S. Inhibition of Herpes Simplex Virus Type 1 by Copper Oxide Nanoparticles. *J. Virol. Methods* **2020**, *275*, 113688.

(132) Hang, X.; Peng, H.; Song, H.; Qi, Z.; Miao, X.; Xu, W. Antiviral Activity of Cuprous Oxide Nanoparticles against Hepatitis C Virus in Vitro. *J. Virol. Methods* **2015**, *222*, 150–157.

(133) Bühler, S.; Bartenschlager, R. New Targets for Antiviral Therapy of Chronic Hepatitis C. *Liver Int.* **2012**, *32*, 9–16.

(134) Chen, Z.; Gao, S.; Jin, M.; Sun, S.; Lu, J.; Yang, P.; Bond, P. L.; Yuan, Z.; Guo, J. Physiological and Transcriptomic Analyses Reveal CuO Nanoparticle Inhibition of Anabolic and Catabolic Activities of Sulfate-Reducing Bacterium. *Environ. Int.* **2019**, *125*, 65–74.

(135) Wu, W.; Zhao, W.; Wu, Y.; Zhou, C.; Li, L.; Liu, Z.; Dong, J.; Zhou, K. Antibacterial Behaviors of Cu2O Particles with Controllable Morphologies in Acrylic Coatings. *Appl. Surf. Sci.* **2019**, *465*, 279–287.

(136) Domagała, K.; Jacquin, C.; Borlaf, M.; Sinnet, B.; Julian, T.; Kata, D.; Graule, T. Efficiency and Stability Evaluation of Cu2O/MWCNTs Filters for Virus Removal from Water. *Water Res.* **2020**, *179*, 115879.

(137) Giannousi, K.; Sarafidis, G.; Mourdikoudis, S.; Pantazaki, A.; Dendrinou-Samara, C. Selective Synthesis of Cu_2O and Cu/Cu_2O NPs: Antifungal Activity to Yeast *Saccharomyces Cerevisiae* and DNA Interaction. *Inorg. Chem.* **2014**, *53* (18), 9657–9666.

(138) Rydosz, A. The Use of Copper Oxide Thin Films in Gas-Sensing Applications. *Coatings* **2018**, *8* (12), 425.

(139) Zhang, J.; Liu, J.; Peng, Q.; Wang, X.; Li, Y. Nearly Monodisperse Cu_2O and CuO Nanospheres: Preparation and Applications for Sensitive Gas Sensors. *Chem. Mater.* **2006**, *18* (4), 867–871.

(140) Juska, V. B.; Walcarius, A.; Pemble, M. E. Cu Nanodendrite Foams on Integrated Band Array Electrodes for the Nonenzymatic Detection of Glucose. *ACS Appl. Nano Mater.* **2019**, *2* (9), 5878–5889.

(141) Dhara, K.; Stanley, J.; T, R.; Nair, B. G.; T.G, S. B. Pt-CuO Nanoparticles Decorated Reduced Graphene Oxide for the Fabrication of Highly Sensitive Non-Enzymatic Disposable Glucose Sensor. *Sens. Actuators B Chem.* **2014**, *195*, 197–205.

(142) Park, H. J.; Choi, N.-J.; Kang, H.; Jung, M. Y.; Park, J. W.; Park, K. H.; Lee, D.-S. A Ppb-Level Formaldehyde Gas Sensor Based on CuO Nanocubes Prepared Using a Polyol Process. *Sens. Actuators B Chem.* **2014**, *203*, 282–288.

(143) Patil, P.; Nakate, U. T.; Nakate, Y. T.; Ambare, R. C. Acetaldehyde Sensing Properties Using Ultrafine CuO Nanoparticles. *Mater. Sci. Semicond. Process.* **2019**, *101*, 76–81.

(144) Navale, Y. H.; Navale, S. T.; Galluzzi, M.; Stadler, F. J.; Debnath, A. K.; Ramgir, N. S.; Gadkari, S. C.; Gupta, S. K.; Aswal, D. K.; Patil, V. B. Rapid Synthesis Strategy of CuO Nanocubes for Sensitive and Selective Detection of NO2. *J. Alloys Compd.* **2017**, *708*, 456–463.

Chapter Two:

Experimental

2. Experimental

2.1 Nanoparticle Synthesis

Synthesis of the Pt nanoparticles (NP) is a two-step seed mediated growth, the method of which was predetermined from previous research in the area by *Bigall et al.*[1] with a few modifications. The first modification was to scale down the reactants by a factor of ten and the second modification was to switch the Pt precursor of chloroplatinic acid hexahydrate (H_2PtCl_6) with potassium tetrachloroplatinate (K_2PtCl_4). The first step in the synthesis involved synthesizing the nanoparticle seed (~5 nm), which would then be later used to form the particles. Briefly, 46.4 mL of deionised (DI) water and a stir bar were added to a two-neck 100 mL round bottom flask, equipped with a reflux condenser, and heated to reflux. At this point 3.6 mL of 0.02% (w/v) K_2PtCl_4 solution was added. One minute later 1.1 mL of a 1% (w/v) sodium citrate and 0.05% (w/v) citric acid mixture was added to the round bottom. This was followed 30 s later by an addition of 0.55 mL of a mixture of $NaBH_4$ and 1% (w/v) sodium citrate and 0.05% (w/v) citric acid solution. The round bottom flask was then stoppered and the solution was allowed to reflux for 10 mins.

Once the seeds had cooled to room temperature they were then used to synthesise larger Pt NPs. For the seeded synthesis, 29 mL of DI water and 1 ml of the Pt NP seed solution were added to a two-neck round bottom flask equipped with a condenser and magnetic stir bar. Depending on the desired nanoparticle size, a different quantity of the 0.4 M Pt precursor solution (K_2PtCl_4) was added. In order to make ~10 nm particles 10 µL of the Pt precursor solution was added and in the case of ~30 nm particles that value was 45 µL. After addition of the Pt precursor, 0.5 mL of a solution containing 1% (w/v) sodium citrate and 1.25% (w/v) L – ascorbic acid was added to the flask. The solution was heated to reflux and aged for 20 min.

2.2 Nanoparticle Purification

After the NPs had been synthesised they were washed thoroughly with DI water and isolated by centrifugation to remove impurities before being used for deposition. For a typical synthesis 7.5 mL of Pt NP solution was placed into a centrifuge tube, giving four centrifuge tubes for each synthesis. The particles were centrifuged at 3000 rpm for 25 mins which produced a sediment that consisted of large NPs and was discarded. The supernatant in each of the tubes was transferred to four new tubes and placed back in the centrifuge for a period of 25 mins at 6000 rpm. The sediment was again discarded to remove larger NPs and the supernatant added to new tubes. To this solution, 2.5 mL of DI water was added and the particles were centrifuged at 8500 rpm for 85 mins. The supernatant was decanted and discarded. The sediment was further washed with 10 mL of DI water and collected by centrifugation. The Pt NPs were then redispersed in 7.5 mL of DI water. These washes were done in order to remove the unwanted NP which would ensure that the particles would be approximately uniform in size.

2.3 Preparation of 1,10-diaminodecane Solution

In order for the NPs to tether to the surface of the Cu substrates a molecule was needed in that would bond to both the Pt and the Cu surface. To achieve this, the Cu substrates were modified using a bifunctional, self-assembled monolayer (SAM). The molecule chosen for this purpose was 1,10-diaminodecane as the amino groups on either end form weak interactions with both the Cu surface and the Pt NPs to immobilise the NPs on the surface. A 10 mM 1,10-diaminodecane solution was made by dissolving 0.04 g in 25 mL of methanol which was sonicated for 20-30 s. The SAM solution was degassed using N_2 before use for better results.

2.4 Functionalisation of Copper Substrates

The Cu-coated wafers used had a native oxide layer which had to be removed prior to functionalisation of the surface. The substrates were first cut to the desired size of approximately 1 cm x 1 cm. During this time the 1% (w/v) citric acid solution was degassed with N_2 for 15 mins. The substrates were then degreased by sonicating in acetone for 3 min. The substrates were removed from the acetone and washed with isopropyl alcohol (IPA), dried with N_2 and placed into the citric acid solution for 10 min while under N_2 flow. After the 10 mins had elapsed the substrates were removed from the citric acid and quickly placed into a vial containing the SAM solution for 24 h. The sample vial was stoppered and sealed with Parafilm to prevent evaporation of the SAM solution.

2.5 Deposition of Pt NPs on Functionalised Copper Substrates

Prior to use the Pt NP solution was placed under the flow of N_2. The Cu substrates were removed from the SAM solution and placed in methanol for 10 mins. They were then removed, washed with IPA, dried with N_2 and placed into the NP solution, while under the flow of N_2 for 15 mins, after which time they were removed, dried with N_2 and immediately annealed in the tube furnace.

2.6 Annealing of Substrates

The samples were annealed using a stainless steel reaction cell in a tube furnace. Different reaction environments were evaluated by annealing the substrates under air or under reducing atmosphere (H_2 /Ar). The role of the annealing temperature was also evaluated.

In a typical annealing experiment, the reaction cell was placed in the tube furnace and annealed at 350°C for a period of 30 mins. After which time the tube furnace was turned off and the reaction cell allowed to cool to room temperature before disassembling and removing the samples. Three annealing conditions were evaluated, firstly the substrates were annealed under air. The second of these conditions involved annealing the samples under a reducing environment, in this case forming gas (H_2/Ar). The furnace was set to 350°C and the samples were annealed at this temperature for 30 mins after which time the furnace and the gas was turned off and the reaction cell was allowed to cool to room temperature. The third set of conditions involved annealing the sample under forming gas for a period of 10 mins initially at 120°C, after which time the temperature was increased to 350°C and the samples remained at this temperature for 30 mins. After this time, the furnace was turned off but the samples remained under a flow of H_2/Ar for the duration of the cooling.

The influence of the annealing temperature was also evaluated. The annealing experiments were performed under a reducing environment for both the annealing and cooling stages. The three different temperatures used were 450°C, 550°C and 650°C. These temperature experiments were also performed on all three Cu substrates similar to the environmental experiments. These temperatures were used to determine if the Pt NP would melt and potentially form a film due to melting point depression of the Pt in the nanoparticle scale. As the PVD wafer has the thinnest coating of copper at these higher annealing temperatures it was possible for the copper to de-wet which had the ability to affect the Pt coverage.

2.7 Materials Characterisation

The nanoparticles were analysed using Transmission Electron Microscopy (TEM) and each of the samples were analysed with Scanning Electron Microscopy (SEM) analysis while others were further analysed using X-Ray Diffraction (XRD) and X-ray Photoelectron Spectroscopy (XPS). The samples were stored in an inert environment, which was a N_2 glove box due to the instability of the samples in an oxygen rich environment. For comparative purposes a set of samples including each type of substrate was analysed unannealed after deposition to highlight any changes that occurred during the annealing process including those discernible by the naked eye. **Figure 2.1** below shows the schematic of the reaction procedure that demonstrates what happens to the substrates after each step of the reaction that produces cubic NP.

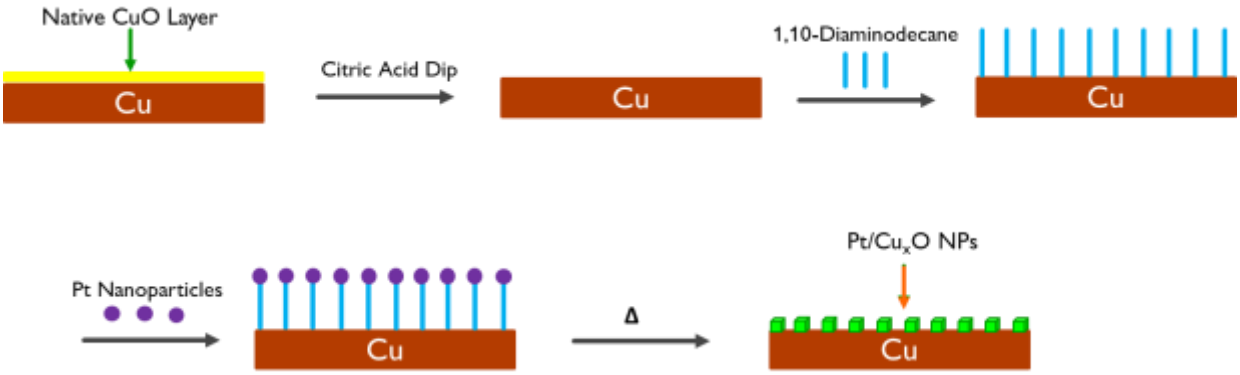

Figure 2.1: Schematic of reaction process.

2.7.1 TEM Analysis

TEM analysis functions by passing an electron beam through a sample to produce a 2D image of that sample. The samples must have a thickness <150 nm in order to allow the

electrons to pass through them and reach the fluorescent screen or detector below. A schematic of the layout of a TEM can be seen from **Figure 2.2**.

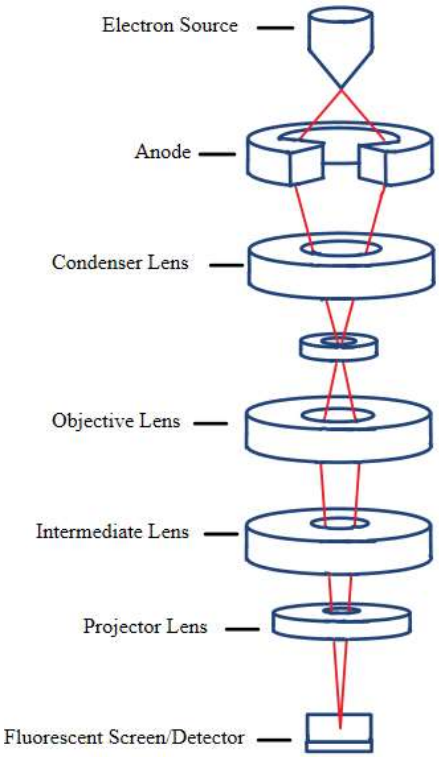

Figure 2.2: Schematic of a TEM instrument. *Adapted from Reference 2.*

The broad electron beam used in this type of microscope provides information on the samples internal structure, morphology as well as its composition.[3] These advantages, along with the simple preparation made TEM a very useful tool for analysing these NP before they were adhered to the surface of the substrate.

In this work, TEM was performed on a JEOL 2100 LaB6 instrument at an operating voltage of 300 kV. As these particles were in solution some preparation was needed in order to analyse them under the microscope. Using a dropper, a small amount of the Pt NP solution was drop cast onto a carbon film, TEM grid and allowed to dry.

2.7.2 SEM Analysis:

SEM functions in a similar way to TEM in that an electron beam is passed through a serious of lenses until it reaches the sample. However, contrary to TEM analysis this focused electron beam does not pass through the sample, instead it scans the sample causing electron-sample interaction that produces a range of signals. These signals are composed of backscattered electrons, X-rays and secondary electrons which are detected and produce a 3D image of the samples surface.[4] This can be seen in **Figure 2.3.** For this work SEM analysis was carried out using the Zeiss Supra 40 instrument.

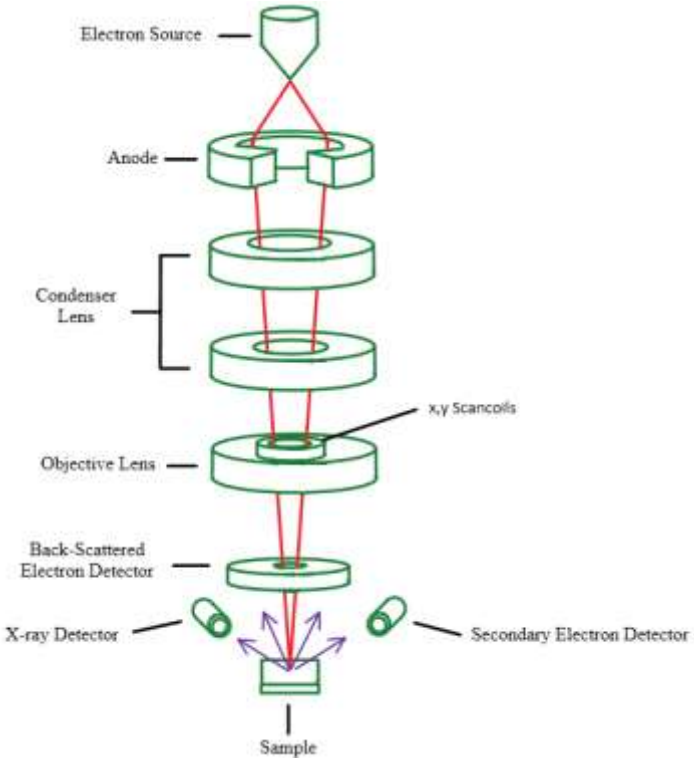

Figure 2.3: Schematic of a SEM instrument. *Adapted from Reference 2.*

The information obtained from this analysis demonstrates the surface topography. Energy Dispersive X-ray (EDX) analysis can be done in conjunction with SEM analysis and this provides information on the chemical composition of the sample through elemental analysis.

2.7.3 XRD Analysis:

Similar to the electron microscopy analysis, XRD is also a non-destructive technique. XRD allows for the analysis of crystalline structures. X-rays are generated by a cathode ray tube, which are then filtered to produce monochromatic radiation, directed toward the sample. The interaction of the incident X-rays with the sample produces constructive interference when conditions satisfy Bragg's Law, which is $n\lambda = 2d_{hkl}sin\theta$. This equation represents the crystalline structures of the atom planes (hkl), the distance between these planes (d), the incidence angle (θ) as well as the wavelength of the X-ray (λ). These rays are reflected from the surface, detected and produce peaks which demonstrate the different hkl peaks that the incidence ray came into contact with as well as how crystalline the material is. Bragg's Law can be seen in **Figure 2.4.**

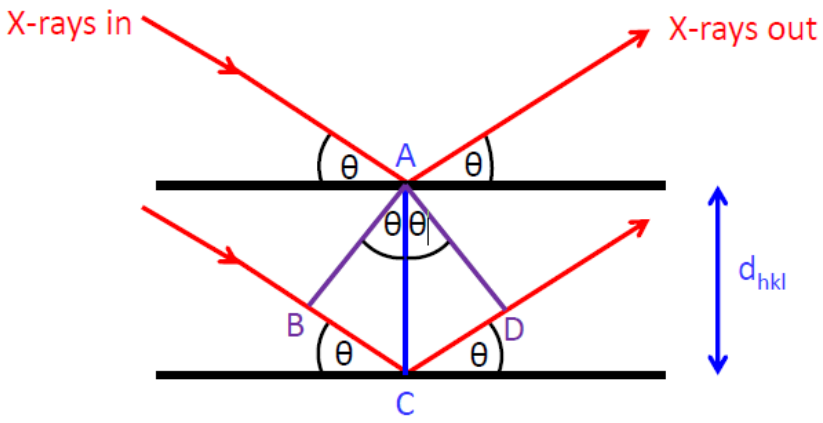

Figure 2.4: Diagram demonstrating Bragg's Law.

For this work XRD analysis was conducted on a PHILLIPS Xpert PW3719 diffractometer using Cu Kα radiation.

2.7.4 XPS Analysis:

XPS is also a non-destructive technique that can measure the elemental composition, chemical and electronic state of the surface of a material. This analysis produces spectra as a result of irradiating the solid surface of the substrate with a beam of X-rays while simultaneously recording the kinetic energy produced by the emitted electrons from the surface. The electron beams penetrates the surface of the analysed material by a depth of 1-10 nm emitting the surface electrons as photoelectrons. A schematic of the XPS can be seen in **Figure 2.5** below.

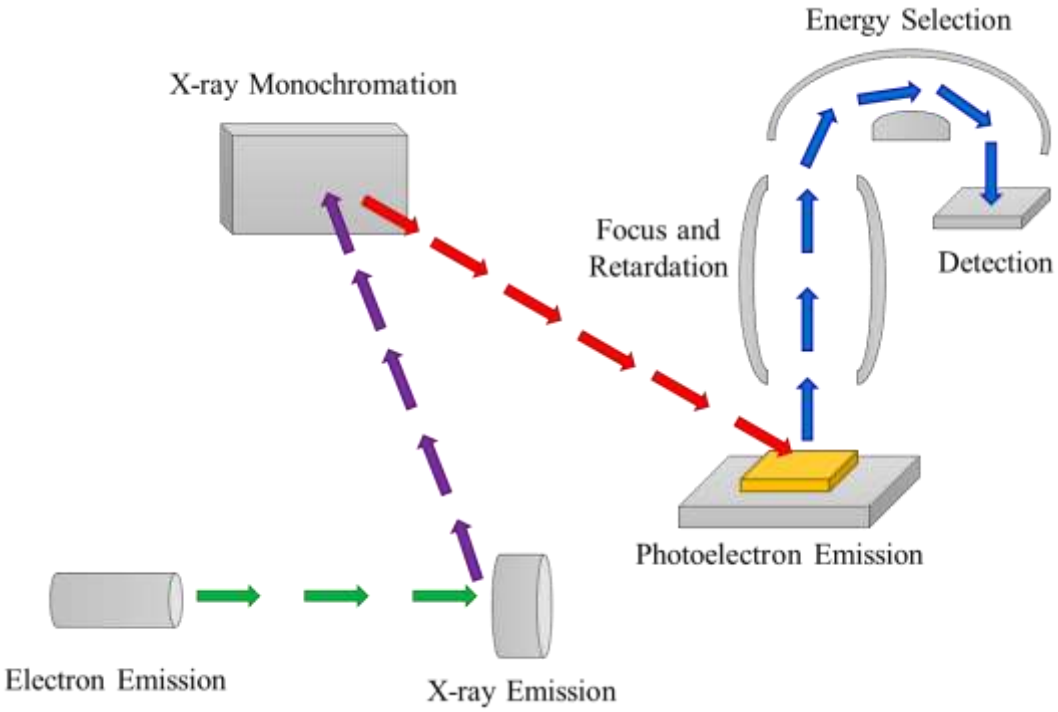

Figure 2.5: Schematic of XPS instrument. *Adapted from Reference* 5.

XPS analysis can also provide information about the binding energy of both a material's surface and interfaces. The binding energy of a material is unique to each element and when the core electrons from these elements are emitted they can be detected and the elements present of the surface of the material can be identified. These core electrons are only emitted as a result of the atoms absorbing the energy from the X-ray and the energy required to cause

these core electrons to be emitted is unique to each element.[6] This analysis technique is highly suitable to these substrates as it provides detailed information of the elemental composition of the surface allowing the changes in both the NPs and the substrates before and after annealing to be identified. For this work XPS analysis was carried out using an Oxford Applied Research Escabase XPS System.

2.8. References:

(1) Bigall, N. C.; Härtling, T.; Klose, M.; Simon, P.; Eng, L. M.; Eychmüller, A. Monodisperse Platinum Nanospheres with Adjustable Diameters from 10 to 100 Nm: Synthesis and Distinct Optical Properties. *Nano Lett.* **2008**, *8* (12), 4588–4592.

(2) ThermoFisher Scientific. Transmission Electron Microscopy vs Scanning Electron Microscopy. Electron microscopy reference focusing on the difference between transmission electron microscopy (TEM) and scanning electron microscopy (SEM). https://www.thermofisher.com/ie/en/home/materials-science/learning-center/applications/sem-tem-difference.html (Accessed Apr 6, 2021).

(3) Gleichmann, N. SEM vs TEM https://www.technologynetworks.com/analysis/articles/sem-vs-tem-331262 (Accessed Apr 6, 2021).

(4) Nanoscience Instruments. Scanning Electron Microscopy https://www.nanoscience.com/techniques/scanning-electron-microscopy/ (Accessed Apr 15, 2021).

(5) Thermo Scientific XPS. What is X-Ray Photoelectron Spectroscopy (XPS)? https://xpssimplified.com/whatisxps.php (accessed Apr 21, 2021).

(6) Mathias, J. How to Analyze XPS Data: A Beginner's Guide https://www.innovatechlabs.com/newsroom/2075/how-analyze-xps-data/ (Accessed Apr 26, 2021).

Chapter Three:

Results and Discussion

3.1 Introduction

This chapter reports the solid-state synthesis and characterisation of Pt@Cu_2O core-shell nanocubes immobilised onto a Cu substrate and their application as a glucose sensor. Though most of the experiments were carried out on a chemically mechanically polished (CMP) Cu wafer, two other substrates were also used during the optimisation process. The details of these substrates are listed in **Table 3.1**.

Table 3.1: Details of Cu substrates used for the synthesis of Pt@Cu_2O core-shell nanocubes.

Cu Wafer	***Grain Size***	***Cu Coating Thickness***	***CMP***	***Surface Roughness (Rq)***
Cu1*	Large	~100 nm	Y	0.8 nm
Cu2†	Small	~ 30 nm	N	1.0 nm
Cu3*	Large	~100 nm	N	5.0 nm

**Electrochemical deposition of Cu; †Physical vapour deposition of Cu*

The stepwise sequence in the synthesis of the nanostructures is illustrated in **Figure 3.1.** The first step involves the removal of the Cu native oxide followed by surface functionalisation with a self-assembled monolayer (SAM) of 1,10-diaminodecane (DAD). The purpose of this is two-fold: **1)** to prevent re-oxidation of the Cu surface and **2)** to introduce a functional group to anchor the Pt nanoparticles (PtNP). The modified Cu substrates are then immersed into a solution of synthesized PtNP resulting in their immobilisation. Finally, the substrates are annealed under forming gas and cooled in air yielding nanostructures with a cubic morphology. Optimisation of this process was carried out to maximise the coverage of Pt@Cu_xO on the Cu substrate. This included studying the impact of the presence of the DAD SAM and varying the annealing temperature and atmosphere. Material characterisation of the resulting nanocubes was carried out using scanning electron microscopy (SEM), transmission

electron microscopy (TEM), cross-sectional TEM (XTEM), X-ray diffraction (XRD) and X-ray photoelectron spectroscopy (XPS). Finally, these substrates were evaluated for the electrochemical detection of glucose for potential application in glucose sensing.

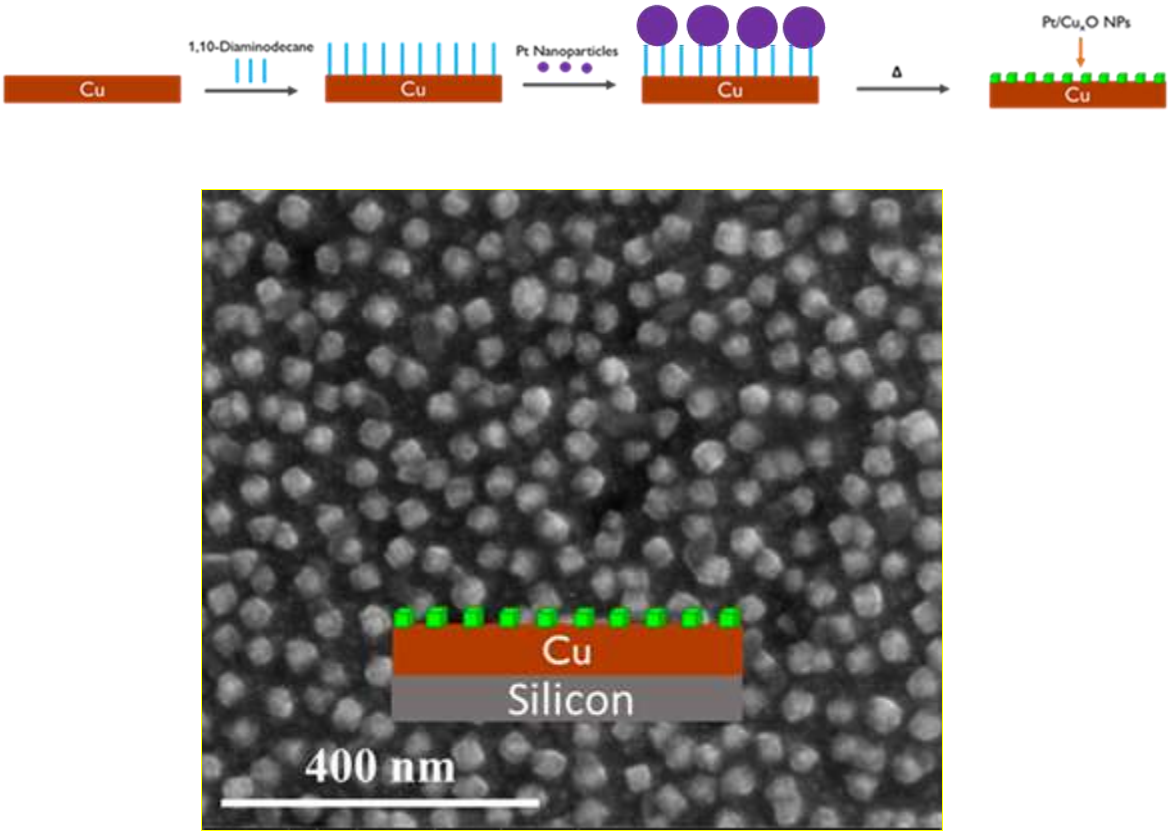

Figure 3.1: Schematic illustrating the solid-state synthesis of Pt@Cu_2O nanocubes on Cu substrate.

3.2 Process for the Optimisation of the Synthesis of Pt@Cu_2O core-shell nanocubes

3.2.1 Synthesis of Pt Nanoparticles

A range of PtNP, with targeted mean diameters of 10, 30 and 50 nm, were grown via an aqueous phase, seed mediated method. Citrate stabilised Pt seed particles with a mean diameter of 5 nm were first synthesised. Subsequent growth of the seed particles results in the formation of PtNP with a dendritic structure with advantages such as large surface area, and excellent connectivity between the different parts of the structure. It has been reported

that nanoparticles form through the attachment of the smaller Pt crystallites promoted by the low stabilizing ability of the citrate species.[1–3]Another driving force for the formation of the dendritic structures is the reduction of surface energy due to a net reduction is surface area.

TEM analysis of the as-synthesized PtNP solution identified that the size distribution of all samples was broad. The polydisperse nature of the sample is attributed to the synthesis conditions. In the initial stage of synthesis, the degree of supersaturation of Pt atoms is high due to the fast reduction of the Pt salt precursor by sodium borohydride. The number of possible nucleation sites provided by the Pt seeds may not be sufficient to accommodate all the Pt atoms generated from the reduction and as a result, the supersaturation would be kept at a high level, facilitating homogeneous nucleation in the solution. Sequential centrifugation was used to separate the multiple fractions in the PtNP to obtain a solution with a narrower size distribution.

The solution was initially centrifuged at 3500 rpm for 25 min to remove the largest particles and agglomerates. The precipitate was discarded and the supernatant was centrifuged further at 4500 rpm for 25 min to remove medium sized aggregates. The precipitate was again discarded, and the supernatant was collected. To remove excess citrate, reducing agent and precursor species the supernatant was then centrifuged at 8500 rpm for 85 min. This time the supernatant was discarded and the precipitate was collected and redispersed in water.

The TEM and associated size distribution analysis of the synthesised nanoparticles are shown in **Figure 3.2** and **Table 3.2. Figure 3.2 a)** shows an image and size analysis for the smallest nanoparticles which have a measured average size of 13 nm and a standard deviation 1.87 nm. These nanoparticles were prepared using 10 uL of a (0.4 M) Pt precursor solution. Larger nanoparticles with a mean diameter of 28 nm and a standard deviation of 4.44 nm, as shown in **Figure 3.2 b)** was also prepared using the same 5 nm seed solution but

using a higher Pt precursor concentration (45 uL of a 0.4 M). The particles maintained good size and shape uniformity as seen in the TEM and size distribution histogram in **Figure 3.2 b)**. In an effort to make larger PtNP, the 28 nm nanoparticles were used as seed particles. The subsequent growth led to an increase in the diameter of the nanoparticles, resulting in a mean diameter of 44 nm. However, the nanoparticles had a board size distribution (standard deviation 16.5 nm) as displayed in the TEM and size distribution histogram in **Figure 3.2 c)**. The formation of smaller nanoparticles was attributed to homogenous nucleation and could potentially be improved through reaction optimisation, however this was not pursued in the current study. For this work the nanoparticles with a mean diameter of 30 nm were used for the immobilisation onto the Cu substrates which can be seen in **Figure 3.3.**

Table 3.2: Targeted and measured particle size for synthesised PtNP.

Targeted particle size	***Measured particle size***	***Standard deviation***
10 nm	13 nm	1.87 nm
30 nm	28 nm	4.44 nm
50 nm	44 nm	16.5 nm

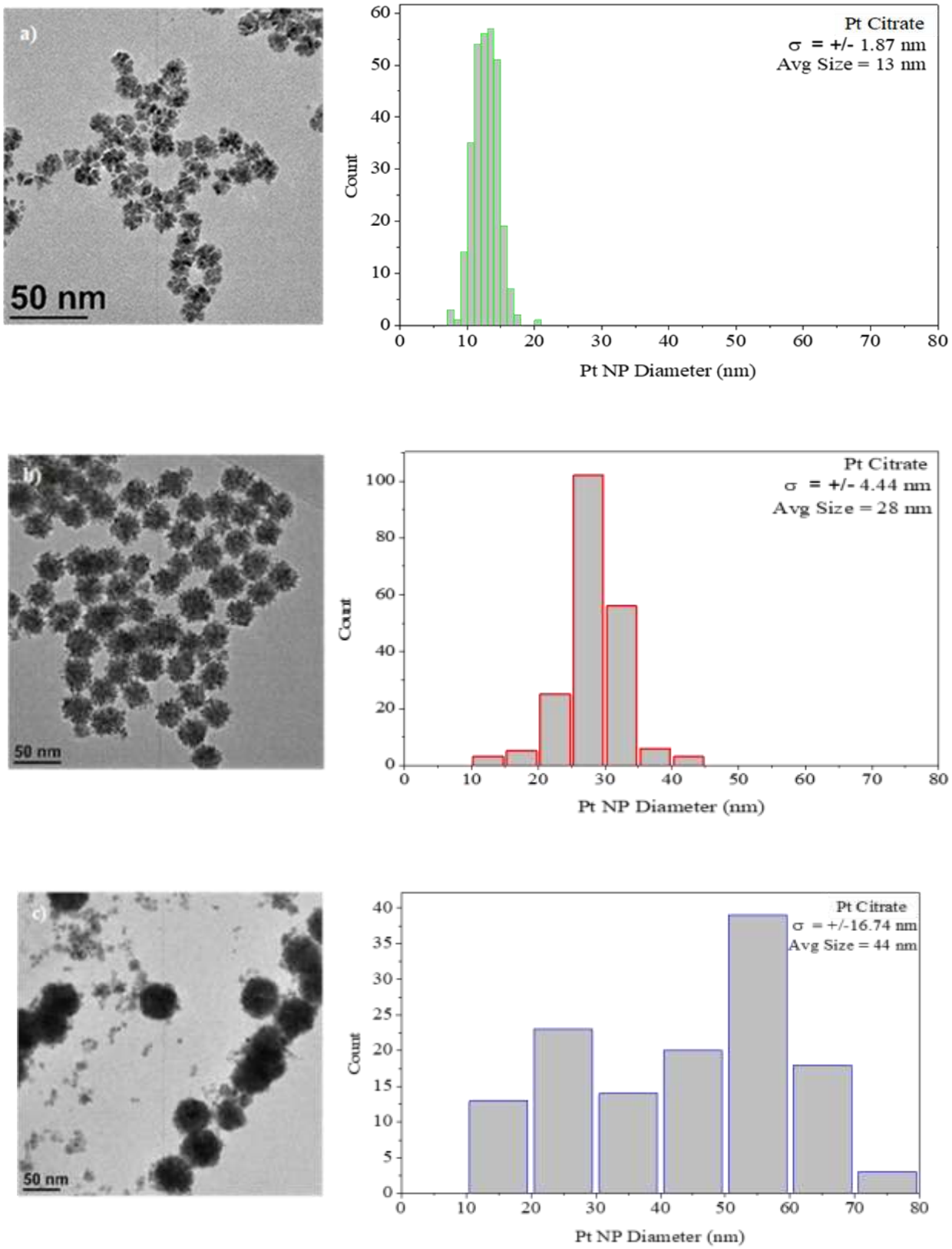

Figure 3.2: TEM image and size distribution of a) 10 nm NP, b) 30 nm NP and c) 50 nm NP.

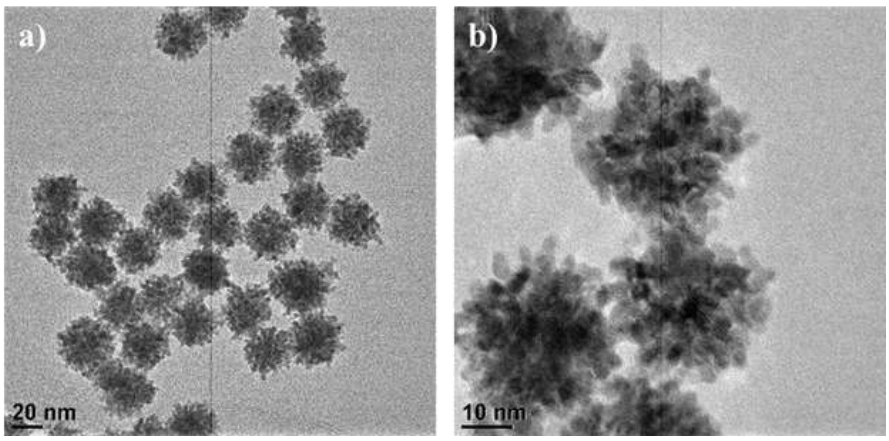

Figure 3.3: TEM images of **a)** 30 nm PtNP and **b)** detailed image of 30 nm PtNP.

It is common to sonicate citrate stabilised nanoparticles prior to use as they tend to agglomerate as they age. However, it was observed by TEM analysis (**Figure 3.4**) that sonication of these dendritic nanoparticles leads to their fragmentation. **Figure 3.4 a)** and **b)** shows a TEM image typical of 30 nm nanoparticles before and after sonication respectively. After sonication TEM analysis identified a high degree of fragmented dendrites. Consequently, the nanoparticles for this study were not sonicated prior to use and were used within 3 weeks of their synthesis.

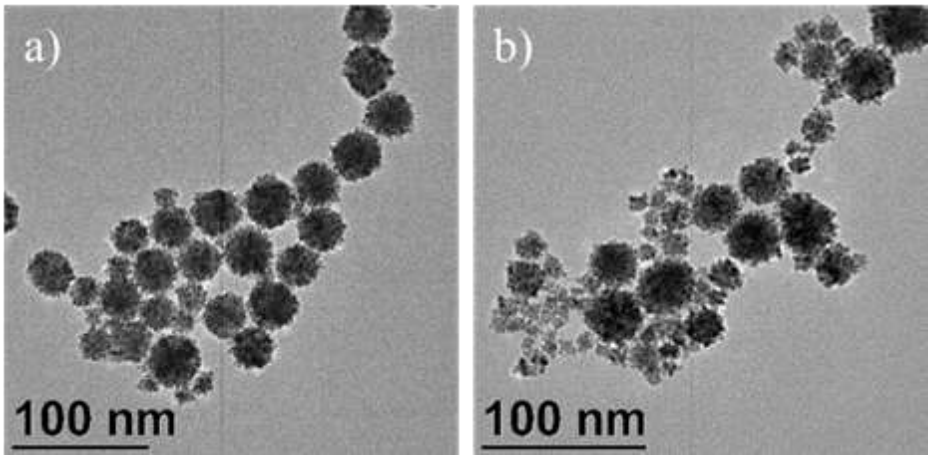

Figure 3.4: TEM images of the PtNP **a)** before sonication and **b)** after sonication.

3.2.2 Nanoparticle Immobilisation and Optimisation

After surface oxide removal the Cu surface is functionalized with DAD as shown in the schematic in **Figure 3.1**. The citrate stabilized PtNP are then immobilized onto the DAD-functionalized surface through the interaction of the terminal amino groups with the surface of the PtNP. **Figure 3.5 (a – c)** displays SEM images of Cu substrates after the immobilization of PtNP that were subject to different centrifugation steps. **Figure 3.5 (d – f)** show those substrates after annealing at a temperature of 350ºC. **Figure 3.5 a)** shows the deposition of the as-synthesized PtNP, ***i.e.*** where no size selective centrifugation was conducted. A high coverage density of PtNPs is achieved on the Cu substrates; however the lack of the uniform size is clearly evident in the SEM image. **Figure 3.5 d)** shows a SEM of this substrate after annealing at 350°Cwhere the formation of larger facetted particles can be identified. As the nanoparticles were not subject to purification after synthesis, residual species such as sodium, borohydride, excess citrate and precursor material also contaminate the substrate. **Figure 3.5 b)** and **c)** show the PtNP deposition using centrifuge purification to obtain a narrow side distribution. **Figure 3.5 e)** and **f)** display the substrates after annealing at 350°C which show only minor nanoparticle agglomeration and well-facetted structures. Sequential centrifuge also diluted the PtNP concentration as nanoparticles were removed through each centrifuge sequence, thereby lowering the nanoparticle coverage obtained on the Cu substrates.

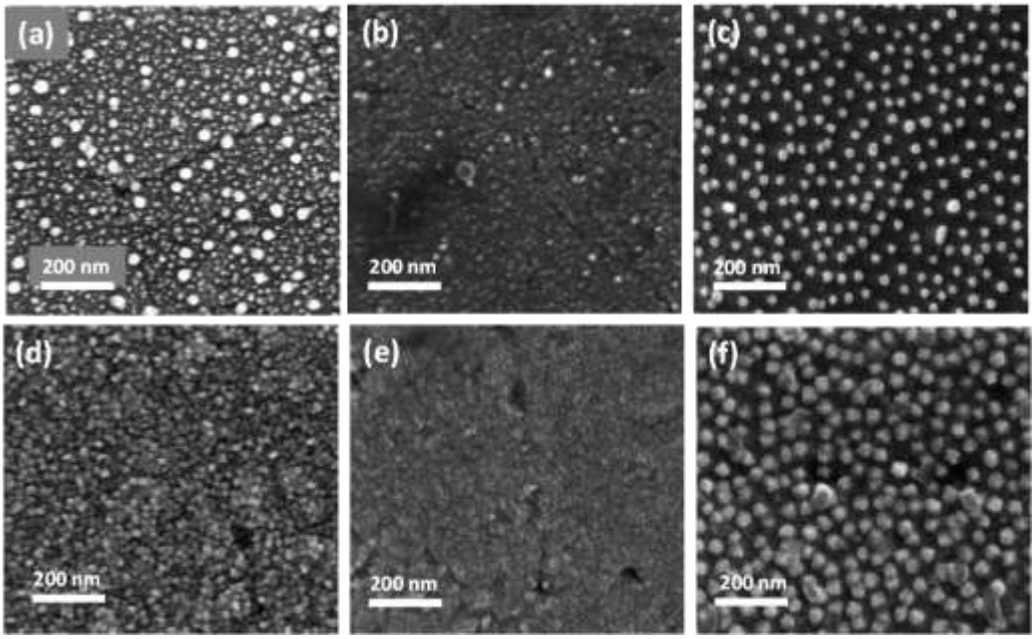

Figure 3.5: a) Unannealed, unwashed PtNPs **b)** unannealed polydisperse PtNPs of non-uniform particles, **c)** unannealed monodisperse PtNPs with more uniform particles, **d)** annealed , unwashed PtNPs **e)** annealed polydisperse PtNPs of non-uniform particles and **f)** annealed monodisperse PtNPs with more uniform particles.

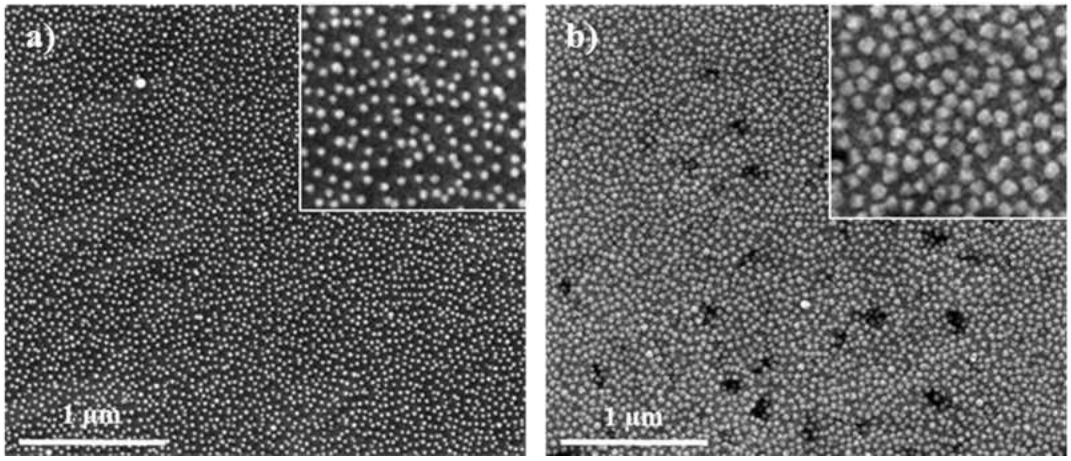

Figure 3.6: SEM images of optimal PtNP coverage **a)** unannealed and **b)** annealed monodisperse PtNPs with more uniform particles.

To obtain the optimal coverage of PtNP a high concentration of PtNP with a narrow size distribution is required. **Figure 3.6** shows the optimized PtNP immobilization on the Cu substrates. **Figure 3.6 a)** shows a high density of 30 nm PtNP uniformly dispersed on the Cu substrate. **Figure 3.6 b)** shows the substrate after annealing under a reducing atmosphere (H_2/Ar) at 350°C and cooling to RT in air. The formation of cubic nanostructures across the substrate is clearly illustrated. The resultant cubic nanostructures display high degree of size and morphology control and remain well-dispersed across the substrate.

Temperature dependent experiments confirmed that the cubic nanostructures formed when the substrates were annealed at 300°C and 350°C but that the PtNP remained relatively spherical when heated to only 275°C. The heating and cooling profiles of the furnace during the annealing process was measured. The heating rate for annealing the substrates under forming gas at 350°C for 30 min was found to be 32°C/min and can be seen in **Figure 3.7 a).** The reactor cell was left in the furnace for 40 min to cool before being removed from the furnace into the fumehood and allowed to cool for another 50 min at which time the cell was disassembled and the samples removed. **Figure 3.7 b)** shows the temperature gradient after the furnace is turned off.

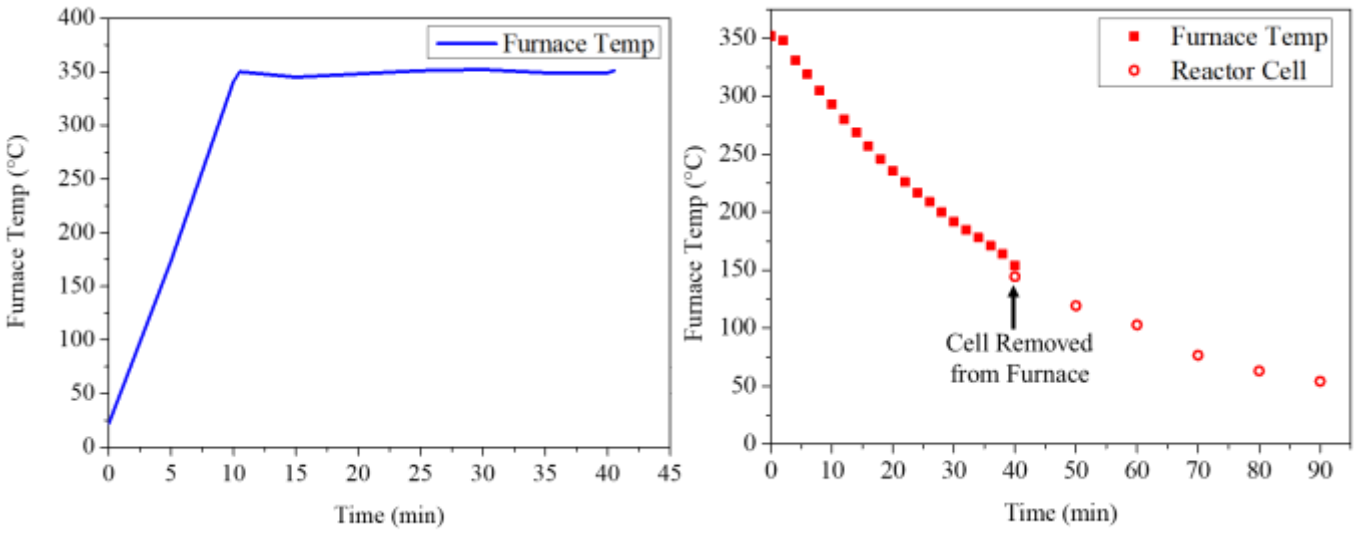

Figure 3.7: Temperature gradient during **a)** annealing and **b)** cooling after annealing.

3.3 Characterisation of Pt@Cu_2O core-shell nanocubes

3.3.1 XPS Analysis

XPS analysis was carried out to evaluate changes in the substrate surface chemistry at each synthesis step. **Figure 3.8** compares the survey spectra of Cu substrates after surface functionalisation with the DAD SAM, followed by PtNP deposition and subsequent thermal annealing under H_2/Ar at 350°C. In addition to the characteristic Cu peaks (Cu 2p, Cu 3s, Cu 3p), the survey spectra of substrates functionalised with DAD show the presence of the C 1s and N 1s peaks attributed to the organic over-layer. After PtNP deposition, the survey spectrum shows the presence of the Pt 4f and Pt 3d peaks confirming successful immobilisation of the PtNPs. Annealing the substrates results in a significant decrease in the C 1s signal and the disappearance of the N 1s peaks due to the loss of the DAD SAM on thermal annealing. The Pt 4d peak also disappears due to attenuation of the Pt 4d electron after becoming encapsulated in the oxide shell.

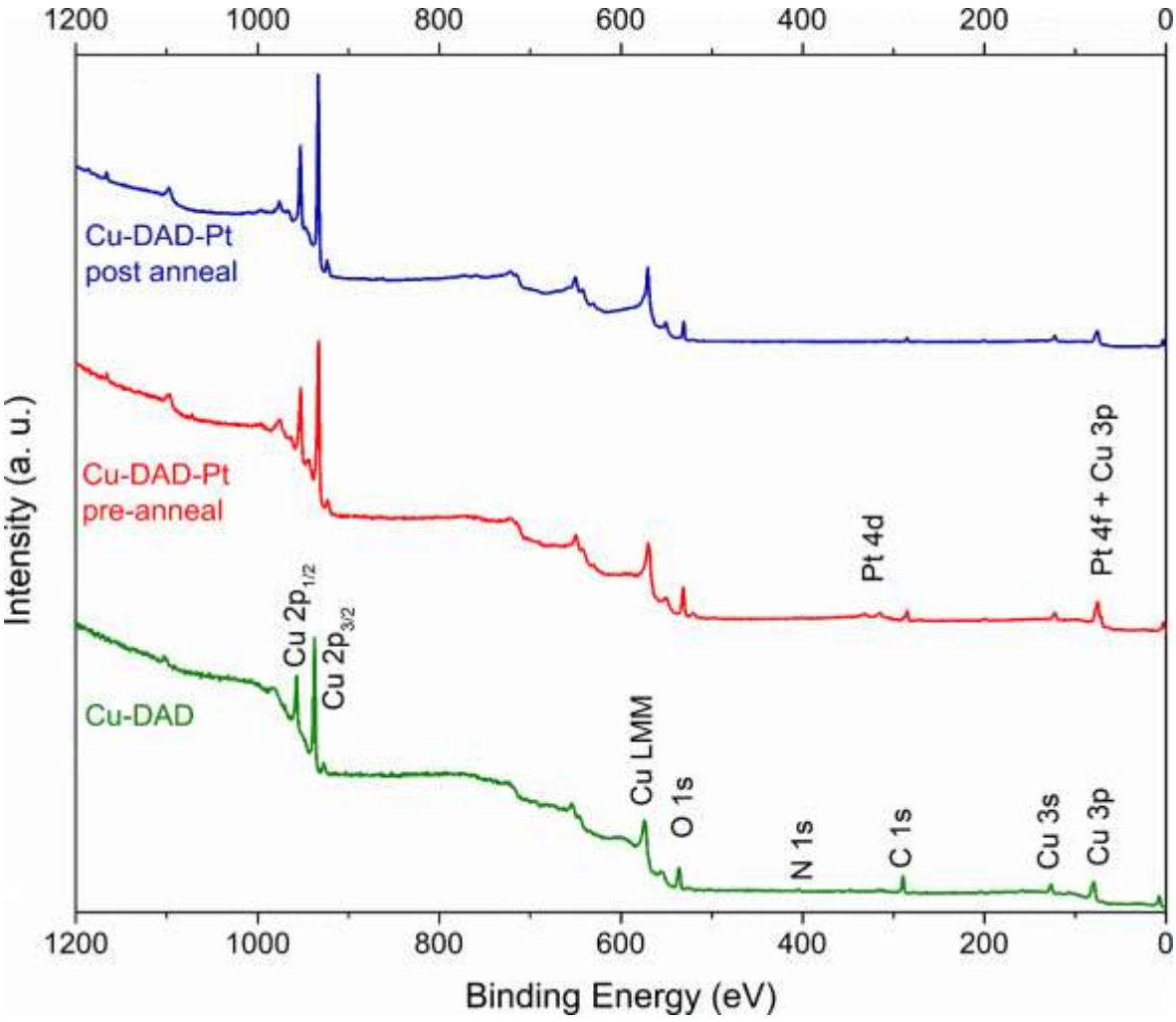

Figure 3.8: Comparison of XPS survey spectra of Cu substrates functionalised with DAD (green), after PtNP deposition (red) and after annealing at 350°C (blue).

High resolution core level XPS spectra was recorded to further identify and evaluate changes in chemical environment before and after annealing. **Figure 3.9 a)** compares the Cu 2p core level of the unannealed and annealed substrates. In the unannealed sample the dominant Cu $2p_{3/2}$ peak is located at a B.E. of 932.9 eV in good agreement with metallic Cu(0) and Cu^{1+} species assigned to Cu_2O and/or metallic Cu, respectively. A very small shoulder peak is observed at 934.9 eV in the unannealed sample and is attributed to Cu^{2+} species, assigned to CuO. The weak feature at a B.E. of 944 eV corresponds to the shakeup satellite

peaks associated with CuO. XPS analysis shows that the PtNP decorated substrates remain relatively oxide free with only trace amounts of surface oxide.

The Cu 2p core level of after annealing shifts upward to 933.45 eV due to oxidation but this B.E. is lower than that typically reported for Cu_2O, likely due to the underlying Cu substrate, or due to the presence of non-stoichiometric oxides or even Pt-Cu alloy formation. Metallic Cu cannot be easily distinguished from Cu^{1+} using the 2p core level due to their spectral overlap so to discriminate Cu_2O from Cu, the corresponding Cu LMM Auger peak was evaluated, which is shown in **Figure 3.9 b).** The broad Cu LMM Auger peak for the unannealed sample clearly exhibits a prominent metallic Cu feature at a kinetic energy (K.E.) of 918.1 eV and a peak at 916 eV associated with Cu_2O.[4] Therefore, the Cu $2p_{3/2}$ peak at 932.9 eV can be assigned to both metallic Cu from the underlying substrate and surface oxide. The annealed sample shows a clear decrease in the metallic contribution which shifts the peak to lower K.E., again consistent with the formation of the oxide core shell nanocubes. XPS indicates that Cu_2O is the major composition of the oxide shell.

The O 1s core level XPS spectra (**Figure 3.9 c)** of the unannealed substrates displays a broad peak (fwhm = 2.4) at a B. E. of 531.3 eV attributed to the presence of mixed oxide phases (Cu_2O and CuO) and to chemisorbed and dissociated oxygen species which are typically observed at B.E. >531.3 eV.[5] After annealing, the O 1s peak narrows considerably (fwhm = 1.3) and is downshifted with the peak centred at 530.8 eV, which is in excellent agreement with the formation of Cu_2O after annealing.[6] A minor shoulder peak is also observed at 532.2 eV is associated with surface absorbed O or oxygen vacancies.[7]

Figure 3.9 d) compares the Pt 4f spectrum for the substrates. The unannealed sample display a doublet at a binding energy of 71.1 eV consistent with metallic Pt(0), PtO, PtO_2 and $Pt(OH)_2$ species are typically observed at 74, 74.9 and 72.7 eV, respectively, however due

to spectral overlap of the Cu $3p_{3/2}$ peak with the Pt 4f peak, deconvolution was not possible to evaluate the oxidation states of the PtNPs, however it would be expected that they primarily metallic Pt with minor surface oxide present. The Pt $4d_{5/2}$ peak, shown in **Figure 3.10 a)** is located at a B.E. of 314.7 eV in good agreement with metallic Pt(0) species.[8] XPS analysis is often used to evaluate the formation of alloy nanoparticles as a core-level shift occurs upon alloying due to the change of electron density in d-band states. The binding energy shifts can potentially reflect the degree of alloying between Cu and Pt.[9] The Cu $2p_{3/2}$ peak of CuPt alloys undergo red-shifts typically ~0.5 eV, compared to monometallic Cu which are associated with the suppressed p–d hybridization due to interaction of Cu 2p electrons with wide d-band electrons in Pt.[10] The shifts observed in the Pt $4f_{7/2}$ peak are very small (~0.02 eV, which is below the detection limit of the instrument) because Cu does not affect the electron density in Pt 5d states.[11] However, as shown in **Figure 3.9 d)** and **Figure 3.10 a),** after annealing the Pt 4f double and the Pt 4d doublets both disappear due do attenuation of the Pt signal after encapsulation with Cu_2O.

The C 1s core level of the substrates before annealing display three environments attributed the carbon chain of the DAD and adventitious hydrocarbons at 284.8 eV (C-C), carbon single bound to oxygen or nitrogen at 285.8 eV (C-O and/or C-N) and a more electron deficient C environment that correspond to C-O-N or C=O at 288.1 eV.[12] After annealing the C 1s core level is best fit to two peaks C-C associated with adventitious hydrocarbons and a minor should peak centred at 288.6 eV as the DAD SAM has been removed during the anneal.

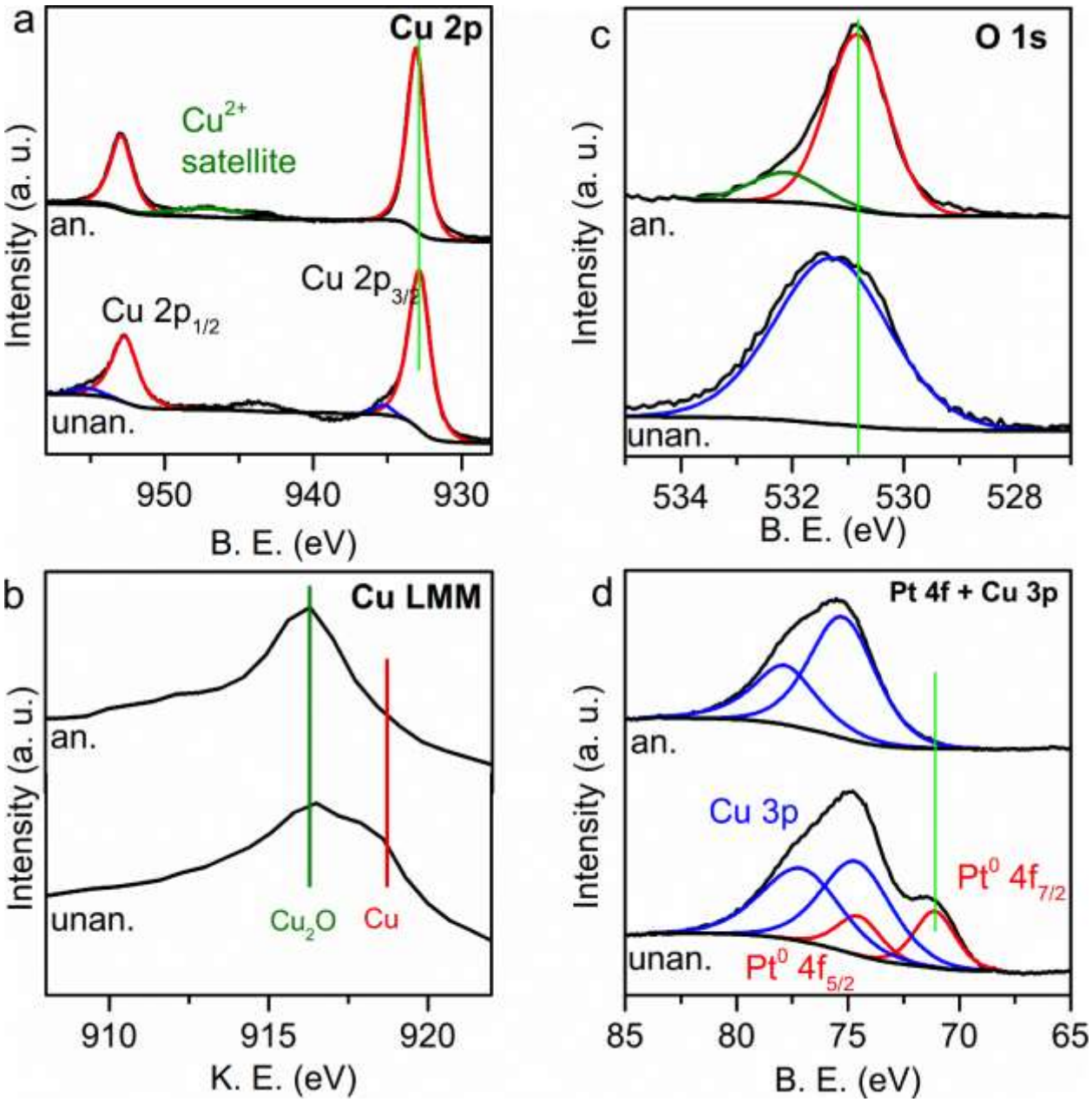

Figure 3.9: XPS analysis showing **a)** Cu 2p core level **b)** Cu LMM Auger spectra **c)** O 1s core level and **d)** Pt 4f core level of the substrates before (unan.) and after annealing (an.) at 350°C.

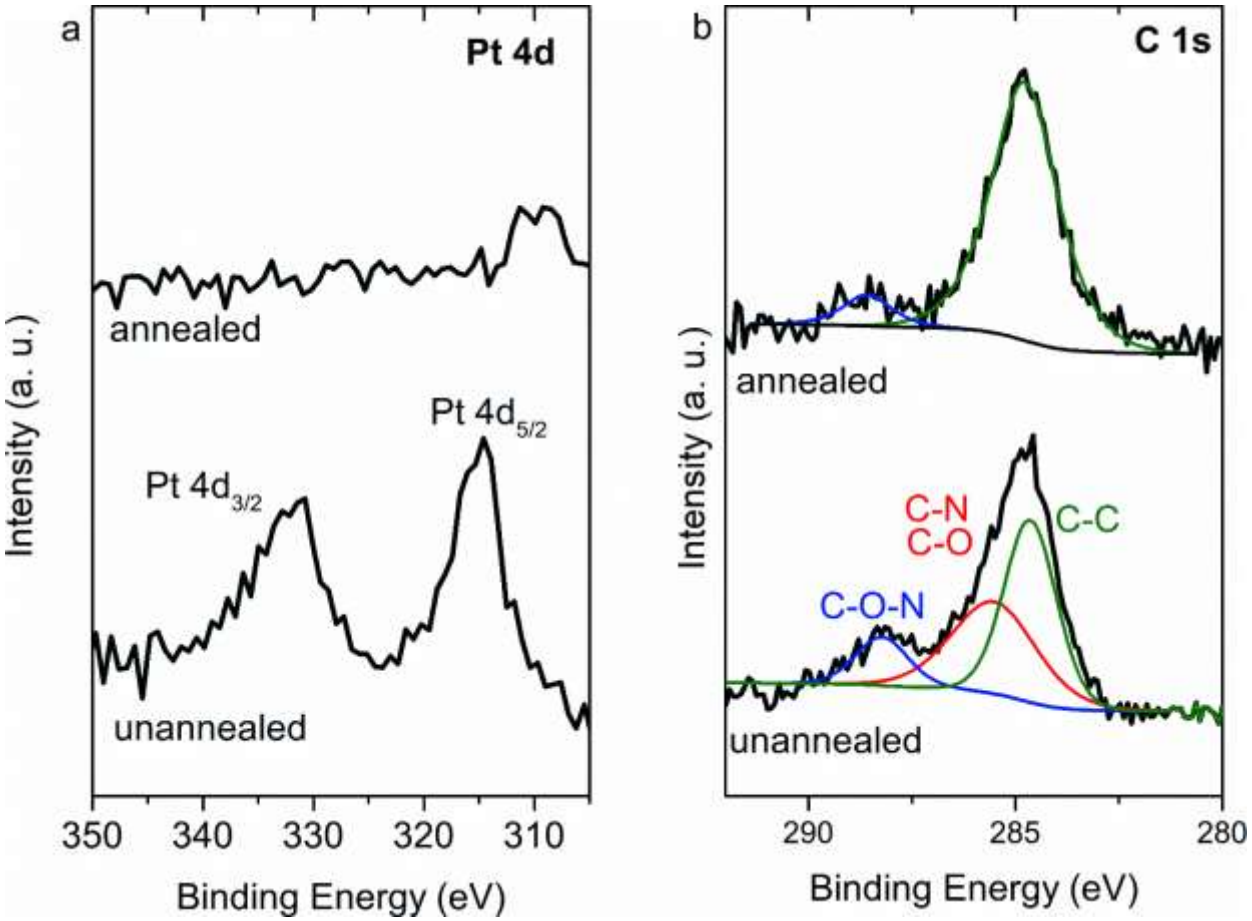

Figure 3.10: **a)** Pt 4d and **b)** C 1s XPS core level spectra before and after substrate annealing at 350°C.

Evaluation of the N 1s core level was carried out to further understand the immobilization of the PtNPs onto the DAD – functionalized Cu substrates. It is worth noting that N environments can be challenging to analyse by XPS due to the element having a low photoionization cross section and stability under analysis conditions, as some N groups are prone to X-ray induced degradation under long scan times.[13]

Furthermore, multiple N bonding configurations can have the same binding energy or the chemical shifts for N containing functionalities, such as amine, imine or amide are very small. **Table 3.3** summaries the binding energy positons reported for common N containing organic functional groups.[11]

Table 3.3: N 1s binding energies for different N-containing organic functional groups. *Data Reference from 14.*

N Environment	Name	Binding Energy (eV)
N=C	Imine	397.8 - 399.0
N≡C	Nitrile	398
NH_2	Amine (aliphatic)	399.1-399.6
NHC=O	Amide	400.3-400.7
$-NH_2/NH_3^+$	Electron-donating /Protonated amine	400.9-401.7

Figure 3.11 shows the N 1s core level of the Cu substrate after functionalization with the DAD SAM, having a peak position located at a binding energy at 399.9 eV. This binding energy is characteristic of an aliphatic amine but N-coordinated to transition metals also contribute to the range between 399.5 and 400.5 eV.[10] After PtNP deposition, there is a sharp decrease in the N 1s signal which is attributed to the attenuation from the PtNPs. While a tentative observation, given the high signal to noise ratio in the Cu-DAD + Pt spectrum, the N 1s peak appears to be slightly shifted upward to a higher binding energy. This is consistent with protonation of the terminal amino groups after contact with the acidic citrate stabilized PtNP solution.

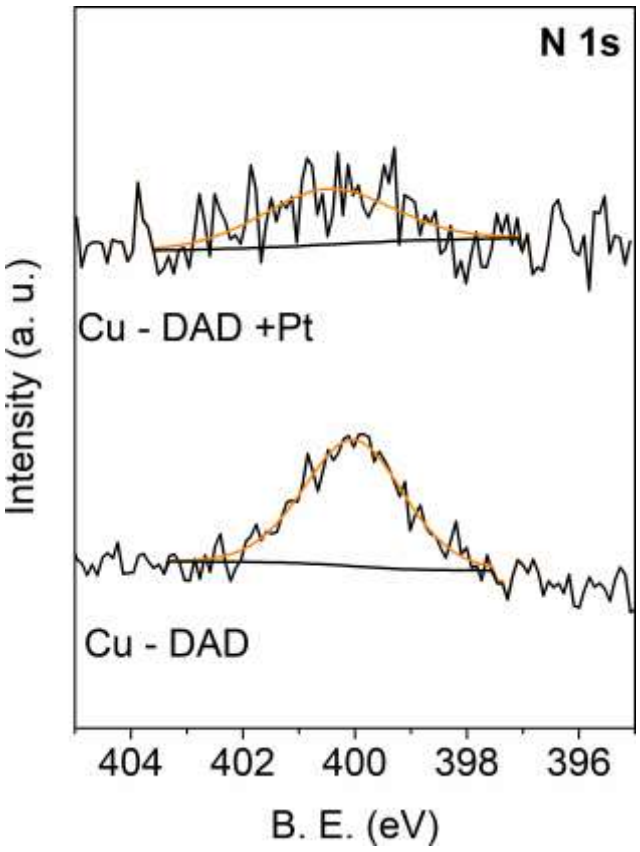

Figure 3.11: Comparison of the N 1s XPS core level of Cu substrates with the DAD-self assembled monolayer before and after PtNP deposition.

3.3.2 XRD Analysis

Figure 3.12 displays the XRD patterns of the Cu substrates before and after annealing at 350°C under H_2/Ar. The predominate XRD peaks are located at 43.4 2Θ indexed to the (111) planes of cubic Cu (JCPDF No. 04-0836). After annealing there is slight downward shift of this peak now centred at 43.3° *(see **Figure 3.12** inset)* due to the appearance of the overlapping Cu_2O (200) peak at 42.3°. The appearance of a second peak at 36.4° after annealing is in good agreement with the (111) plane of cubic phase Cu_2O. Diffraction peaks associated with Pt were not detected mostly likely due to the small crystallite size of the particles (5 nm) that make up the dendritic PtNPs.

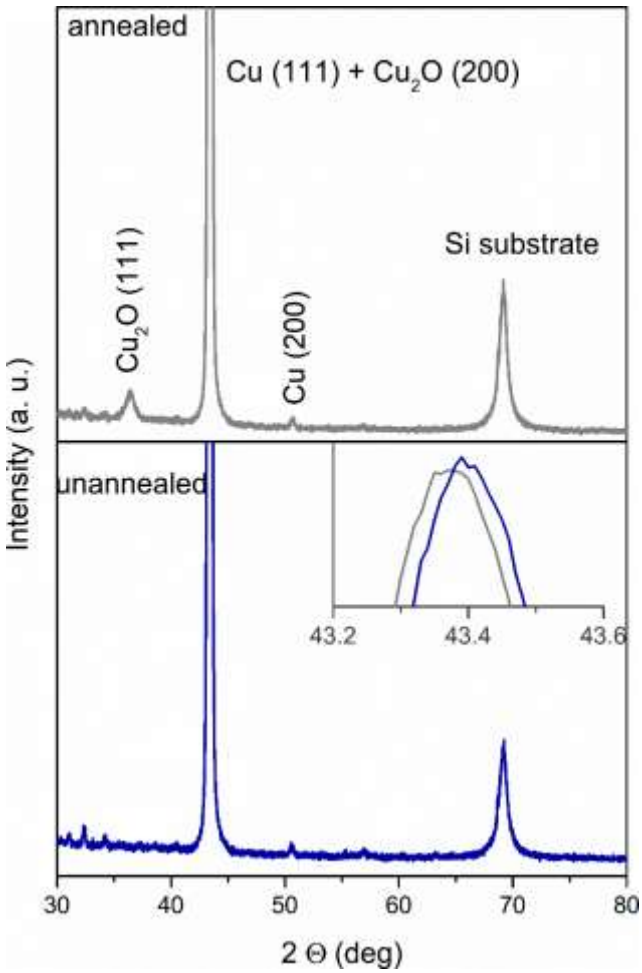

Figure 3.12: XRD analysis of PtNP decorated Cu substrates before and after annealing at 350°C.

3.3.3 XTEM Analysis

Cross-sectional TEM analysis was used to further study the immobilization and morphology of the core-shell nanostructures on the Cu substrates. High resolution TEM analysis was used to confirm the composition of the oxide shell as Cu_2O.

Figure 3.13 a) and **b)** show XTEM analysis of the Cu substrates. The presence of the core-shell nanostructures at the interface is clearly visible in **Figure 3.13 a)**. The cross section also shows the underlying Cu substrate, the adhesion layer (tantalum nitride) and the silicon wafer substrate. As indicated by SEM analysis the NPs are uniformly dispersed on the Cu

substrate surface. **Figure 3.13 b)** also shows the presence of Moiré fringes along the interface. Translational Moiré fringes are parallel contrast lines formed in high resolution TEM that arise from the interference of diffracting crystal lattice planes that are overlapping with one another.[15]

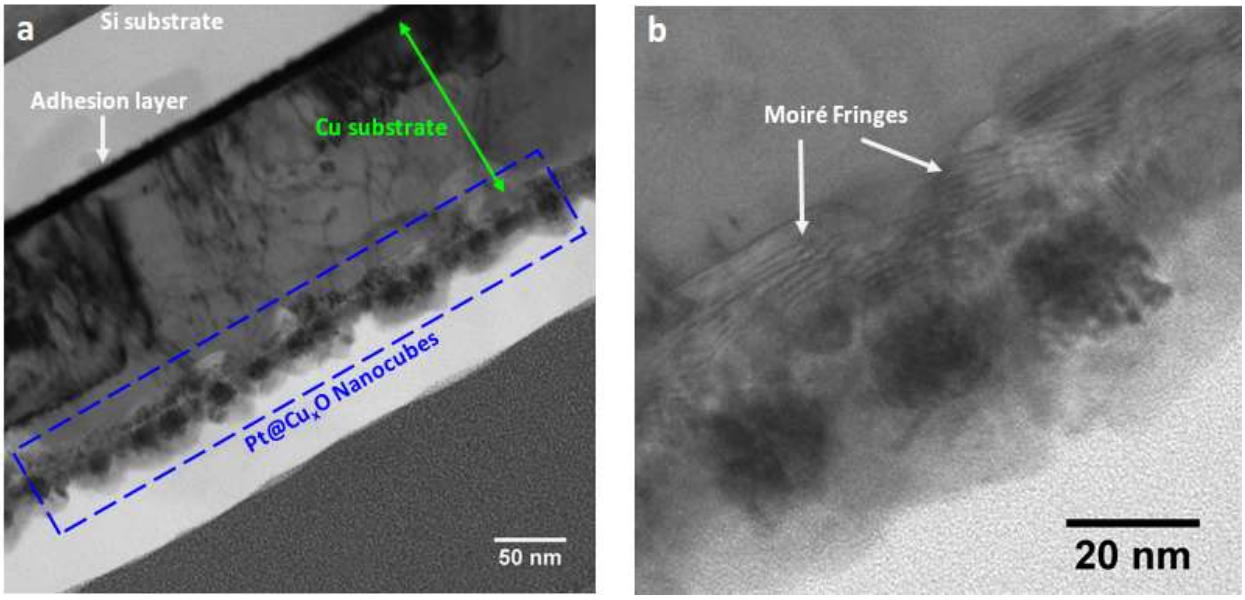

Figure 3.13: **a)** and **b)** Cross sectional TEM images of Pt@Cu_2O nanostructures on Cu substrate.

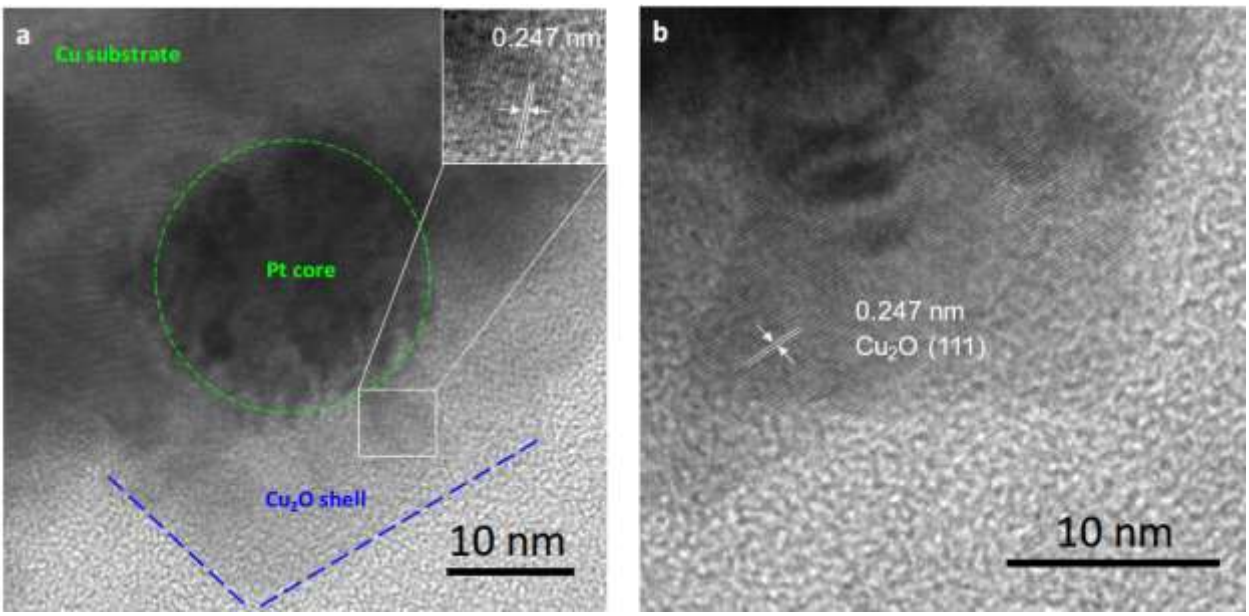

Figure 3.14: a) and **b)** High resolution TEM analysis of Pt@Cu_2O.

While XPS and XRD both indicate the dominant oxide to be Cu_2O, contribution from the underlying Cu substrate made it difficult to differentiate signals from the shell and Cu substrate. Therefore, to confirm the presence of Cu_2O, lattice resolution TEM of the shell was carried out. High resolution TEM of the core shell cross sections shows the presence of a crystalline shell surrounding the Pt core. The *d* spacing of the shell material was determined to be 0.247 nm, which is in excellent agreement with the (111) lattice spacing for Cu_2O.[16] No other *d*-spacings as displayed in **Table 3.4** were identified through HRTEM analysis. It worth noting that due to the nature of the cross section and impact of Moiré patterns limiting clear visualization of the Pt-Cu_xO, the co-existence of Cu_2O and CuO, cannot be completely ruled out. However, TEM, XRD and XPS all indicate that the shell is comprised of primarily of Cu_2O.

Table 3.4: Lattice *d*-spacing associated with different crystalline phrases of Cu, Cu_2O and CuO.[16,17]

D spacing (nm)	Crystalline Lattice Assignment
0.181	Cu (200)
0.208	Cu (111)
0.211	Cu_2O (200)
0.231	CuO (111)
0.246	Cu_2O (111)
0.251	CuO (002)
0.302	Cu_2O (200)

3.4 Application of Pt@Cu_2O Nanocubes

In recent years noble metal@Cu_2O nanoparticles, in particular Pt based nanoparticles have been shown to exhibit excellent electrocatalytic activity toward glucose oxidation and hydrogen peroxide and oxygen reduction, resulting from the electronic and structural effects between core and shell.[18] Au@Cu_2O nanoparticles have also been effective in gas sensor application,[19] these gas sensing applications can also be achieved using Ag@Cu_2O and Pd@Cu_2O nanoparticles.[20] Au@Cu_2O nanoparticles also have proven effective as non-enzymatic glucose sensors,[21] similar to that of the Pt@Cu_2O nanocubes synthesized in this project. The Pt@Cu_2O nanocubes were tested for glucose sensing applications. Electrochemical glucose testing of the substrates was carried out by Dr. Vuslat J. Buk at Tyndall National Institute. The results shown in **Figure 3.15** that the core-shell cubic nanostructures have potential for applications in glucose sensing as in **Figure 3.15 a)** the substrates reaction to glucose within an alkaline environment is shown and demonstrates the cycle of oxidation and reduction that the Cu undergoes. The samples further demonstrate their suitability to glucose sensing in comparison to the blank substrate which can be seen in **Figure 3.15 c).** These nanoparticles were further tested to produce a calibration curve and to demonstrate the substrate's reproducibility which can be seen **Figure 3.16.**

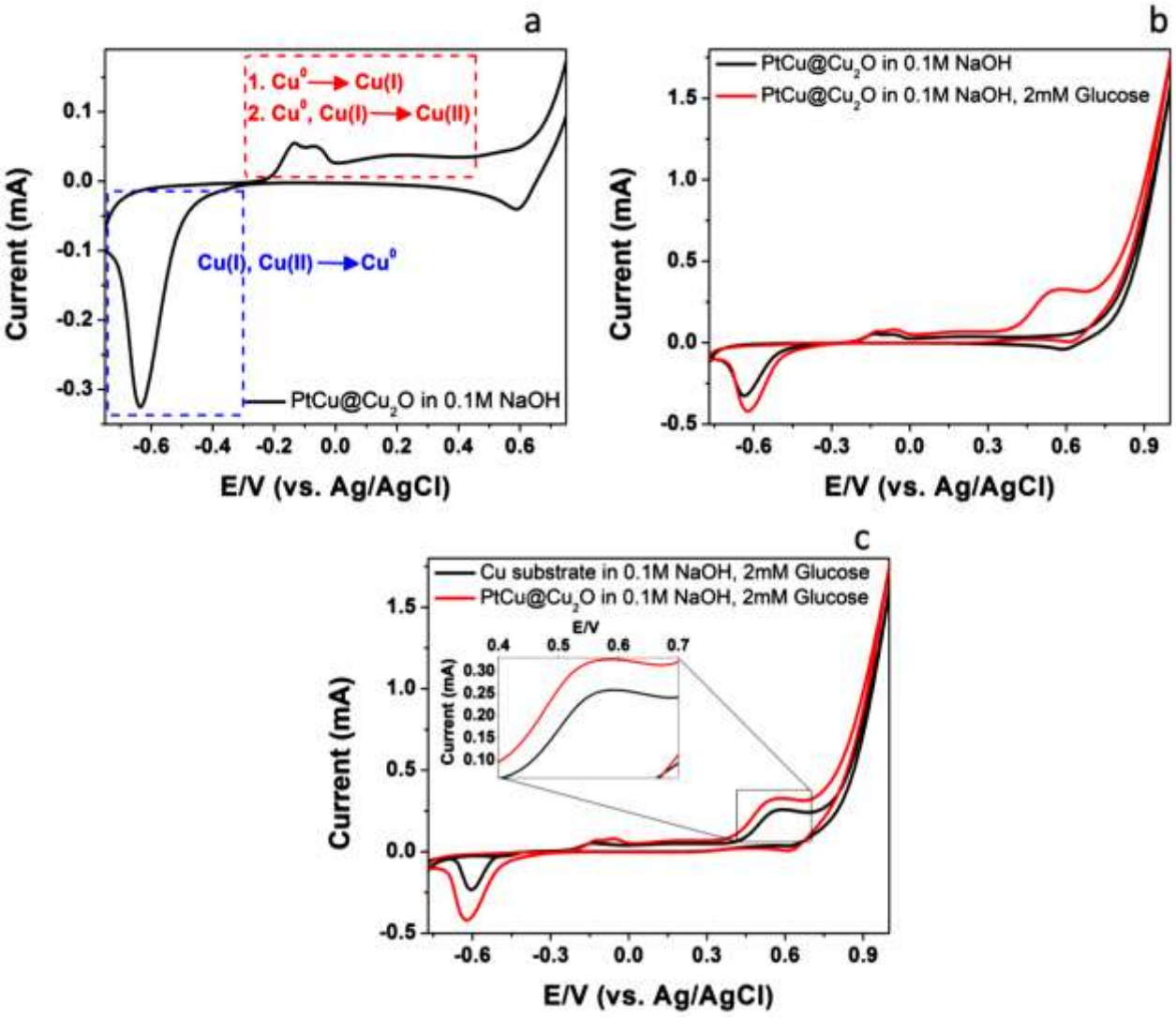

Figure 3.15: Cyclic voltammetry studies of functionalized and blank wafers in **a)** NaOH solution in the **b)** presence and absence of glucose and **c)** comparison of blank and functionalized wafers in presence of glucose.

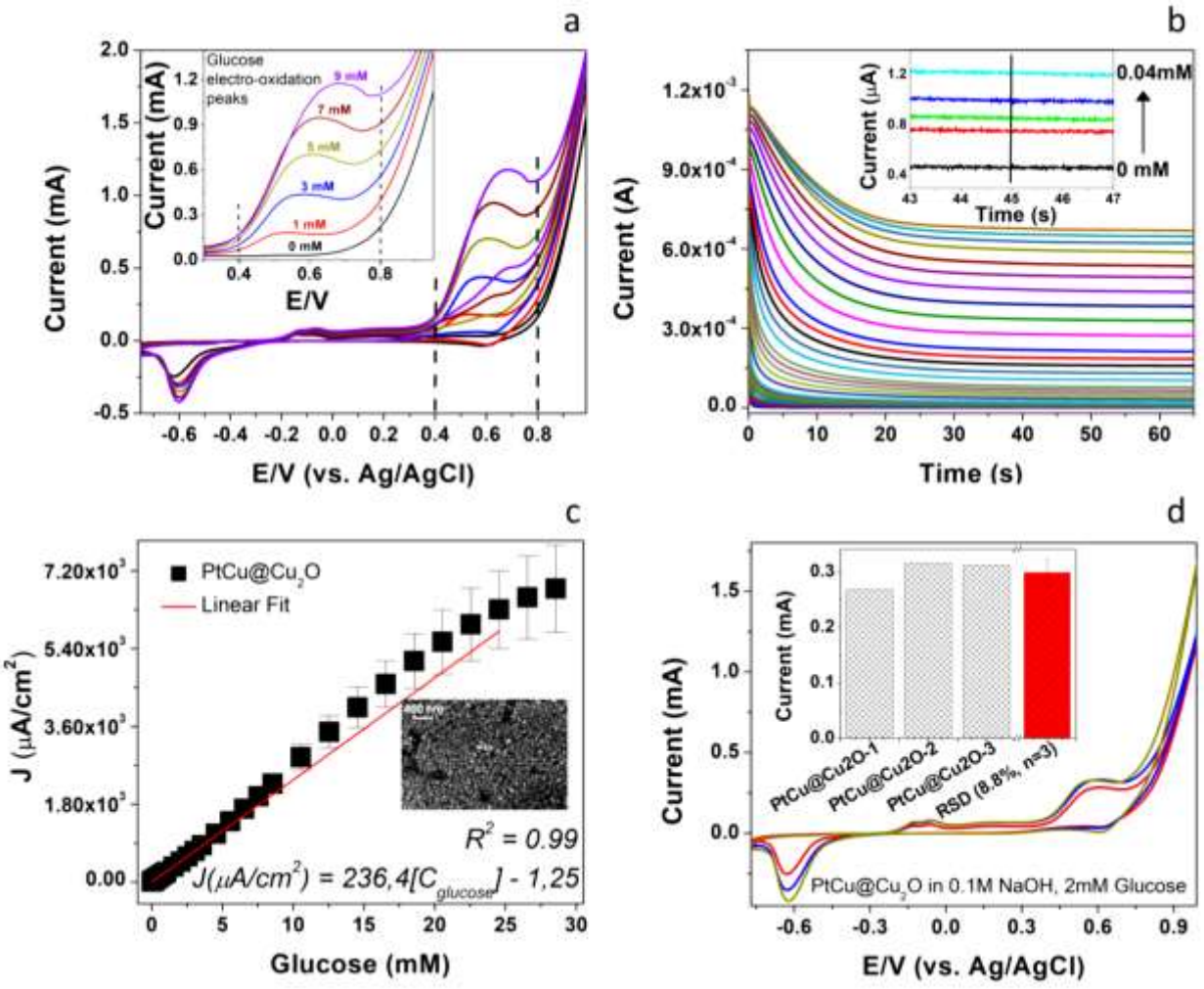

Figure 3.16: a) Cyclic voltammetry response towards increased conc. of glucose, **b)** calibration study with chronoamperometry **c)** corresponding calibration curve and **d)** reproducibility of substrates.

These results demonstrate that each addition of glucose into the electrochemical cell showed an increase in the current levels. The calibration curve shown in **Figure 3.16 c)** has a linear increase corresponding to the increase in glucose within the electrochemical cell. The linear range for the samples is found to be 0.01 – 24.55 mM, with a sensitivity of 236.4 µA/mM cm^2 and a detection limit of 10 µM. The electrochemical analysis demonstrates that these PtCu@Cu_2O nanocubes supported on Cu substrates are highly suitable to be used as a glucose sensing probe.

The final aspect studied in this work was the potential to extend the solid state formation of Pt@Cu_2O core shell nanostructures to other systems. Following the same procedure using the DAD SAM, citrate stabilized gold (Au) nanoparticles were used instead of the PtNP. AuCu_2O hybrid core–shell nanoparticles not only combine the optical signatures of Cu_2O nanoshells and the plasmonic properties of Au nanoparticles but exhibit further enhanced and expanded plasmonic tunability as well due to the dielectric properties of the Cu_2O shells surrounding the Au cores.[22] To date the most commonly used method to synthesis they core shell nanostructures is through solution based methods, therefore, the ability to synthesis via a solid state process would be highly beneficial. **Figure 3.17** shows the spherical Au nanoparticles both before and after the annealing process. It is clear to see that these particles possess a cubic morphology after being annealed at the higher temperature of 450°C in comparison to the 350°C annealing temperature used for the Pt counterparts.

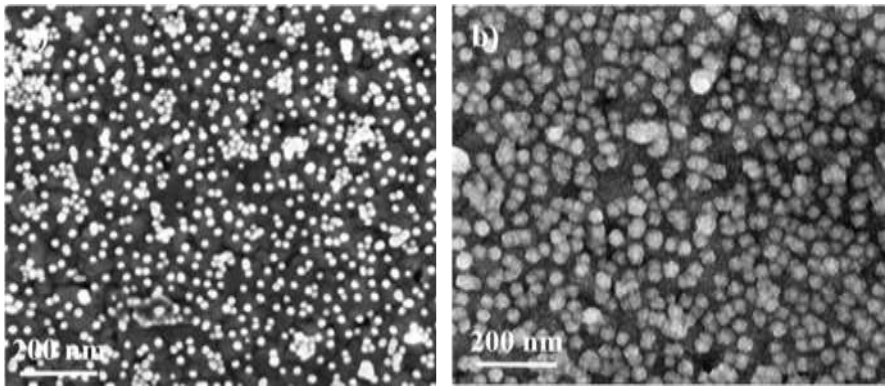

Figure 3.17: SEM images of Au nanoparticles supported on Cu substrates **a)** unannealed and **b)** annealed.

The results produced using the Au nanoparticles in place of the Pt highlight not only more dense coverage of the underlying Cu substrate but distinctive faceted structures which have a large surface area. The large surface area would contribute to the particles applications in catalysis. However, this work is currently being conducted and will require further investigation.

These preliminary results are very promising and show strong potential for the application of the solid state process developed in this work to be extended to other metal-semiconductor systems.

3.5 Exploring the reaction parameters leading to the formation of the Pt@Cu_2O nanocubes

3.5.1 The influence of the DAD SAM as a structure directing agent

It is well known that the morphology of Cu_2O plays a vital role in their physical and chemical properties so being able control this parameter is very useful. Shape controlled Cu_2O nanocrystals are predominantly prepared by solution-based methods. Typically, a copper precursor salt in the presence of a capping ligand that acts as a structure directing agent and a reducing agent, results in the formation of shape-controlled nanostructures. Zhang *et al.* demonstrated selective surface stabilization using PVP on {111} facets to obtain different Cu_2O morphologies.[23] Using cetyltrimethylammonium (CTAB) as the surfactant, Gou and Murphy fabricated regular oxide Cu_2O nanocubes.[24] Amines are a commonly used capping ligand in the shape controlled synthesis of various metal and metal oxide nanoparticles.[25,26] Therefore, the role of the DAD SAM on the Cu substrate and its influence on the formation of the cubic nanostructures was further studied. While XPS analysis confirmed no N 1s peak indicating that the SAM is removed during the thermal anneal, the amine may play a role as a structure-directing agent in earlier stages of the annealing process.

The role of the DAD SAM on the immobilisation of the PtNP were first evaluated using Cu1. A clean, oxide-free Cu substrate was immersed in a solution of the PtNP. A Cu substrate, modified with a DAD SAM, was immersed in the same solution of PtNP for the same amount of time. **Figure 3.18** shows SEM images of as-received Cu, Cu + PtNP in the absence of a SAM and Cu + PtNP in the presence of a SAM. It is clear that when the SAM is not present

there is little or no adsorption of PtNP on the Cu substrate indicating its importance in immobilising the PtNP.

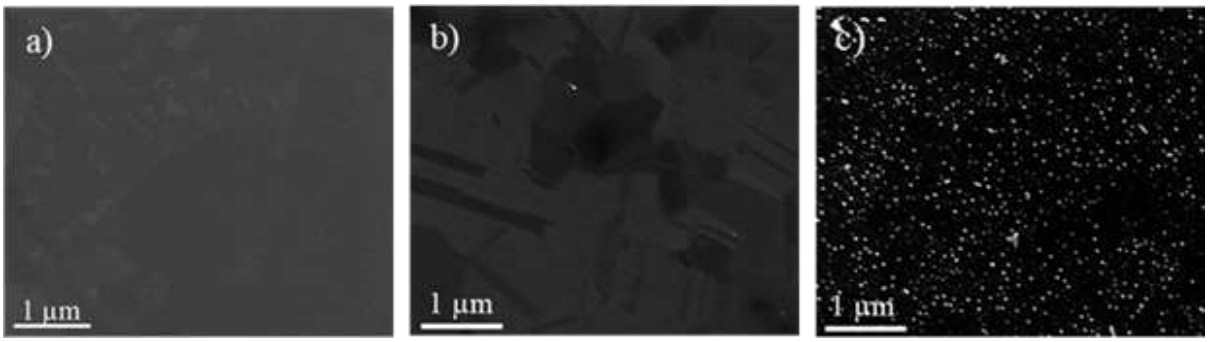

Figure 3.18: SEM of **a)** as-received Cu1 **b)** Cu1 with no SAM but with PtNPs and **c)** Cu1 with SAM + PtNPs.

The role of the DAD ligand to act as a structure-directing agent was then evaluated. **Figure 3.19 a)** shows a SEM image of a Cu substrate that was functionalised with DAD (no NPs present). The substrate was then annealed at 350°C under the flow of forming gas and cooled in a sealed reactor cell. These conditions produced faceted structures. **Figure 3.19 b)** shows an as-received substrate that hasn't been treated with DAD. This doesn't show any signs of faceted structures after being annealed under the same conditions demonstrating the role of DAD as a structure-directing agent.

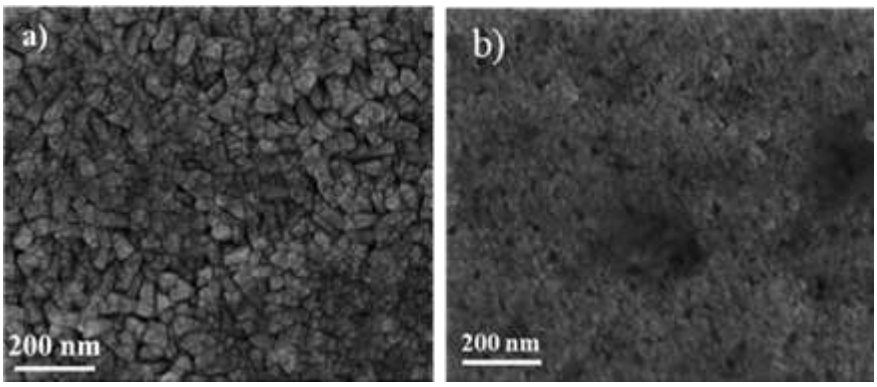

Figure 3.19: SEM image of Cu wafer after annealing **a)** with DAD SAM **b)** with no DAD SAM

3.5.2 Influence of the Annealing Environment

Under normal synthesis conditions the substrates are annealed under a flow of forming gas (5% H_2/Ar) at 350°C for 40 min after which time the cell taps are closed, during the cooling phase, to seal the cell. In order to evaluate the importance of the ambient during the heating and cooling phase a number of conditions where tested as summarised in **Table 3.5**. Annealing condition 1 used the standard synthesis conditions where annealing was carried out under a flow of H_2/Ar and the cooling was carried out in a sealed cell. As shown in the SEM images in **Figure 3.20** the Cu1, Cu2 and Cu3 substrates formed facetted nanostructures, but the Cu1 and Cu2 had the most well-defined nanocubic structures. We hypothesized that the cubic nanostructures may form from the presence of oxygen in the cell at some stage in the process as the composition of the shell material was determined to the Cu_2O. Annealing condition 2 involved annealing and cooling the substrates in air, which led to considerable oxidation of the surface substrate, as to be expected, which is also indicated in the SEM images in **Figure 3.20**. Annealing condition 3 involved annealing the substrates under a flow of H_2/Ar and maintaining the flow of H_2/Ar during the cooling period. SEM analysis, shown in **Figure 3.20,** demonstrates that under these conditions no cubic nanostructures were formed on the Cu1, Cu2 or Cu3 substrates, with the PtNP retaining their spherical morphology. This result suggests that the continual flow of H_2/Ar prevented the morphology change which was likely induced by oxidation. The exact source of this oxygen is unclear; in principle the H_2/Ar atmosphere should be maintained in the sealed cell, the lower pressure of the sealed cell upon cooling may facilitate leaking air into the cell from the surrounding ambient.

Table 3.5: Results of Cu substrates annealed under different environments.

Annealing Conditions	*Environment*		*Effects on the Cu Wafer*		
	Annealing	***Cooling***	***CMP***	***PVD***	***CCAD***
1	FG	Sealed FG	Cubes	Faceted Structures	Faceted Structures
2	Air	Sealed Air	Oxidation	Oxidation	Oxidation
3	FG	Flowing FG	No Change	Faceted Structures	No Change

FG = forming gas (5% H_2/Ar)

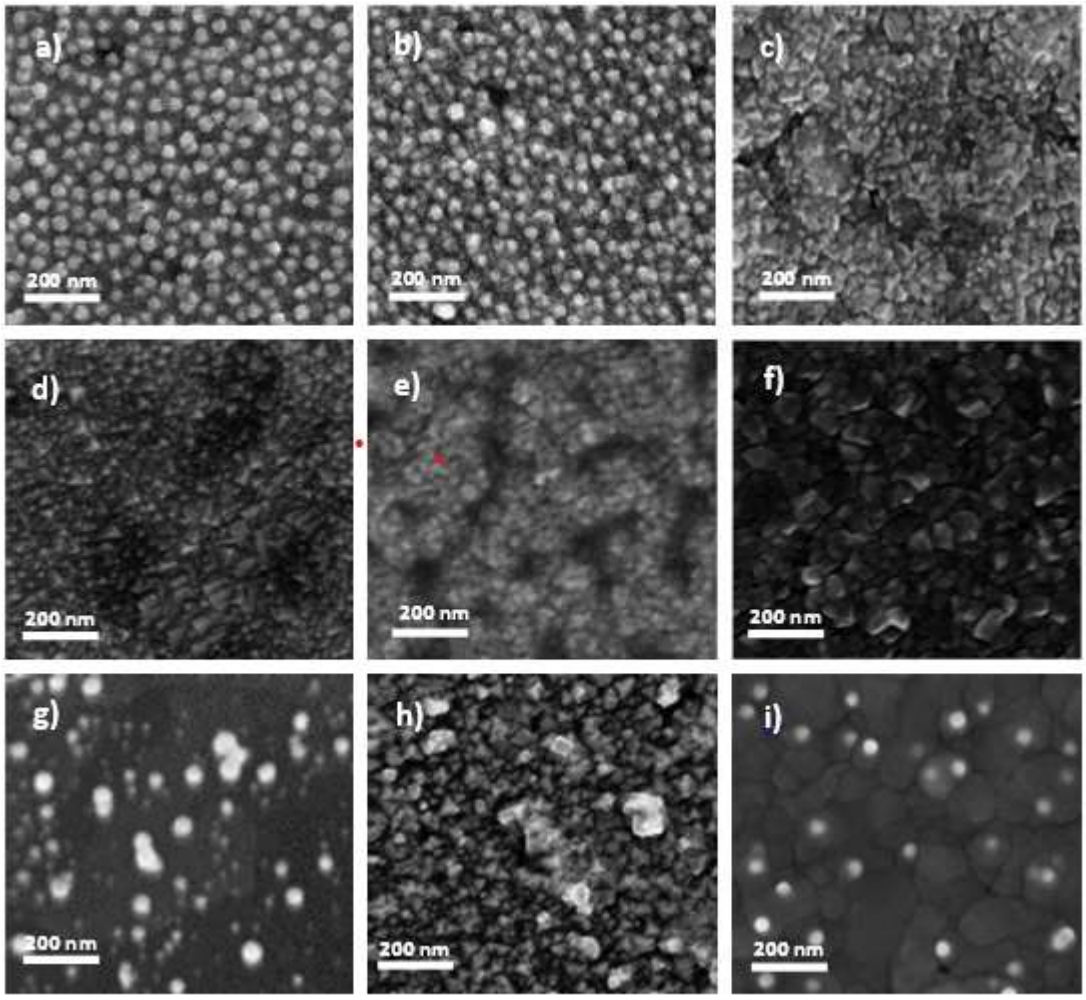

Figure 3.20: a) Cu1 **b)** Cu2 and **c)** Cu3 wafer after being annealed under conditions 1. **d)** Cu1, **e)** Cu2 and **f)** Cu3 wafer after being annealed under conditions 2. **g)** Cu1, **h)** Cu2 and **i)** Cu3 condition after being annealed under conditions 3.

3.6 Exploring Surface Roughness; NP coverage and Annealing Temperatures for Thin Film Development

The initial purpose of this research was to make Pt thin films on a Cu substrate by exploiting the melting point depression of PtNP. In order to determine this melting point depression the PtNP were annealed at higher temperatures. The effects of the surface roughness on the NP coverage was also explored.

3.6.1 Influence of the Annealing Temperature

Cubic core-shell nanostructures were formed when the Cu1 substrates decorated with PtNP were annealed at 350°C. As previously mentioned, the initial aim of this work was to achieve a uniform coverage of PtNP on a Cu substrate, which on annealing would form a Pt film. The process exploits the melting point depression of nanoparticles, which is the reduced melting temperature of a substance compared to the bulk, as dimensions of a material decrease towards the atomic scale. Nanoparticles have significantly greater surface area to volume ratios compared to bulk materials and this dramatically alters their thermodynamic properties. For example, experimental studies have shown that the melting point of 4.3 nm Ni nanoparticles was found to be 925°C, with bulk Ni having a melting point of 1455°C.[27] Theoretical studies have predicted that PtNP with a diameter of 2 nm could melt at temperatures as low as 500°C.[28] This is relevant to the PtNP used in this work as they have a dendritic structure consisting of small Pt crystallites with a diameter of ~2 nm. The influence of annealing the substrate at a higher temperature was evaluated for the Cu1, Cu2 and Cu3 wafers and is summarised in **Table 3.6**. Annealing temperatures of 450°C, 550°C and 650°C was evaluated.

Table 3.6: Annealing temperatures of the different substrates.

Annealing	***Effects on the Cu Wafer***		
Temperature	***Cu1***	***Cu2***	***Cu3***
450°C	Nanoparticles visible	Partial De-wetting of Cu	Nanoparticles visible
550°C	Film-like Structure	De-wetting of Substrate	De-wetting of Substrate
650°C	De-wetting of Substrate	De-wetting of Substrate	De-wetting of Substrate

A key issue encountered on annealing the substrates at higher temperatures was de-wetting of the Cu, which is evident from the SEM analysis in **Figure 3.21**. De-wetting was most pronounced for the Cu2 wafer which was attributed to the relatively thin layer of Cu (30 nm) on the surface.

De-wetting of the Cu2 substrate was apparent at 450, 550 and 650°C, as shown in **Figure 3.21 (a-c). Figure 3.21 (d-f)** show the Cu1 substrate after annealing at 450°C, 550°C and 650°C. At 450°C, nanoparticles are visible on the surface. At 550°C, the surface is relatively smooth with no nanoparticles observed by SEM analysis. It is possible that at 550°C, the PtNP melted to form a Pt film or CuPt film on the surface, however further analysis would be required to confirm this finding. At 650°C, de-wetting of the Cu1 substrate is clearly observed. The Cu3 water, which has the thickest layer of Cu but a considerably rougher surface than the Cu1 or Cu2 substrates are shown in **Figure 3.21 (g-i).** At an anneal temperature of 450°C, distinct nanoparticles are visible on the surface, however at the higher temperature of 550°C significant de-wetting occurs, which is in contrast to the Cu1 where the surface remained smooth at 550°C.

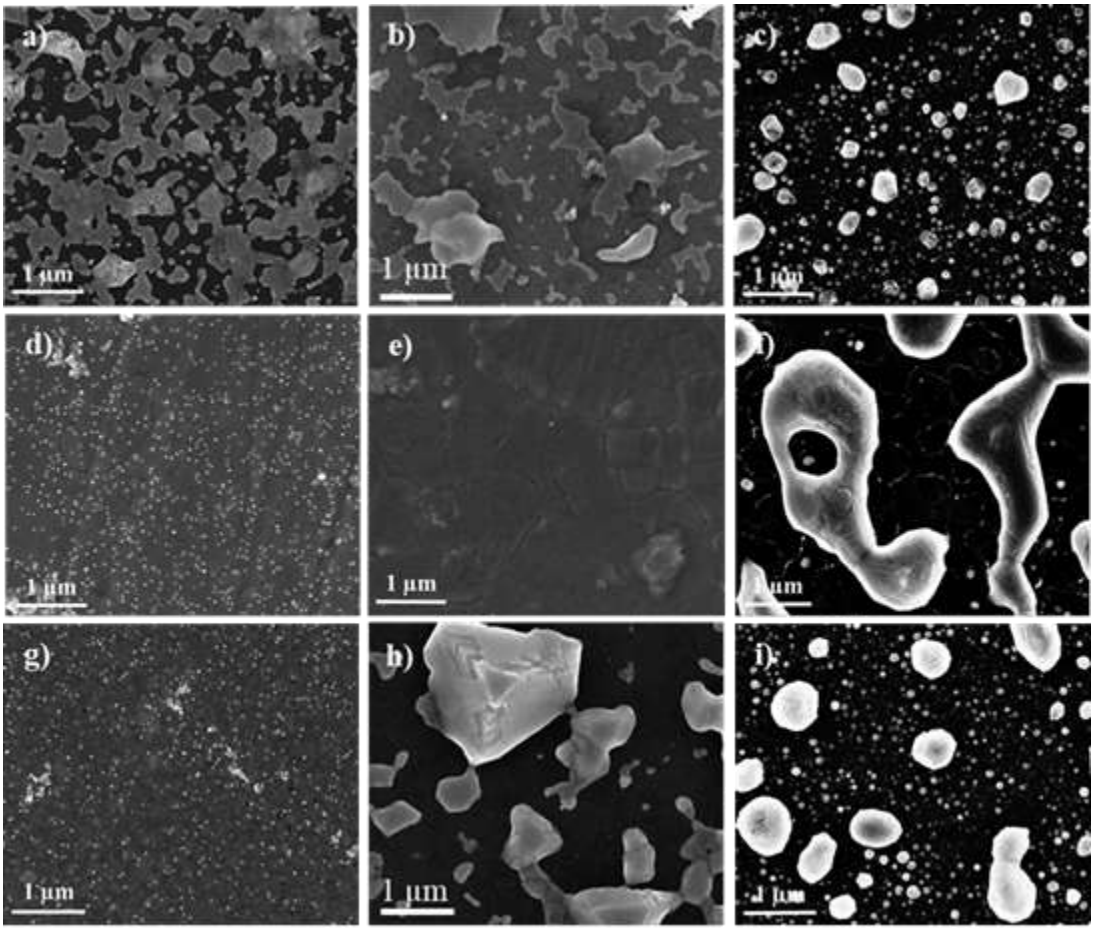

Figure 3.21: Cu2 wafer after annealing at **a)** 450°C, **b)** 550°C and **c)** 650°C. Cu1 wafer after annealing at **d)** 450°C, **e)** 550°C and **f)** 650°C. Cu3 wafer after annealing at **g)** 450°C, **h)** 550°C and **i)** 650°C.

XRD was carried on the Cu1 sample that was annealed at 550°C, **Figure 3.21 e)** to determine the composition of the smooth surface produced. An as-received Cu1 wafer was also analysed to be used as a control to compare to the changes that occurred on the surface of the treated sample as a result of annealing. The results of this analysis can be seen in **Figure 3.22.**

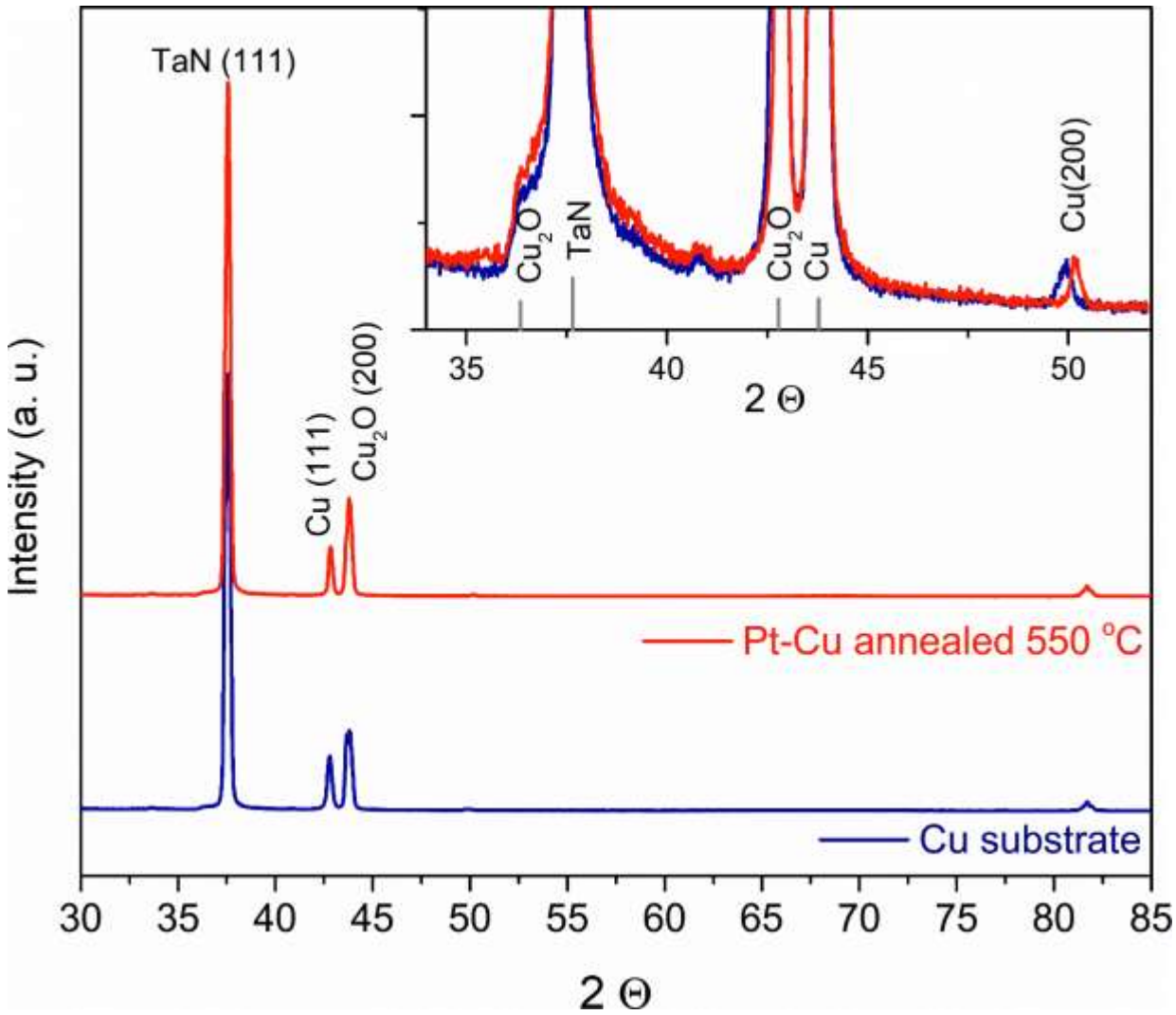

Figure 3.22: XRD analysis of as-received and treated Cu1 wafer.

Figure 3.22 shows the XRD analysis of a bare Cu substrate and the substrate after PtNP deposition followed by annealing at 550°C. Both XRD patterns are similar and show the metallic Cu (111) diffraction peak at 43.4 and the Cu_2O (200) peak at 42.3. Notably there is an intense peak centred at 37.5. Magnification of this peak (**Figure 3.22** inset) shows a highly unsymmetrical baseline. A shoulder peak is visible to the left side of this peak and is attributed to the Cu_2O (111) peak. The main dominate peak was absent in previous XRD analysis and this peak may be attributed to the TaN adhesion layer, which is in excellent agreement with the location of the TaN(111) diffraction peak.[29] The presence of this peak may be due to damage of the Cu overlayer ***e.g***. from tweezers etc. XRD analysis can often

by useful in evaluating alloy formation.[30] Due to the dendritic nature of the PtNPs which are composed of very small Pt crystallites, clear diffraction peaks associated the PtNPs were not observed. It is interesting to note that an upward shift in the Cu (200) diffraction peak is observed after annealing the Pt decorated substrates. This upward shift in the Cu(200) refection is characteristic of alloy formation due to lattice contraction.[31] Further analysis such as EDX mapping would be required to evaluate the surface composition and confirm the presence of a CuPt alloy.

The XRD results shown in **Figure 3.22** indicate that the smooth surface seen in **Figure 3.21 e)** was not a Pt/Cu alloy or a Pt film. The results suggest that the smooth surface primarily consists of Cu_2O that has formed a film-like structure on the surface. As no Pt or Pt/Cu was detected on the annealed surface and the peaks for both the substrate as received and the substrate that was treated were almost identical it strongly indicates that the surface was mainly Cu_2O. Further analysis such as XPS should be done to confirm these findings.

3.6.2 Influence of Cu Substrate and Surface Roughness

The nature of the Cu substrate including Cu thickness and surface roughness was then investigated. Three Cu substrates with different thicknesses of Cu and varying roughness were used. All substrates consisted of Cu deposited onto a Si wafer with a tantalum nitride adhesion layer. The work reported thus far was carried out on a chemically mechanically polished (CMP) wafer. **Table 3.1** summarises the properties of each Cu substrate.

Figure 3.23 shows AFM images and SEM images of the Cu substrates. Both the Cu1 and Cu2 substrates have relatively smooth surfaces while the Cu3 substrate is characterised by a high degree of roughness (Rq > 5 nm).

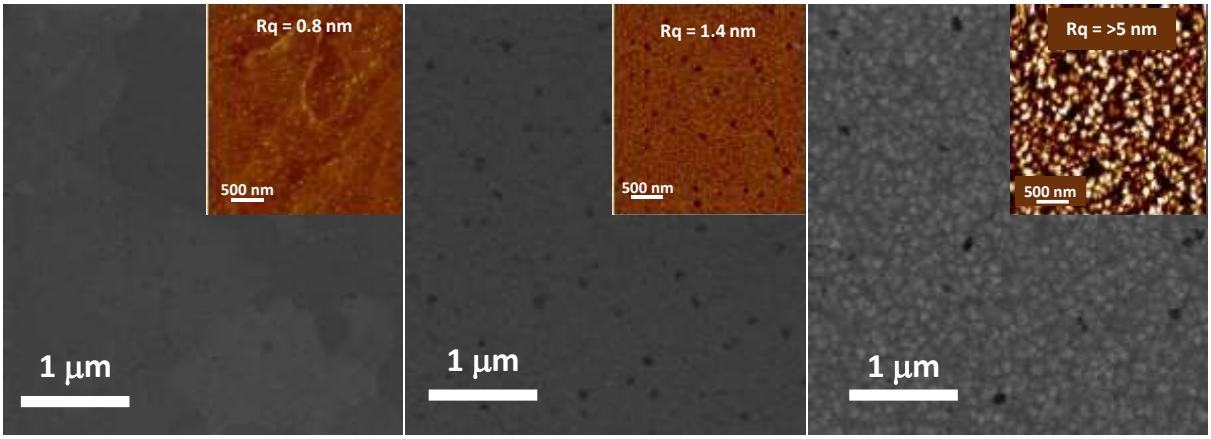

Figure 3.23: Scanning electron microscopy image of **a)** Cu1, **b)** Cu2 and **c)** Cu3 as-received (inset is the atomic force microscopy image of each substrate).

The effect of substrate surface roughness on PtNP deposition was evaluated by measuring the time taken to reach saturation coverage after immersion into the PtNP solution.

Figure 3.24 shows a plot of nanoparticle coverage versus deposition time for the Cu1 and Cu3 wafer. The nanoparticle coverage begins to plateau after ~30 min immersion time. As the PtNP solution was slightly acidic due to the presence of citrate, immersion times longer than 32 min were not carried out due to etching of the Cu substrate. The maximum coverage recorded for the Cu1 wafer was 2700 nanoparticles per 1.36 μm^2 after 32 min. There was only a modest increase in coverage from 15 min to 32 min, so consequently 15 min was taken as the optimal time for nanoparticle deposition while preventing any etching of the Cu substrate. **Figure 3.24** also shows the nanoparticle coverage versus time for the Cu3 wafer. PtNP deposition onto the Cu3 wafer under the same conditions as the Cu1 wafer has a different profile as clearly evident from comparison of the plots. The rate of nanoparticle deposition is considerably slower on the Cu3 substrate compared to the Cu1 substrate. Nanoparticle deposition on the Cu3 wafer shows a linear profile in the first 32 min as demonstrated in **Figure 3.18 c)**, with a 7-fold decrease in coverage compared to the Cu1, after that time. Nanoparticle

coverage of the Cu3 substrate increased with longer immersion times, and began to plateau ~120 min, with coverage at 1050 nanoparticles per 1.36 µm^2.

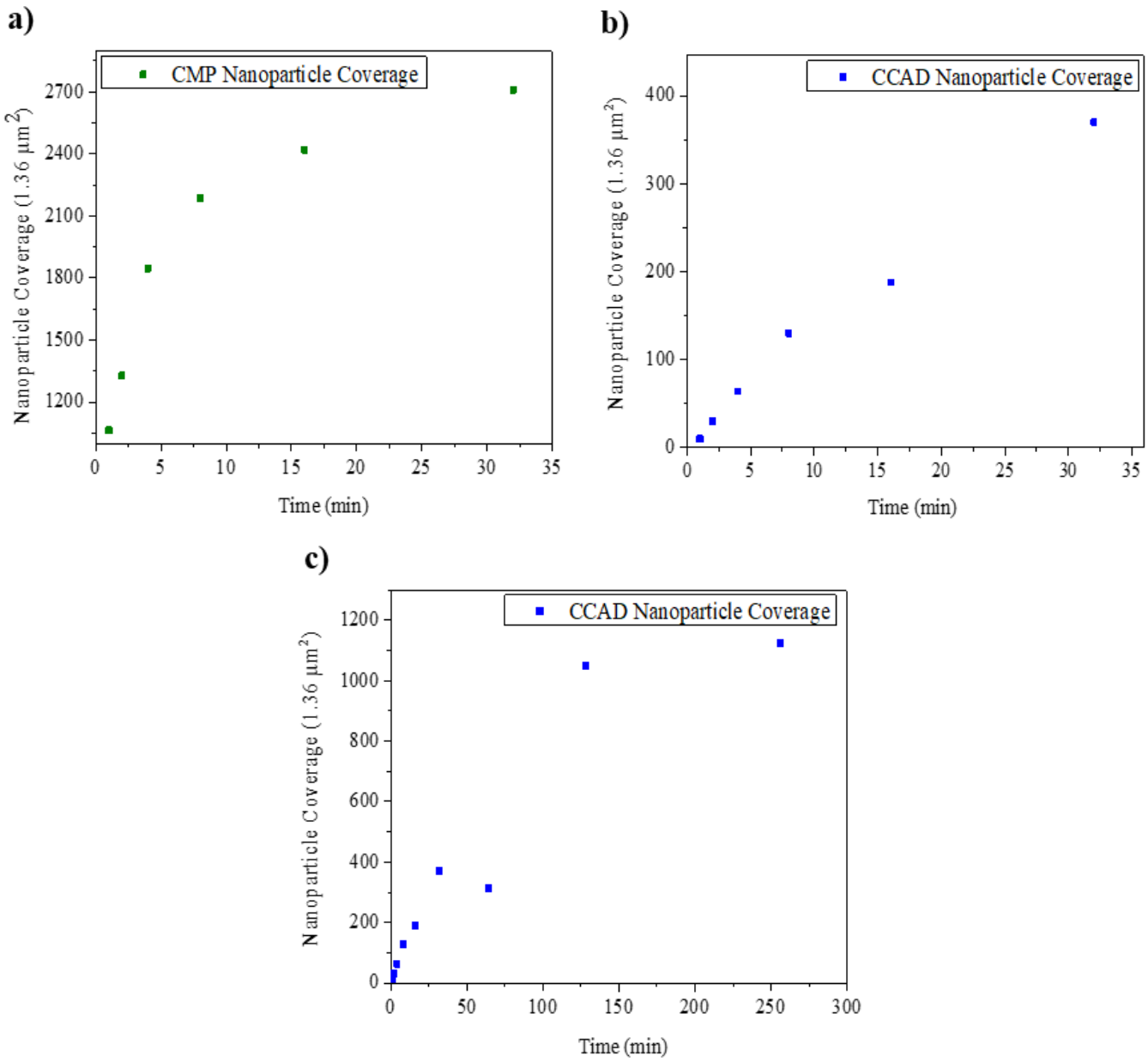

Figure 3.24: Time Deposition study on **a)** Cu1 wafer, **b)** Cu3 wafer and **c)** Cu3 wafer reaction after 300 min.

With a longer immersion time etching of the substrate was also apparent from SEM. **Figure 3.25 a)** and **b)** show the Cu3 substrate after 128 min and 256 min, respectively. De-wetting of some parts of the substrate was clearly evident by SEM analysis and longer

immersion times in the nanoparticle solution also results in the deposition of agglomerates of nanoparticles. The optimal time to achieve the highest coverage on the Cu3 substrates while minimising damage to the wafer is 120 min, however the maximum coverage obtainable is still 2.5 times lower than that achievable on the Cu1 wafer. While rough surfaces are characterised by higher surface area which can be beneficial for many applications such as sensing and catalysis, this study demonstrated that surface roughness has a clear negative impact on the PtNP loading which is an important finding for potential applications.

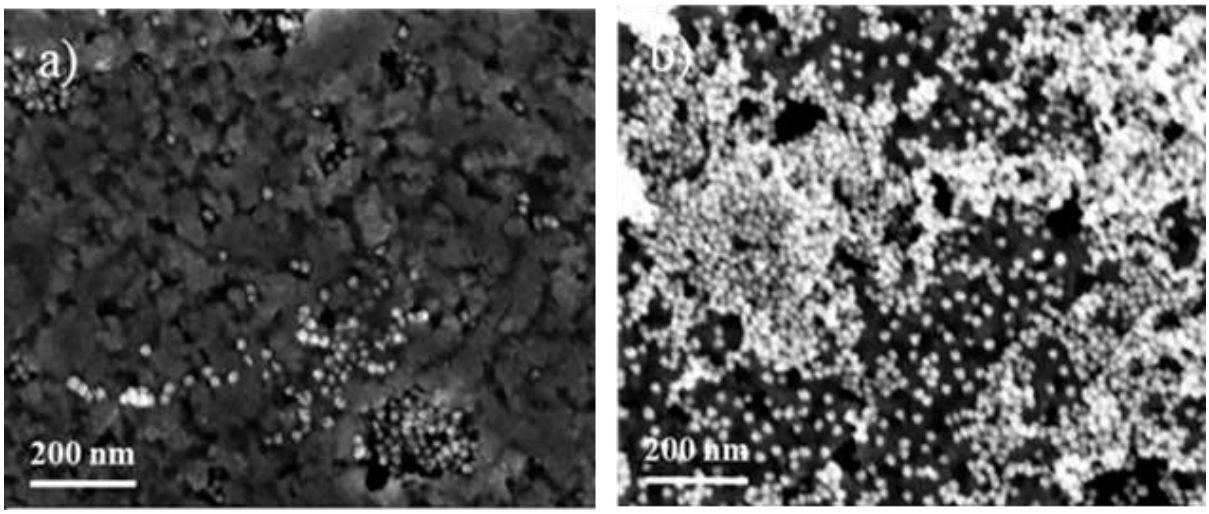

Figure 3.25: Cu3 wafer with PtNP deposition time of **a)** 128 min and **b)** 256 min.

3.7 Conclusions

Characterising these Pt@Cu_2O nanocubes involved a range of analytical techniques in order to determine the factors that effected their formation. It was determined that the PtNPs were dendritic and that through their synthesis and subsequent size selection uniform particles of ~30 nm were synthesised. Further analysis determined that the ideal temperature in which to anneal these substrates was 350°C for 30 min using a furnace with a heating rate of 32°C/min.

XPS analysis demonstrated that the native oxide removal step in the synthesis was successful as only trace amounts of surface oxide were present in the Pt decorated samples. This analysis also indicated that the nanocubes were core-shell in structure as the Pt peaks observed in the unannealed sample were not present in their annealed counterpart. This demonstrated that the Pt had been encapsulated within a Cu_2O shell which was shown in the Cu LMM Auger peak. XPS analysis was also able to demonstrate the suitability of the SAM used as its peaks decreased when protonation of the terminal amine group had occurred by the citrate stabilised PtNP. The XRD analysis performed corroborated the finding of the XPS analysis.

Confirmation of the core-shell structure of these nanoparticles was achieved through XTEM. The results of this analysis clearly demonstrated the presence of a dense core consisting of Pt as well as the underlying copper and adhesion layer. The *d* spacing of the shell was calculated to be 0.247 nm, which is in agreement with the lattice spacing of Cu_2O. The finding obtained from XTEM strongly agree with the findings from the XPS and XRD analysis.

3.8 References:

(1) Kim, C.; Oh, J.-G.; Kim, Y.-T.; Kim, H.; Lee, H. Platinum Dendrites with Controlled Sizes for Oxygen Reduction Reaction. *Electrochemistry Communications* **2010**, *12* (11), 1596–1599.

(2) Song, Y.; Yang, Y.; Medforth, C. J.; Pereira, E.; Singh, A. K.; Xu, H.; Jiang, Y.; Brinker, C. J.; van Swol, F.; Shelnutt, J. A. Controlled Synthesis of 2-D and 3-D Dendritic Platinum Nanostructures. *J. Am. Chem. Soc.* **2004**, *126* (2), 635–645.

(3) Peng, Z.; Yang, H. Designer Platinum Nanoparticles: Control of Shape, Composition in Alloy, Nanostructure and Electrocatalytic Property. *Nano Today* **2009**, *4* (2), 143–164.

(4) Sohn, Y.; Pradhan, D.; Zhao, L.; Leung, K. T. Anomalous Oxidation Resistance of "Core-Only" Copper Nanoparticles Electrochemically Grown on Gold Nanoislands Prefunctionalized by 1,4-Phenylene Diisocyanide. *Electrochem. Solid-State Lett.* **2012**, *15* (4), K35.

(5) Radi, A.; Pradhan, D.; Sohn, Y.; Leung, K. T. Nanoscale Shape and Size Control of Cubic, Cuboctahedral, and Octahedral Cu−Cu_2O Core−Shell Nanoparticles on Si(100) by One-Step, Templateless, Capping-Agent-Free Electrodeposition. *ACS Nano* **2010**, *4* (3), 1553–1560.

(6) Tissot, H.; Wang, C.; Stenlid, J. H.; Panahi, M.; Kaya, S.; Soldemo, M.; Ghadami Yazdi, M.; Brinck, T.; Weissenrieder, J. Interaction of Atomic Hydrogen with the Cu_2O(100) and (111) Surfaces. *J. Phys. Chem. C* **2019**, *123* (36), 22172–22180.

(7) Wang, C.; Tissot, H.; Escudero, C.; Pérez-Dieste, V.; Stacchiola, D.; Weissenrieder, J. Redox Properties of Cu_2O(100) and (111) Surfaces. *J. Phys. Chem. C* **2018**, *122* (50), 28684–28691.

(8) Lee, S.; Jeong, S.; Kim, W. D.; Lee, S.; Lee, K.; Bae, W. K.; Moon, J. H.; Lee, S.; Lee, D. C. Low-Coordinated Surface Atoms of CuPt Alloy Cocatalysts on TiO_2 for Enhanced Photocatalytic Conversion of CO_2. *Nanoscale* **2016**, *8* (19), 10043–10048.

(9) Wakisaka, M.; Mitsui, S.; Hirose, Y.; Kawashima, K.; Uchida, H.; Watanabe, M. Electronic Structures of Pt−Co and Pt−Ru Alloys for CO-Tolerant Anode Catalysts in Polymer Electrolyte Fuel Cells Studied by EC−XPS. *J. Phys. Chem. B* **2006**, *110* (46), 23489–23496.

(10) Kleiman, G. G.; Sundaram, V. S.; Barreto, C. L.; Rogers, J. D. ESCA Determination of the Electronic Structure of Pt□Cu Alloys. *Solid State Communications* **1979**, *32* (11), 919–923.

(11) Lee, Y.-S.; Lim, K.-Y.; Chung, Y.-D.; Whang, C.-N.; Jeon, Y. XPS Core-Level Shifts and XANES Studies of Cu–Pt and Co–Pt Alloys. *Surface and Interfaces Analysis* **2000**, *30* (1), 475–478.

(12) Ryskin, N. M.; Torgashov, R. A.; Starodubov, A. V.; Rozhnev, A. G.; Serdobintsev, A. A.; Pavlov, A. M.; Galushka, V. V.; Bessonov, D. A.; Ulisse, G.; Krozer, V. Development of Microfabricated Planar Slow-Wave Structures on Dielectric Substrates for Miniaturized Millimeter-Band Traveling-Wave Tubes. *Journal of Vacuum Science & Technology B* **2021**, *39* (1), 013204.

(13) Artyushkova, K. Misconceptions in Interpretation of Nitrogen Chemistry from X-Ray Photoelectron Spectra. *Journal of Vacuum Science & Technology A* **2020**, *38* (3), 031002.

(14) Graf, N.; Yegen, E.; Gross, T.; Lippitz, A.; Weigel, W.; Krakert, S.; Terfort, A.; Unger, W. E. S. XPS and NEXAFS Studies of Aliphatic and Aromatic Amine Species on Functionalized Surfaces. *Surface Science* **2009**, *603* (18), 2849–2860.

(15) Zhang, H.; Wen, H.; Liu, Z.; Zhang, Q.; Xie, H. TEM Nano-Moiré Evaluation for an Invisible Lattice Structure near the Grain Interface. *Nanoscale* **2017**, *9* (41), 15923–15933.

(16) Zhao, D.; Tu, C.-M.; Hu, X.-J.; Zhang, N. Notable in Situ Surface Transformation of Cu $_2$ O Nanomaterials Leads to Dramatic Activity Enhancement for CO Oxidation. *RSC Adv.* **2017**, *7* (60), 37596–37603.

(17) Cheng, G.; Hight Walker, A. R. Transmission Electron Microscopy Characterization of Colloidal Copper Nanoparticles and Their Chemical Reactivity. *Anal Bioanal Chem* **2010**, *396* (3), 1057–1069.

(18) Jin, J.; Mei, H.; Wu, H.; Wang, S.; Xia, Q.; Ding, Y. Selective Detection of Dopamine Based on Cu2O@Pt Core-Shell Nanoparticles Modified Electrode in the Presence of Ascorbic Acid and Uric Acid. *Journal of Alloys and Compounds* **2016**, *689*, 174–181.

(19) Rai, P.; Khan, R.; Raj, S.; Majhi, S. M.; Park, K.-K.; Yu, Y.-T.; Lee, I.-H.; Sekhar, P. K. Au@Cu2O Core–Shell Nanoparticles as Chemiresistors for Gas Sensor Applications: Effect of Potential Barrier Modulation on the Sensing Performance. *Nanoscale* **2013**, *6* (1), 581–588.

(20) Lin, Y.-K.; Chiang, Y.-J.; Hsu, Y.-J. Metal–Cu2O Core–Shell Nanocrystals for Gas Sensing Applications: Effect of Metal Composition. *Sensors and Actuators B: Chemical* **2014**, *204*, 190–196.

(21) Su, Y.; Guo, H.; Wang, Z.; Long, Y.; Li, W.; Tu, Y. Au@Cu2O Core-Shell Structure for High Sensitive Non-Enzymatic Glucose Sensor. *Sensors and Actuators B: Chemical* **2018**, *255*, 2510–2519.

(22) Zhang, L.; Blom, D. A.; Wang, H. Au–Cu $_2$ O Core–Shell Nanoparticles: A Hybrid Metal-Semiconductor Heteronanostructure with Geometrically Tunable Optical Properties. *Chem. Mater.* **2011**, *23* (20), 4587–4598.

(23) Zhang, D.-F.; Zhang, H.; Guo, L.; Zheng, K.; Han, X.-D.; Zhang, Z. Delicate Control of Crystallographic Facet-Oriented Cu2O Nanocrystals and the Correlated Adsorption Ability. *J. Mater. Chem.* **2009**, *19* (29), 5220.

(24) Gou, L.; Murphy, C. J. Solution-Phase Synthesis of Cu $_2$ O Nanocubes. *Nano Lett.* **2003**, *3* (2), 231–234.

(25) Zhang, Z.; Lu, M.; Xu, H.; Chin, W.-S. Shape-Controlled Synthesis of Zinc Oxide: A Simple Method for the Preparation of Metal Oxide Nanocrystals in Non-Aqueous Medium. *Chem. Eur. J.* **2007**, *13* (2), 632–638.

(26) Zhang, L.; Wang, L.; Jiang, Z.; Xie, Z. Synthesis of Size-Controlled Monodisperse Pd Nanoparticles via a Non-Aqueous Seed-Mediated Growth. *Nanoscale Res Lett* **2012**, *7* (1), 312.

(27) van Teijlingen, A.; Davis, S. A.; Hall, S. R. Size-Dependent Melting Point Depression of Nickel Nanoparticles. *Nanoscale Adv.* **2020**, *2* (6), 2347–2351.

(28) Guisbiers, G.; Abudukelimu, G.; Hourlier, D. Size-Dependent Catalytic and Melting Properties of Platinum-Palladium Nanoparticles. *Nanoscale Res Lett* **2011**, *6* (1), 396.

(29) Elangovan, T.; Murugeshan, S.; Mangalaraj, D.; Kuppusami, P.; Khan, S.; Sudha, C.; Ganesan, V.; Divakar, R.; Mohandas, E. Synthesis and High Temperature XRD Studies of Tantalum Nitride Thin Films Prepared by Reactive Pulsed Dc Magnetron Sputtering. *Journal of Alloys and Compounds* **2011**, *509* (22), 6400–6407.

(30) Saravanan, G.; Khobragade, R.; Chand Nagar, L.; Labhsetwar, N. Ordered Intermetallic Pt–Cu Nanoparticles for the Catalytic CO Oxidation Reaction. *RSC Adv.* **2016**, *6* (88), 85634–85642.

(31) Zhou, S.; Varughese, B.; Eichhorn, B.; Jackson, G.; McIlwrath, K. Pt-Cu Core-Shell and Alloy Nanoparticles for Heterogeneous NOx Reduction: Anomalous Stability and Reactivity of a Core-Shell Nanostructure. *Angew. Chem.* **2005**, *117* (29), 4615–4619.

Chapter Four:

Conclusions and Future Work

4.1 Conclusions and Future Work

This work developed a solid state synthesis to PtCu@Cu_2O nanocubes immobilized on Cu substrates. The nanocubes synthesized by this method are significantly smaller than those synthesized by solid-state methods reported in the literature to date. In fact, the size and morphology control obtainable in our synthesis method rivals that of solution based methods. While solution based methods can enable exceptional control of nanoparticle size, shape and composition, it usually requires the use of stabilizing ligands during the synthesis and consequently the surfaces of the resultant nanoparticles are modified with these capping ligands. Complete removal of capping ligands without compromising the nanoparticles is not trivial and remains a key challenge in the application of nanoparticles. Therefore, a major benefit of the solid state approach is that the nanoparticle surfaces are not passivated by capping ligands, which is a significant advantage in the application of catalysis, electrocatalysis and sensing. Preliminary measurements have demonstrated the use of the PtCu@Cu_2O substrates in glucose sensing applications. Further work would be need to develop this, particularly in the application of selective detection.

Alternative applications for these unique particles could also be further investigated. Pt based nanoparticles have a range of applications such as catalysis, water splitting and fuel cells.[1,2,3] As the core shell nanocubes are supported on a Cu substrate they, would be best suited to a fuel cell that operated in an alkaline or aqueous environment such as the methanol oxidation reaction (MOR).[4] The high density of nanoparticles with strong adhesion to the substrate would be very beneficial for such applications.

This work focused on the immobilisation of Pt nanoparticles onto Cu substrates, however a vast variety of other transition metal nanoparticles could be evaluated. Preliminary tests were carried out using citrate stabilised Au nanoparticles and confirm that our solid state

synthesis method is transferable to other metal nanoparticles. A high density of Au nanoparticles could be immobilised on the Cu substrates with the aid of the diamine self-assembled monolayer. Cubic nanostructures formed when annealed using a slightly higher temperature of 450°C instead of 350°C used for the Pt nanoparticles. Further work is required to optimise the synthesis parameters and also characterise the cubic nanostructures obtained in the Au-Cu substrate system to compare with those obtained using the Pt-Cu substrate system.

In addition to changing the nanoparticle, this method could also be used with a different substrate metal, such as nickel (Ni). Studies have shown that the combination of Pt and Ni are effective in the hydrogen evolution reaction.[5,6] PtNi nanoparticles have been proven to be effective in ORR, and have a greater affinity for the reaction over Pt and PtCo,[3] so further studies could be done in this area using Ni as a substrate in place of its Cu counterpart. Similar to the Cu substrate the Ni surface functionalisation would need to be optimised to deposit a high density of Pt nanoparticles. Annealing the substrates is likely to give rise to nanostructure morphologies different to those observed on Cu substrates, however may yield substrates for potential applications in fuel cells. Ni-Pt systems have received considerable interest in recent years and have been shown to be one of high preforming systems for fuel cell applications.

4.2 References:

(1) Zhou, S.; Varughese, B.; Eichhorn, B.; Jackson, G.; McIlwrath, K. Pt-Cu Core-Shell and Alloy Nanoparticles for Heterogeneous NOx Reduction: Anomalous Stability and Reactivity of a Core-Shell Nanostructure. *Angew. Chem. Int. Ed.* **2005**, *44* (29), 4539–4543.

(2) Kim, C.; Oh, J.-G.; Kim, Y.-T.; Kim, H.; Lee, H. Platinum Dendrites with Controlled Sizes for Oxygen Reduction Reaction. *Electrochemistry Communications* **2010**, *12* (11), 1596–1599.

(3) Wu, D.; Shen, X.; Pan, Y.; Yao, L.; Peng, Z. Platinum Alloy Catalysts for Oxygen Reduction Reaction: Advances, Challenges and Perspectives. *ChemNanoMat* **2020**, *6* (1), 32–41.

(4) Bai, Z.; Yang, L.; Zhang, J.; Li, L.; Hu, C.; Lv, J.; Guo, Y. High-Efficiency Carbon-Supported Platinum Catalysts Stabilized with Sodium Citrate for Methanol Oxidation. *Journal of Power Sources* **2010**, *195* (9), 2653–2658.

(5) Cao, Z.; Chen, Q.; Zhang, J.; Li, H.; Jiang, Y.; Shen, S.; Fu, G.; Lu, B.; Xie, Z.; Zheng, L. Platinum-Nickel Alloy Excavated Nano-Multipods with Hexagonal Close-Packed Structure and Superior Activity towards Hydrogen Evolution Reaction. *Nat Commun* **2017**, *8* (1), 15131.

(6) Du, Y.; Su, J.; Luo, W.; Cheng, G. Graphene-Supported Nickel–Platinum Nanoparticles as Efficient Catalyst for Hydrogen Generation from Hydrous Hydrazine at Room Temperature. *ACS Appl. Mater. Interfaces* **2015**, *7* (2), 1031–1034.

Appendix Chapter:

MoS_2 Liquid Phase Exfoliation

Acknowledgement:

The work shown in this chapter was done in collaboration with a project that Dr. Vuslat J. Buk was conducting in Tyndall National Institute. Once the MoS_2 was exfoliated it was given to Dr. Vuslat for further study and experimentation.

A.1 Introduction:

The layered material molybdenum (IV) disulphide (MoS_2) is a transition-metal dichalcogenide (TMD) which is similar to the 2D material graphene. It's similarities with graphene mean that this materials layers stack together as a layered crystal.[1] These layered materials can be exfoliated into layers/nanosheets using a range of techniques which include, physical methods of mechanical exfoliation and laser thinning as well as chemical methods of liquid phase exfoliation (LPE)[1] and chemical vapour deposition.[2] However, some of the available methods come with disadvantages which include, inability to scale up, time consuming and sensitivity of the environmental conditions.[3] Finding the right method that is both cost effective and can be scaled up is of great importance for both academic and commercial use.

LPE satisfies the need for a scalable cost-effective method and as a result is the main method used to produce 2D materials in large quantities with a good balance between cost and quantity,[4] as well as having a simple methodology.[5] This mechanism of exfoliation is effective due to the force of the sonication applied and its success lies in using the correct solvent in which to sonicate the TMD. The most common solvent used to separate the MoS_2 into its layers is *N*-methyl-pyrrolidone (NMP)[1–3,6–8] due to its stabilising abilities. However, there are other solvents available that will exfoliate MoS_2 including some of the following, isopropyl alcohol (IPA),[2,7,8] *N*-cyclo-2-pyrrolidone, dimethyl sulfoxide (DMSO), dimethylforamamide (DMF), sodium cholate hydride (SCH)[8] as well as a water and ethanol mixture.[7]

Layered MoS_2 comes in three crystal forms, each with its own suited application. These crystal structures are 1T (D_{3d} group, AA stack), 2H (D_{3H} group, ABAB stack) and 3R (C^5_{3v} group, ABCABC stack) and are applicable in catalysis and 2H-MoS_2 has a bandgap suitable for electronic and optical applications requiring semiconductor characteristics, including gas sensors.[9] Similar to exfoliated graphene, MoS_2 can also be used as additives in lubricants,[10]

phototransistors, memory devices[3] as well as photodiodes[9] and organic photovoltaics.[5] Using the LPE method to exfoliate the MoS2 crystals is very effective as it enables the exfoliated layers to be used across a vast range of applications in different areas.

A.2 Experimental:

The liquid exfoliation methodology of MoS_2 was taken from *Backes et al*.[8] MoS_2 was used in two forms for these experiments. The first was the crystal form of the compound and the second was the powder form of the compound. Both forms required their own solvents for the exfoliation procedure.

A.2.1 MoS_2 Crystal

A piece was of MoS_2 crystal was removed using a pair of tweezers and was placed into a 50 mL sealed Schlenk flask along with 1 mL of the organic solvent, NMP. The Schlenk flask was placed into a beaker of water and sonicated using a bath sonicator for a period of 6-8 hrs. In order to maintain the temperature at ~20-30°C in the sonicator ice was added when required to lower the temperature of the bath. The contents of the flask was monitored throughout the experiment.

A.2.2 MoS_2 Powder

A spatula tip of MoS_2 powder and 1 mL of NMP were placed into the Schlenk flask and sonicated under the same condition as described in section A.2.1. An additional sonication procedure was carried out using the MoS_2 powder, taken from *Backes et al.*[8] In this case an aqueous solvent was used instead of NMP. Sodium cholate hydrate (SCH) was used as the solvent. Into a 50 mL Schlenk flask 0.5 g of SCH was added to 10 mL of deionised water making up the solvent and 0.35 g of MoS_2 powder was added forming a dark navy solution. This solution was sonicated as before for a time of 72 min. The initial 72 mins sonication was considered as a washing step of the MoS_2 powder.

Once completed the solution was removed from the Schlenk flask and centrifuged at 5000 g (6236 rpm) for 25 mins. The supernatant was decanted and replaced with another 0.5 g of SCH in 10 mL of deionised water. This new solution was sonicated as before for 6 hrs while maintaining the temperature of the bath using ice as previously described. It was observed that the solution changed colour throughout the sonication period from dark navy to deep green.

A.2.3 Size Separation of Exfoliated MoS_2

The deep green solution produced from sonication was placed into a centrifuge tube and washed at 4500 rpm for a period of 2 h to separate the larger sheets. This is labelled as Wash 1 in **Table A.1**. The dry tube was weighed before centrifugation and again after once the supernatant was removed and the plug dried. The tube was placed into a drying oven at 60°C until the plug was completely dry before reweighing.

The green supernatant was placed into a second pre-weighed centrifuge tube and centrifuged at 6500 rpm for 2 h to separate the larger sheets. This was labelled as Wash 2 in **Table A.1.**. The supernatant was removed after centrifugation and the plug was placed in a 60°C oven until dry. This tube was then weighed a second time, as described in **Table A.1**.

A.3 Results:

A.3.1 MoS_2 Crystal:

The crystal showed signs of exfoliation after 2.5 hrs of sonication as smaller pieces of the crystal could be seen in the flask. After 6 hrs of sonication the original piece of crystal remained predominantly intact with the exception of a few smaller pieces of the crystal in the NMP solution. Although partial exfoliation of the crystal occurred, powder was deemed the more appropriate option for exfoliation due to its smaller size. In order to better exfoliate the crystal a more powerful sonication such as a probe sonicator would have been more suitable.

A.3.2 MoS_2 Powder:

The solution before sonication occurred was dark navy in colour and after 6 hrs of sonication no change had occurred in relation to the solution colour. This indicated that the MoS_2 powder had not been oxidised. As the powder was smaller in size in relation to the crystal but still not showing signs of exfoliation after a long period of sonication, the exfoliation was carried out using a different solvent other than NMP.

Similar to the powder sonication with NMP, the initial solution colour of the SCH solvent and MoS_2 powder was dark navy. However, 4 hrs into the 6 hrs sonication process the solution began to change colour to eventually becoming dark green. This can be seen in **Figure A.1**. The dark green colour is a poignant indication that the MoS_2 powder had been oxidised and therefore exfoliated into layers as desired. As this combination of MoS_2 powder and aqueous SCH solvent was successful, it was used for all subsequent experiments.

Figure A.1: a) Dark navy MoS_2 solution before sonication, b) Deep green MoS_2 solution after sonication

A.3.3 Size Separation of Exfoliated MoS_2

The results demonstrating the recovery of the MoS_2 from the size separation can be seen in the **Table A.1**. This experiment was carried out using four batches labelled A-D made using SCH as a solvent and MoS_2 powder. The mass of exfoliated product obtained after Wash 1 and Wash 2 procedures are shown. Batch C had low recovery due to an unknown error in the process and as a result was not included in the average concentration or concentration range calculations.

Table A.1: Concentrations and amounts recovered from Batches A-D after size separation

Batch	Product Mass after Wash 1 *4500 rpm, 2 hrs*	Product Mass after Wash 2 *6500 rpm, 2 hrs*	Total Product Retrieved	% Recovery
A	0.315 g/10 mL	0.010 g/10 mL	0.326 g	93.1
B	0.285 g/10 mL	0.183 g/10 mL	0.303 g	86.6
C	0.095 g/10 mL	0.005 g/10 mL	0.100 g	28.6
D	0.304 g/10 mL	0.015 g/10 mL	0.319 g	91.1
Conc. Range	0.285 – 0.315 g/10 mL	0.015 – 0.183 g/10 mL	0.303 – 0.326 g/10 mL	86.6 – 93.1%
Average Conc.	0.232 g/10 mL	0.066 g/10 mL	0.316 g/10 mL	90.3%

From the table it is evident that the separation process recovered up to 93% of the MoS_2 powder initially added at the start of the reaction. This demonstrates that the MoS_2 exfoliated into layers of different sizes as the both the slower speed of 4500 rpm and the faster speed of 6500 rpm both produced product. The majority of exfoliated product 90% is obtained in Wash 1. Although not conducted here, using lower rpm values during centrifuge could further refine the size selective precipitation of exfoliated MoS_2. The exfoliated product was deposited onto a Si wafer and analysed using SEM. The results of which can be seen in **Figure A.2.**

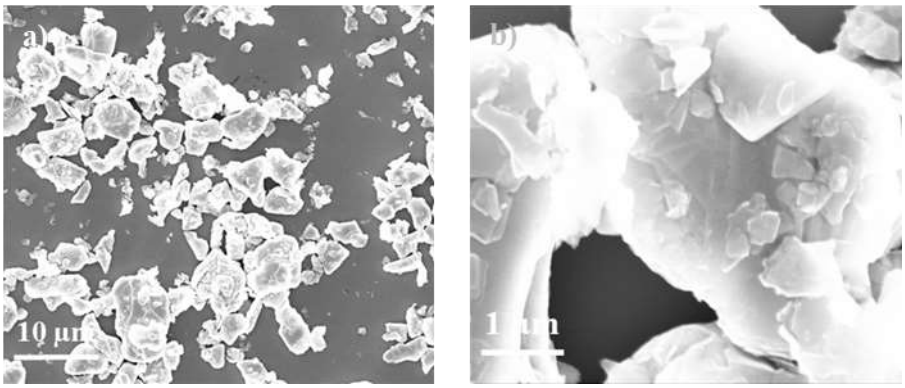

Figure A.2: a) and **b)** SEM images of the exfoliated MoS_2 powder.

It is clear from **Figure A.2** that the vast majority of the MoS_2 powder had been partially exfoliated as there was evidence of layered species on the substrate. However, there was almost no evidence of single exfoliated layers present on the Si substrate under the microscope. **Figure A.2 a)** demonstrates the different size particles that the exfoliation produced while **Figure A.2 b)** highlights the smaller, fragmented layers that are present and more evident on the larger layers that made up the majority of the sample. These images suggest that although exfoliation of MoS_2 took place, a longer sonication time may be needed to produce single layers of the compound or alternatively a stronger exfoliation technique such as probe sonication may be more effective in achieving single layers. Further experimentation would be needed to confirm the best technique for this time of liquid phase exfoliation.

A.4 Conclusion:

LPE was very effective at separating the MoS_2 layers in this experiment, especially in its powdered form. However, even though NMP has been proven to be an effective solvent for this solute with this type of separation, it was not effective here. Its ineffectiveness could be a result of the type of sonication used. Probe sonication may have worked better with both the crystalline MoS_2 as well as the powder MoS_2 due to the higher power obtainable under probe sonication. Longer sonication times beyond 6 h may be required to exfoliate the MoS_2 or the addition of a washing step.

The SCH however, proved to be a superior solvent for the exploitation of MoS_2 and the colour change from dark navy to deep green was a strong indication of this success. Bath sonication seemed to be more suited to this mixture of solvent and solute. The size separation of the exfoliated MoS_2 was also successful as the recovery percentage ranged from 86.6-93.1% However, it is possible that the remainder of the product could be retrieved if the supernatant from the second wash was centrifuged. This method of LPE was successful and this was due in part, to choosing the best pairing of MoS_2 and solvent. However, further improvement in terms of producing individual layers of MoS_2 may be possible using probe sonication.

A.5 References:

(1) O'Neill, A.; Khan, U.; Coleman, J. N. Preparation of High Concentration Dispersions of Exfoliated MoS_2 with Increased Flake Size. *Chem. Mater.* **2012**, *24* (12), 2414–2421.

(2) Backes, C.; Berner, N. C.; Chen, X.; Lafargue, P.; LaPlace, P.; Freeley, M.; Duesberg, G. S.; Coleman, J. N.; McDonald, A. R. Functionalization of Liquid-Exfoliated Two-Dimensional 2H-MoS_2. *Angew. Chem. Int. Ed.* **2015**, *54* (9), 2638–2642.

(3) Zhang, W.; Zhang, P.; Su, Z.; Wei, G. Synthesis and Sensor Applications of MoS_2 -Based Nanocomposites. *Nanoscale* **2015**, *7* (44), 18364–18378.

(4) Li, Z.; Young, R. J.; Backes, C.; Zhao, W.; Zhang, X.; Zhukov, A. A.; Tillotson, E.; Conlan, A. P.; Ding, F.; Haigh, S. J.; Novoselov, K. S.; Coleman, J. N. Mechanisms of Liquid-Phase Exfoliation for the Production of Graphene. *ACS Nano* **2020**, *14* (9), 10976–10985.

(5) Adilbekova, B.; Lin, Y.; Yengel, E.; Faber, H.; Harrison, G.; Firdaus, Y.; El-Labban, A.; Anjum, D. H.; Tung, V.; Anthopoulos, T. D. Liquid Phase Exfoliation of MoS_2 and WS_2 in Aqueous Ammonia and Their Application in Highly Efficient Organic Solar Cells. *J. Mater. Chem. C* **2020**, *8* (15), 5259–5264.

(6) Knirsch, K. C.; Berner, N. C.; Nerl, H. C.; Cucinotta, C. S.; Gholamvand, Z.; McEvoy, N.; Wang, Z.; Abramovic, I.; Vecera, P.; Halik, M.; Sanvito, S.; Duesberg, G. S.; Nicolosi, V.; Hauke, F.; Hirsch, A.; Coleman, J. N.; Backes, C. Basal-Plane Functionalization of Chemically Exfoliated Molybdenum Disulfide by Diazonium Salts. *ACS Nano* **2015**, *9* (6), 6018–6030.

(7) Zhang, X.; Lai, Z.; Tan, C.; Zhang, H. Solution-Processed Two-Dimensional MoS_2 Nanosheets: Preparation, Hybridization, and Applications. *Angew. Chem. Int. Ed.* **2016**, *55* (31), 8816–8838.

(8) Backes, C.; Higgins, T. M.; Kelly, A.; Boland, C.; Harvey, A.; Hanlon, D.; Coleman, J. N. Guidelines for Exfoliation, Characterization and Processing of Layered Materials Produced by Liquid Exfoliation. *Chem. Mater.* **2017**, *29* (1), 243–255.

(9) Kim, S.; Park, W.; Kim, D.; Kang, J.; Lee, J.; Jang, H. Y.; Song, S. H.; Cho, B.; Lee, D. Novel Exfoliation of High-Quality 2H-MoS2 Nanoflakes for Solution-Processed Photodetector. *Nanomaterials* **2020**, *10* (6), 1045.

(10) Singh, K. K.; Prabhu B, R.; Choudhary, S.; Pramanik, C.; John, N. S. Effect of Graphene and MoS_2 Flakes in Industrial Oils to Enhance Lubrication. *ACS Omega* **2019**, *4* (11), 14569–14578.